REALIZATION OF DETECTOR BASED SPECTRAL RESPONSIVITY SCALE FROM ULTRAVIOLET TO NEAR INFRARED REGIONS OF ELECTROMAGNETIC SPECTRUM

A THESIS SUBMITTED TO
THE GRADUATE SCHOOL OF NATURAL AND APPLIED SCIENCES
OF
MIDDLE EAST TECHNICAL UNIVERSITY

BY

ÖZCAN BAZKIR

IN PARTIAL FULFILLMENT OF THE REQUIREMENTS FOR THE DEGREE
OF

DOCTOR OF PHILOSOPHY

IN

PHYSICS

JUNE 2004

Approval of the Graduate School of Natural and Applied Sciences

_____
Prof. Dr. Canan Özgen
Director

I certify that this thesis satisfies all the requirements as a thesis for the degree of Doctor of Philosophy.

_____
Prof. Dr. Sinan Bilikmen
Head of Department

This is to certify that we have read this thesis and that in our opinion it is fully adequate, in scope and quality, as a thesis for the degree of Doctor of Philosophy.

_____
Assoc. Prof. Dr. Sevilay Uğur
Co-Supervisor

_____
Assoc. Prof. Dr. Akif Esendemir
Supervisor

Examining Committee Members

Prof. Dr. Ali Gökmen	(METU, CHEM)	_____
Assoc. Prof. Dr. Akif Esendemir	(METU, PHYS)	_____
Assoc. Prof. Dr. Sevilay Uğur	(TÜBİTAK, UME)	_____
Prof. Dr. Bülent Akınoğlu	(METU, PHYS)	_____
Prof. Dr. İbrahim Günal	(METU, PHYS)	_____

I hereby declare that all information in this document has been obtained and presented in accordance with academic rules and ethical conduct. I also declare that, as required by these rules and conduct, I have fully cited and referenced all material and results that are not original to this work.

Name, Last Name : Özcan, Bazkır

Signature :

ABSTRACT

REALIZATION OF DETECTOR BASED SPECTRAL RESPONSIVITY SCALE FROM ULTRAVIOLET TO NEAR INFRARED REGIONS OF ELECTROMAGNETIC SPECTRUM

Bazkır, Özcan

Ph.D., Department of Physics

Supervisor: Assoc. Prof. Dr. Akif Esendemir

Co-Supervisor: Assoc. Prof. Dr. Sevilay Uğur

June 2004, 114 pages.

Realization of spectral responsivity scale was studied in three stages. Firstly, absolute optical power measurements using Electrical Substitution Cryogenic Radiometer (ESCR) was studied. The absolute measurements were done at discrete laser wavelengths of tunable Ar+ (488 nm and 514.5 nm), Nd:YAG (532 nm) and fixed He-Ne (632.8 nm) laser sources. To increase measurement accuracy the method used for the stabilization of laser beams, transmittance measurements of optical windows, and minimization of scattered beams were discussed.

Secondly, realization of absolute responsivity scale between 350- 850 nm ranges was studied. The scale based on reflection type trap detectors consisting of three silicon photodiodes. Various measurement systems were established in order to make optical characterization of trap detectors like non-linearity, surface non-homogeneity, polarization dependency, reflectance, and internal quantum efficiency. The absolute responsivity was linked to the absolute optical power by measuring the current response of trap detectors to the absolute power measured by ESCR system at laser wavelengths. Using models for the trap detector's, reflectance and internal quantum efficiency the scale between 350- 850 nm ranges was realized with an uncertainty of 0.05 %.

Finally, the spectral responsivity scale in ultraviolet (UV) and near-infrared (NIR) regions was realized using Electrically Calibrated Pyroelectric Radiometer (ECPR). Optically characterizing the spatial non-uniformity of pyroelectric detector and its surface reflectance, the spectral responsivity scale was established with uncertainties ±0.5-1.0 % between 250 nm and 350 nm and ±0.5-1.5 % between 850 and 2500 nm.

Key Words: Cryogenic radiometer, laser stabilizer, optical power, photodiode, trap detector, responsivity, pyroelectric radiometer.

ÖZ

DEDEKTÖR TABANLI TAYFSAL DUYARLILIK ÖLÇEĞİNİN ELEKTROMANYETİK TAYFININ MORÖTESİ İLE YAKIN KIZILÖTESİ BÖLGELERİ ARASINDA OLUŞTURULMASI

Bazkır, Özcan
Doktora, Fizik Bölümü
Tez Yöneticisi: Doç. Dr. Akif Esendemir
Ortak Tez Yöneticisi: Doç. Dr. Sevilay Uğur

Haziran 2004, 114 sayfa.

Tayfsal duyarlılık ölçeğinin oluşturulması üç aşamada gerçekleştirilmiştir. Birinci aşamada, mutlak optik güç ölçümlerinin elektriksel yerine koyma prensibi ile çalışan düşük sıcaklık radyometresi (ESCR) ile gerçekleştirilmesi anlatılmıştır. Mutlak güç ölçümleri dalga boyu ayarlanabilen Ar+ (488 nm ve 514.5 nm), Nd:YAG (532 nm) ve sabit He-Ne (632.8 nm) lazer dalga boylarında gerçekleştirilmiştir. Ölçümleri yüksek hassasiyetle gerçekleştirmek için lazer çıkış gücü kararlaştırma metodu, optik camlarının geçirgenliği ve saçılan ışınların minimizasyonu gibi çalışmalar yapılmıştır.

İkinci aşamada 350-850 nm dalga boyu aralığında tayfsal duyarlılık ölçeğinin mutlak olarak oluşturma çalışılması yapılmıştır. Ölçek üç adet silikon fotodiyottan yapılmış yansıma tipi tuzak dedektörler üzerine kurulmuştur. Çeşitli ölçüm düzenekleri kurularak tuzak dedektörlerin doğrusallıktan sapma, yüzey duyarlılık değişimi, polarizasyon bağımlılığı, yansıma ve iç kuantum verimi gibi optik karakterizasyon ölçümleri yapılmıştır. Mutlak duyarlılık ölçümleri tuzak dedektörlerin ESCR sistemi ile ölçülen mutlak güç ölçümlerine karşı tepkileri akım cinsinden lazer dalga boylarında ölçülerek elde edilmiştir. Tuzak dedektörlerin iç

kuantum verimi ve yansımaları için geliştirilen modeller kullanarak duyarlılık ölçeği 350- 850 nm dalga boyu aralığında % 0.05 belirsizlikle gerçekleştirilmiştir.

Son olarak elektriksel kalibreli pyroelektrik radyometre ile duyarlılık ölçeğinin morötesinden yakın kızılötesi bölgesine kadar oluşturulması çalışılmıştır. Pyroelektrik dedektörün doğrusallıktan sapması ve yüzey yansıması optiksel olarak karakterize edilmesi ile tayfsal duyarlılık ölçeği 250 nm ile 350 nm arasında % ±0.5-1.0, 850 ile 2500 nm arasında % ±0.5-1.5 belirsizlikle gerçekleştirilmiştir.

Anahtar Kelimeler: Düşük sıcaklık radyometresi, lazer kararlaştırma sistemi, optik güç, fotodiyot, tuzak dedektör, duyarlılık, pyroelektrik radyometre.

ACKNOWLEDGMENTS

I express sincere appreciation to my supervisors Assoc. Prof. Dr. Akif Esendemir and Assoc. Prof. Dr Sevilay Uğur for their guidance and insight throughout the research.

I would like to express my deepest gratitude to Dr Farhad Samedov for having provided me excellent working conditions, encouragement and guidance throughout this study.

I would like to thank Oğuz Çelikel for his valuable comments and discussions during this work.

I would like to thank my PhD committee members Prof. Dr. Bülent Akınoğlu, Prof. Dr. Ali Gökmen and Prof. Dr İbrahim Günal for their time and helpful comments.

I would also like to thank Assoc. Prof. Dr. Hüseyin Uğur for providing me a chance to work on this subject.

All the work presented in this thesis was supported and conducted at TÜBİTAK (Scientific and Technical Research Council of Turkey) - UME (National Metrology Institute of Turkey) and METU Physics Department. I thank TÜBİTAK-UME and METU Physics Department.

TABLE OF CONTENTS

PLAGIARISM……..…… iii
ABSTRACT..……..... iv
ÖZ……. vi
ACKNOWLEDGMENTS…..……..... viii
TABLE OF CONTENTS……. ix
LIST OF TABLES…… xii
LIST OF FIGURES…….. xiii
LIST OF SYMBOLS and ABBREVIATIONS…… xvii
CHAPTERS

1 INTRODUCTION…….. 1

2 PRIMARY STANDARDS AND REALIZATION OF ABSOLUTE POWER SCALE……. 7
2.1 Source for Absolute Detectors…….. 8
2.2 Electrical Substitution Cryogenic Radiometer……. 8
2.2.1 Principle of Electrical Substitution Radiometers. 8
2.2.2 Description of ESCR System……... 10
2.2.2.1 The Absorptivity of the Cavity…..… 13
2.2.2.2 The Electrical Heaters…….…….. 14
2.2.2.3 The Heat Flow Path…….……. 18
2.2.2.4 The Temperature Sensors……. 18
2.2.2.5 Temperature of Reference Block..… 20
2.2.2.6 Radiometer Sensitivity…….. 20
2.2.2.7 Temperature Ranges of Cryogenic Radiometer…….……... 21
2.2.2.8 Power Ranges of Cryogenic Radiometer…… 21

2.2.3 Measurement Preparations …….. 22
2.2.3.1 Power Stabilization of Laser Beam.. 22
2.2.3.2 Transmittance Measurements of Radiometer Entrance Window.....… 30
2.2.3.3 Minimization of Scattered Light….. 33
2.2.4 Measurement and Calculation of Laser Power… 35

3 TRANSFER STANDARDS AND REALIZATION OF ABSOLUTE SPECTRAL RESPONSIVITY SCALE…… 42
3.1 Trap Detectors…….. 42
3.2 Optical Characterizations of Trap Detectors…… 44
3.2.1 Noise equivalent power (NEP)…….…… 44
3.2.2 Polarization Dependency…….. 45
3.2.3 Non-Linearity……... 46
3.2.4 Spatial Non-uniformity…… 48
3.2.5 Temporal Stability…….…….... 50
3.2.6 Reflectance Losses……... 51
3.2.7 Quantum efficiency…….. 54
3.2.8 Responsitivity…….. 56
3.3 Interpolation and Extrapolation of Responsivity…….……. 57
3.3.1 Calculation of the Reflectance of Silicon Photodiode…….. 58
3.3.2 Calculation of the Quantum Efficiency of Silicon Photodiode……... 67
3.3.3 Models Used for the IQE Calculations of Silicon Photodiodes……. 67
3.3.4 Realization of responsivity scale from 350 nm to 850 nm……. 72
3.3.5 Extension of Responsivity Scale to UV (250 nm) and NIR (2500 nm)…… 73

4 REALIZATION OF RELATIVE SPECTRAL RESPONSIVITY SCALE…… 75
4.1 Electrically Calibrated Pyroelectric Radiometer (ECPR)…….……. 75
4.1.1 Readout…….…… 75
4.1.2 Pyroelectric Probe…….……... 76
4.1.3 Chopper…… 77
4.2 Operation of ECPR…….…….……. 77
4.3 Optical Characterizations of ECPR…….……. 80
4.3.1 Response Non uniformity……. 80
4.3.2 Reflectance Measurements……... 81
4.3.3 Response Non-linearity…..……... 83
4.3.4 Responsivity Measurements…….…… 84
4.3.5 Calibration of ECPR against ESCR……. 85
4.4 Relative Spectral Responsivity Measurements of Working Standards Using Spectrometer…….. 87
4.5 Responsivity measurements of Silicon (Si), Silicon Based Trap detector (TD), Germanium (Ge) and Indium Galium Arsenide (InGaAs) in UV and NIR Regions.....……. 93

5 CONCLUSION.....…… 103
REFERENCES..... 105
VITA..... 114

LIST OF TABLES

TABLES

2.1	Source and detector based primary standards……..	7
2.2	Transmittance measurements of window at Brewster angle……...	32
2.3	Optical power measurements at various laser wavelengths and corresponding uncertainties…….	40
2.4	Uncertainty budget for optical power measurement at 632.8 nm wavelength……...	41
3.1	Uncertainty budget for responsivity measurements of trap detectors.....	73
4.1	Uncertainty budget for responsivity measurements of ECPR…….	87
4.2	Monochromator parameters…….	88
4.3	Spectrometer parameters; filters and gratings…….	89

LIST OF FIGURES

FIGURES

2.1	Schematic illustration of ESR and it's principal of operation…….	9
2.2	High accuracy cryogenic radiometer system……...	11
2.3	Cryogenic Radiometer Wiring and Electronic Scheme……...	12
2.4	Cryogenic radiometers electrical heater system……...	15
2.5	Temperature response of cavity to the heater A……..	16
2.6	Temperature response of cavity to the heater B……...	17
2.7	Non-equivalence correction factor versus power…….……	17
2.8	Laser Power Stabilizer System, A1, A2 and A3 are apertures.……	23
2.9	a: Calcite crystal, b: polarizer made from calcite…….……	24
2.10	Neutral density filters and their effect on the photographs..…..……...	24
2.11	Wedged beam splitter……..	25
2.12	Variation of stabilized Ar^+ (488.1 nm) laser beam in time……..	26
2.13	Variation of stabilized Ar^+ (514.5 nm) laser beam in time……..	27
2.14	Variation of stabilized Nd:YAG (532 nm) laser beams in time……..	27
2.15	Variation of stabilized He-Ne (632.8 nm) laser beam in time…….	28
2.16	Gaussian beam and diffraction pattern…….……	29
2.17	Beam shape of lasers used in the measurements.a) Ar^+at 488 nm, b) Ar^+ at 514.5 nn, c) Nd:YAG at 532 nm and d) He-Ne at 632.8 nm…….	29
2.18	a- Gimbal holder, b-birefringence effect of liquid crystal…….…..	30
2.19	Transmittance measurement set up for the window…….……	31
2.20	Glan Laser polarizer…….…….…….……..	32
2.21	Quadrant photodiode ……..……	33
2.22	Set up for the minimization of scattered and adjustment of light into the cavity……...	34

2.23	Quadrant Diode Wiring Rotue in Cryogenic Radiometer……	35
2.24	Thermal calibration of absorbing cavity……..	37
2.25	Static substitution method for the optical power measurements. OPTdesignate optical temperature, ETH and ETL electrical high and low temperatures EPH and EPL electrical power high and low respectively…….……..……..	37
2.26	Illustration of optical power measurements of Ar^+ (488.1 nm) laser...	38
2.27	Illustration of optical power measurements of Ar^+ (514.5 nm) laser...	38
2.28	Illustration of optical power measurements of Nd:YAG (532 nm) laser….	39
2.29	Illustration of optical power measurements of He-Ne (632.8 nm) laser…..……	39
3.1	Internal structure of trap detector and silicon photodiode…..……..	43
3.2	Illustration of single photodiode and its internal structure……...	43
3.3	Relative change in responsitivity of trap detectors as a function of the rotation angle about beam axis…….……..	46
3.4	Non-linearity measurement set up. A1, A2, A3, A4 and A5 are apertures; S1 and S2 are shutters……...…….	47
3.5	Non-linearity measurement of silicon based trap detectors TD-1, TD-2, TD-3 and TD-4……..	48
3.6	Spatial uniformity measurement set up……	49
3.7	Relative spectral responsitivity maps of trap detector and silicon photodiode in two-dimensional view……..…….……...	49
3.8	Relative spectral responsivity maps of silicon photodiode and trap detector in one-dimensional view……..…….	50
3.9	Response stability of trap detectors at 632.8 nm He-Ne laser wavelength……...	51
3.10	Set up for the absolute reflectance measurements of trap detectors..…….	52
3.11	Set up for the relative reflectance measurements of trap detectors…..	53
3.12	Illustration of reflectance of trap detectors. ……	53
3.13	Internal quantum efficiency of trap detector……...…….	54
3.14	Diagrammatic representation of interaction of light with silicon photodiode as a function of wavelength.…….…….	55

3.15	Absolute responsivity measurements at 488.1 nm, 514.55 nm, 532.1 nm and 632.8 nm wavelengths using ESCR……	57
3.16	Photodiode structure with behaviour of fields at the interface between silicon and silicon dioxide…….	59
3.17	Reflection and refraction with the polarization, a) perpendicular to the plane of incidence, b) parallel to the plane of incidence……	61
3.18	Illustration of multiple reflections between two interfaces……..	63
3.19	Calculation of reflectance of p polarized light at 45^0……...	65
3.20	Calculation of reflectance of s polarized light at 45^0……...	66
3.21	Calculation of reflectance of s polarized light at 0^0…….	66
3.22	Calculation of reflectance of trap detector……...	67
3.23	Measured and modelled (first model) IQE of trap detector…….	68
3.24	Absorption coefficient of silicon photodiode……...	69
3.25	Measured and modelled (second model) IQE of trap detector…….	70
3.26	Modelling of EQE of trap detector……...	72
3.27	Responsivity of trap detectors obtained from combination of measured and modeled values……..……..…..…….……	74
4.1	Electrically Calibrated Pyroelectric Radiometer System…….	76
4.2	Schematic diagram of electrically calibrated pyroelectric radiometer.	78
4.3	Chopper arrangement of ECPR……	79
4.4	Spatial response variation of the pyroelectric detector……	81
4.5	Reflectance measurement set up for pyroelectric detector……...	82
4.6	Spectral reflectance of gold-black coated pyroelectric detector versus wavelength……	83
4.7	Responsivity measurement of ECPR system against ESCR……...	85
4.8	Spectral reflectance measurement results of pyroelectric detector…..	86
4.9	Schematic representation of the spectrometer configuration used in spectral responsivity measurements. OSF, order-sorting filter; CSM1, CSM2, CSM3, CSM4 collimating spherical mirrors; M1, M2, M3, M4 flat mirrors,LA, limiting aperture; OPM, off-axis parabolic mirror; SHU, detector holder unit; RD and TD, reference and test detectors; DMM, digital multimeters…….……..	91

4.10 Spectral irradiance from a quartz halogen lamp 50 cm from the filament……. 92

4.11 Spectral irradiance of a deuterium lamp 50 cm from the filament……. 92

4.12 Spectral responsivity of silicon photodiode detector……... 96

4.13 Spectral responsivity of trap detector (TD-1)…….. 96

4.14 Spectral responsivity of trap detector (TD-2)…….. 97

4.15 Spectral responsivity of trap detector (TD-3)…….. 97

4.16 Spectral responsivity of trap detector (TD-4)…….. 98

4.17 Spectral responsivity of trap detector (25.4)..…….. 98

4.18 Spectral responsivity of trap detector (25.4-1)…… 99

4.19 Spectral responsivity of InGaAs photodiode detector…….. 99

4.20 Spectral responsivity of Ge photodiode detector……. 100

4.21 Spectral responsivity of photometer head (9411114)…….. 100

4.22 Spectral responsivity of photometer head ……... 101

4.23 Spectral responsivity of filter radiometer (25.4)…….. 101

4.24 Spectral responsivity of filter radiometer (25.4-1)……... 102

LIST OF SYMBOLS and ABBREVIATIONS

ESR	Electrical Substitution Radiometer
ESCR	Electrical Substitution Cryogenic Radiometer
ECPR	Electrically Calibrated Pyroelectric Radiometer
LPS	Laser Power Stabilizer
EOM	Electro-Optic Modulator
ND	Neutral Density
He	Helium
N_2	Nitrogen
Ge	Germanium
GRT	Germanium Resistance Thermometer
RhFe	Rhodium Iron
Pt	Platinum
NiP	Nickel Phosphor
$LiTaO_3$	Lithium Tantalite
$BaSO_4$	Barium Sulphate
P_{el}	Electrical power
P_{opt}	Optical Power
T_C	Cavity temperature
T_S	Heat sink at temperature
Nd:YAG	Neuodium Yag
He-Ne	Helium Neon
Ar^+	Argon Ion
S	Scattering
τ	Transmittance
α	Absorbance
ρ	Reflectance
θ	Theta
Ω	Ohm

μ	Micron
K	Kelvin
Pa	Pascal
n	Refractive Index
NEP	Noise Equivalent Power
TD	Trap Detector
R	Responsivity
IQE	Internal Quantum Efficiency
EQE	External Quantum Efficiency
δ	Internal Quantum Deficiency
Si	Silicon
SiO_2	Silicon dioxide
UV	Ultraviolet
VIS	Visible
NIR	Near Infrared
OSF	Order-Sorting Filter
CSM	Collimating Spherical Mirror
M	Flat Mirror
LA	Limiting Aperture
OPM	Off-Axis Parabolic Mirror
SHU	Spectral Detector Holder Unit
RD	Reference Detector
Td	Test Detector
DVM	Digital Voltmeter

CHAPTER 1

INTRODUCTION

Radiometry is the science of the measurement of electromagnetic radiant energy. The origin of radiometry goes back to the late nineteenth century when the first absolute radiometers (the instruments used for making the measurements) were independently developed by Angstrom and Kulbraum [l, 2]. Angstrom particularly used his radiometer in the field of metrology to measure the solar irradiance at the Earth's surface, whereas the Kurlbaum radiometer was used to establish a radiometric-based standard for the unit of luminous intensity. Although the objectives of the experiments were different, both the radiometers were thermal detectors of radiation based upon the principle of electrical substitution. That is, the radiant power is measured by substituting the equivalent amount of electrical power (which can be accurately determined) so that the thermal conditions within the radiometer are identical for the two different modes of heating.

Throughout the twentieth century electrical substitution radiometers (ESRs) have been further developed, becoming the most frequently used instruments for establishing detector based radiometric scales. However, their performance is limited by the thermal properties of materials at 293 K resulting in the complicated corrections that have to be applied: for example, for the incomplete absorption of the incident radiation and for the non-equivalence of the substituted electrical power to the absorbed radiant power [3]. Hence, even with the most innovative design including computer-controlled correction packages the accuracy of modern ambient temperature ESRs still remains in the range 0.1% to 0.3% [4- 6].

To satisfy the increasing demand for more accurate ESRs from users not just in the fields of metrology, basic physics and photometry as in the past, but also in the new and expanding fields of optical fibers, laser technology, synchrotron radiation,

radiometric standards, defense technology and space science, two new approaches have been made to improve the accuracy with which radiant power can be measured.

The first approach has been developed by Geist and Zalewski at the National Institute of Standards and Technology, USA (NIST), using silicon photodiodes [7-9]. They discovered that certain diodes could be manufactured with such high quality that their quantum efficiency approximated to unity over a large region of the visible spectrum. This technique is based on decreasing the fraction of photo generated charge carriers lost by recombination effects within the photodiode. In a photodiode the major loss parameters are recombination around depletion region and positive trap charges at the Si/SiO_2 interface. These trap charges attracts electrons and lengthens the time, compared to carrier lifetime, taken to reach the depletion region and this increases the probability of recombination. The fist effect can be evaluated by applying a reverse bias to the photodiode, which extends the depth of the depletion region such that the collection efficiency in the rear of photodiode can brought to unity. The effects of trap charges at the Si/SiO_2 interface can be removed by storing large negative charges on the SiO_2 surface using a drop of water, dilute boric acid solution or discharging electrons. Removing internal losses the responsivity of photodiodes can be obtained from front surface reflection losses and theoretical value in the visible region. As a result they were able to develop "a self-calibration" technique by which the absolute spectral response of the diodes could be measured with an uncertainty of better than 0.1%.

The second approach has been cryogenic radiometry. Ginnings and Reilly at NIST construct an apparatus to measure the radiant flux from a black-body using a low-temperature heat flow calorimeter. Blackbody radiation, for decades have been used as the primary source based standard. The history of these traditional standards maybe tracked to as far as the 1860's, when German physicist Gustav Robert Kirchhoff first published a paper describing blackbody radiation [10]. The first physical realization of proper blackbody radiator was done by Wien and Lummer in 1895 [11]. The output spectrum of a blackbody radiator may be derived from the temperature of it's cavity by Planck's radiation low. Therefore, a scale (unit) for spectral irradiance or spectral radiance may be derived from a temperature scale, e.g. the international temperature scale [12] ITS-90. The highest uncertainty in this kind

of realization arises from the temperature measurements. For example, in the ultraviolet (UV) region, they limit the uncertainty of the spectral irradiance measurements to a level of approximately 1% to 2 % [13]. The aim of Ginnings and Reilly's experiment was to realize the thermodynamic temperature of the boiling point of water [14]. Although they did not succeed in their aim, largely for reasons related to diffraction and scattering, they did demonstrate the potential of such an apparatus. Also, at about this time, Blevin and Brown at the National Measurement Laboratory, Australia (NML), using an ambient temperature ESR and a black-body radiator at the temperature of the freezing point of gold determined the Stefan-Boltzmann constant, σ with an uncertainty of 0.1% [15]. They also showed how diffraction can lead to errors of the order 1%, and how, in principle, such errors could be avoided [16].

Greatly influenced by these two experiments at NIST and NML, Quinn and Martin at the National Physical Laboratory, UK (NPL), constructed the first successful total-radiation thermometer [17,18]. They were able to realize thermodynamic temperature with an uncertainty of a few mK over the range -130 to 100 °C, but more relevant to the field of radiometry they also determined a value for σ. Their value had an uncertainty of 0.017% and differed from the calculated value by only 13 parts in 10^5. The detector part of the apparatus, consisting of an absorbing heat flow calorimeter, could also be considered quite simply as an ESR cooled to liquid-helium temperatures, and hence became known as a cryogenic radiometer. The measurement of σ clearly demonstrated that by using a cryogenic radiometer the accuracy of the measurement of radiant flux could be improved by at least an order of magnitude than had been achieved.

Geist and Zalewski, who were working on their self-calibration technique for photodiodes but had no way of experimentally checking the validity of their results, suggested an intercomparison with the cryogenic radiometer. By modifying the total-radiation thermometer, in particular, removing the radiating black-body and inserting an optical window in the outer vacuum chamber, a laser beam could be directed into the cryogenic radiometer. The laser power could then be measured using the radiometer and compared to the measurement using a photodiode. Although the uncertainty of the intercomparison was slightly higher than had been planned, due to

the problems associated with the window transmittance, the method did show promise for the future. Hence, a second cryogenic radiometer was constructed at NPL dedicated to the measurement of optical radiation with a calculated uncertainty of 0,005% [19], and this is probably the most accurate radiometer available today.
The development of cryogenic absolute radiometer [20-24] in the 80's has started a tremendous change in radiometry and photometry. Due to the low uncertainty significant effort has been devoted recently to developing new realizations for photometric and radiometric units that are traceable to cryogenic absolute radiometers.

Another important subject, almost as important as the development of the cryogenic radiometer, has been development of tarp detectors [25-27]. The cryogenic absolute detectors are voluminous and rather difficult and expensive to operate. Also, the measurements are usually limited to using laser light sources. Trap detectors have proven to be an excellent choice for a transfer standard detector. They may be used e.g. in international comparisons of radiant power scales [28-32] or to form a spectral responsivity scale to interpolate radiant power calibrations between the laser wavelengths used in the calibrations with cryogenic radiometers [33,34]. Since the absolute optical power scale can be obtained at laser wavelengths then the high accuracy responsivity scales also can only be realized at discrete laser wavelengths. At other wavelengths in the visible region, the responsivity values can be determined by interpolating and extrapolating the Internal Quantum Efficiency (IQE) of trap detectors [35-41].

This work is the realization of detector based responsivity scale project developed in UME Optics Laboratory. The high accuracy measurement facilities are performed using an electrical-substitution cryogenic radiometer (ESCR) working at liquid helium temperature (4.2 K) as a primary standard. The basic elements of the ESCR are absorbing cavity, radiometer entrance window, quadrant photodiodes, heaters, reference block, dummy cavity and Germanium (Ge) and Rhodium Iron (RhFe) heat sensors. Each component was characterized carefully to get accurate measurement results. Operating radiometer at liquid helium temperature lead us to measure optical powers with an uncertainty in the order of 1.2×10^{-4}. This high

accuracy is due to the advantages of operating radiometer at low temperatures. The advantages are as follows [42]:

i. the heat capacity of the absorbing material is drastically reduced at low temperatures, which in turn, reduces the time constant and measurement time accordingly;
ii. heat loss is reduced at low temperatures because of the radiant energy is proportional to T^4;
iii. heat contributions from the resistor leads is eliminated by using superconductive wires;
iv. operating the detector in vacuum eliminates convection losses.

Although, the ESCR has these advantages, the uncertainty in optical power strongly depends on preparation; namely quality of stabilization of optical beam, cleanness of Gaussian laser beam, quality of cleaning and transmittance of window, deviations from the Brewster angle and minimization of scattered light. Therefore, all these conditions were checked and measured carefully in order to realize the UME optical power scale and more importantly to evaluate the uncertainty of the scale.

To link the high accuracy measurements obtained from the ESCR to the other optical power measurements silicon based (Hamamatsu S1337-11 windowless photodiodes) reflection type trap detectors were constructed in UME, have been used as transfer standards. The reasons for using trap detectors as transfer standards are that they have following properties [26]:

i- Low noise equivalent power
ii- Polarization independency
iii- Low non linearity
iv- Good spatial uniformity
v- Good temporal stability
vi- Low reflectance looses
vii- High quantum efficiency
viii- Predicted spectral responsivity in the visible region

Various measurements systems were established so as to study the characteristics and influence parameters of trap detectors, having in view their use as transfer standards. The absolute responsivity linked to the absolute optical power was

obtained using laser power stabilization optics and electrical substitution cryogenic radiometer system at discrete laser wavelengths. Using physical models for the trap detectors reflectance and internal quantum efficiency the scale was realized with an expanded uncertainty of 0.05 % from 350 nm to 850 nm.

The spectral responsivity scale from ultraviolet (UV) to near-infrared (NIR) regions was realized using electrically calibrated pyroelectric radiometer (ECPR). Its spectral responsivity was linked to the ESCR facility at discrete laser wavelengths. The active element of ECPR is pyroelectric detector, which is gold-black coated lithium tantalite crystal ($LiTaO_3$). Optically characterizing the spatial non-uniformity in pyroelectric detector responsivity and its surface reflectance, the spectral responsivity scale was established from 250 nm to 2500 nm.

The subject area of this thesis includes three chapters. In the chapter 2 ESCR system, measurement preparations (stabilization of the laser beam, cleaning and the transmittance measurements of window at the Brewster angle and minimization of scattered light) and measurement techniques, calculation of optical power and uncertainties are described. In chapter 3 reflection type trap detectors, their optical characterizations (polarization independency, non linearity, spatial uniformity, temporal stability, quantum efficiency and reflectance looses) are described. Moreover, the models for interpolations and extrapolations of reflectance and quantum efficiency needed for the interpolation and extrapolation of responsivity values of trap detectors in the 350-850 nm regions are described. In the chapter 4, ECPR system, its working principles, optical characterizations (linearity, spatial non uniformity and reflectance) and realization of responsivity scale from 250 nm to 2500 nm are studied. In addition spectral responsivity measurements of working standards (Si, Si based trap detectors, Filter Radiometers, Photometer Heads, Ge, InGaAs) using ECPR and double monochromator system are also described.

CHAPTER 2

PRIMARY STANDARDS AND REALIZATION OF ABSOLUTE OPTICAL POWER SCALE

Spectral responsivity scales are usually maintained on transfer standard detectors. These detectors can then be used to calibrate the spectral responsivity of another detector by comparison. To do this a source is used as a transfer medium. Since the scale must have spectral information, either detector or the source must be spectrally selective. This can be achieved by the use of a monochromator or laser for the light source.

The realization of the spectral responsivity scale can be carried out using an absolute source (known spectral radiance) or an absolute detector (independently known spectral responsivity). There are different options within each generic area and these are summarized in table 2.1 [43]. In general, the absolute detector is most commonly used method for the visible and near infrared region of the spectrum, and so this technique will be discussed in more detail.

Table 2.1: Source and detector based primary standards

Source Based Standards	**Detector Based Standards**
Black Body Radiation	Electrical Substitution Radiometer (ESR)
Synchrotron Radiation	Self Calibrated Photodiodes
Calibrated Lamps	Electrical Substitution Cryogenic Radiometer (ESCR)

2.1 Source for Absolute Detectors

To realize a spectral responsivity scale using an absolute detector requires a source of monochromatic radiation. This source can be calibrated to act as a temporary transfer medium to calibrate other detectors. Monochromators and lasers are the most commonly used sources but filtered lamps or blackbodies could be used.

Lasers provide the most accurate and convenient source. The laser is a source of a high spectral radiance. It is usually collimated, providing very convenient, geometrically well-defined, beam of radiation. However, the radiance of lasers is not usually very stable. The stability can be improved by using an external stabilizing technique and instruments. Such a system can provide a beam of monochromatic radiation that has a radiant power stable to 0.001% over several hours.

2.2 Electrical Substitution Cryogenic Radiometer

Electrical Substitution Cryogenic Radiometer (ESCR) is a device that measures optical radiation by comparison to an equivalent amount of electrical power at low temperatures. In order to understand ESCR and see the effects of operating radiometer at low temperatures, working principle of Electrical Substitution Radiometer (ESR) should be considered first.

2.2.1 Principle of Electrical Substitution Radiometers

The principle of operation of an ESR is that a thermometer is used to measure the temperature rise of the detector, relative to a constant temperature of reference block, during alternate radiant and electrical heating cycles. By adjusting the electrical power so that the detector temperature rise is the same for both types of heating, the radiant power can be equated to the measured quantity of electrical power. Referring to figure 2.1, the electrical power is equal to the radiant power when radiant temperature equal to electrical temperature.

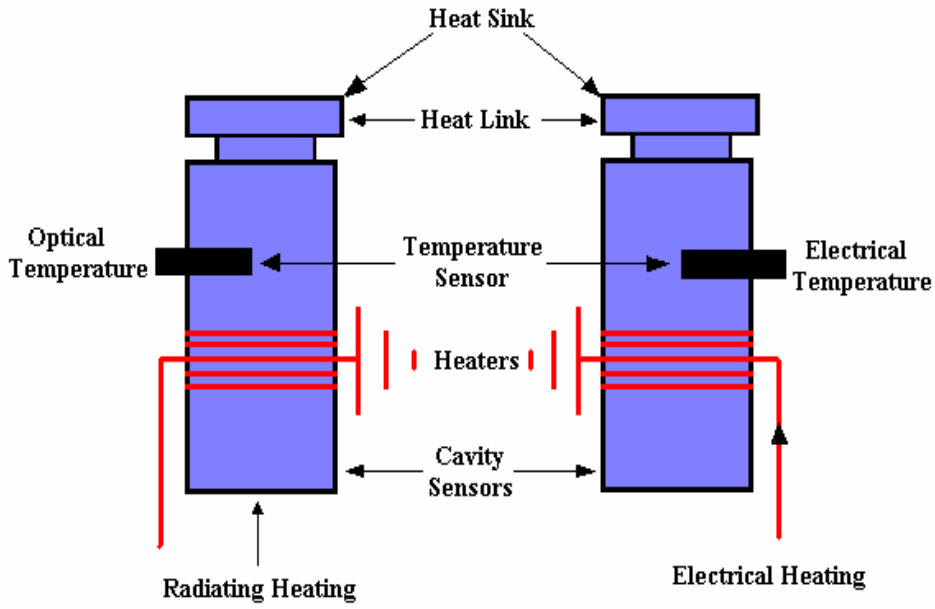

Figure 2.1: Schematic illustration of ESR and it's principal of operation.

In order that the thermometer responds equally to equivalent radiant and electrical power, the following conditions must be satisfied [21]:

a) Cavity should have a high absorbance to ensure that all the incident radiant flux is absorbed and contributes to the rise in the detector temperature,

b) All the electrical power supplied should be dissipated as heat in the detector, and negligible power should be dissipated in, or conducted down, the connecting leads,

c) The heat flow path from the detector to the reference block should be identical for electrical and radiant heating, and should not be influenced by any difference in temperature gradients in the detector created by the two separate heating modes,

d) The thermometer that monitors the temperature rise of the detector should have a small thermal capacity and be in thermal equilibrium with the detector; it should also have appropriate resolution and sensitivity,

e) The temperature of the reference block should remain constant during the period of measurement,

f) The detector should be shielded from other sources of thermal radiation, and its field of view restricted to reduce any scattered radiation falling on the detector surface.

Each of the above conditions will be considered in depth, including an explanation as to why they can be satisfied more easily by ESCR.

2.2.2 Description of ESCR System

ESCR system shown in figure 2.2 constitutes cavity, cryostat, reference block, thermal links, quadrant photodiodes and radiometer entrance window. The internal structure of cryogenic radiometer, it's wiring and electronic scheme is shown in figure 2.3.

The central element of the ESCR as shown in figure 2.3 is the cavity that is designed for the complete absorption of optical radiation. The absorbing cavity thermally connected to the reference block by a stainless steel tube. The reference block is in turn connected to liquid helium reservoir and its temperature is kept constant by a temperature controller. There are two heater resistance to supply electrical power to the cavity, one of them close to where the optical power is absorbed on the opposite side of the inclined plane, the other one close to the entrance of the cavity, on the outside the cylinder. Switching between the two heaters is easily done and provides a good check for non-equivalence of electrical and optical heating cycles.

The temperatures of the cavity and reference block are measured using RhFe and Ge sensors soldered into the cavity and reference block. A dummy cavity, close in thermal mass to that of the real cavity is mounted on the reference block using a thermal link similar to that of the real cavity.

Another RhFe sensor is attached to the dummy cavity. The bridge used for measurements of the sensor resistance allows the use of an external standard resistor.

If the RhFe sensor on the dummy cavity is connected to the external standard input, this automatically cancels any remaining fluctuations in the reference block. If the laser beam hits the cavity (irradiated state) the temperature controller reduces the electrical power P_{el} of the cavity heater by exactly the amounts of the absorbed power P_{opt}. If the laser beam is interrupted (non-radiated state) the temperature controller increases the electrical power P_{el} to the initial state. Thus the difference ΔP_{el} of electrical power balances the absorbed radiant power P_{opt}.

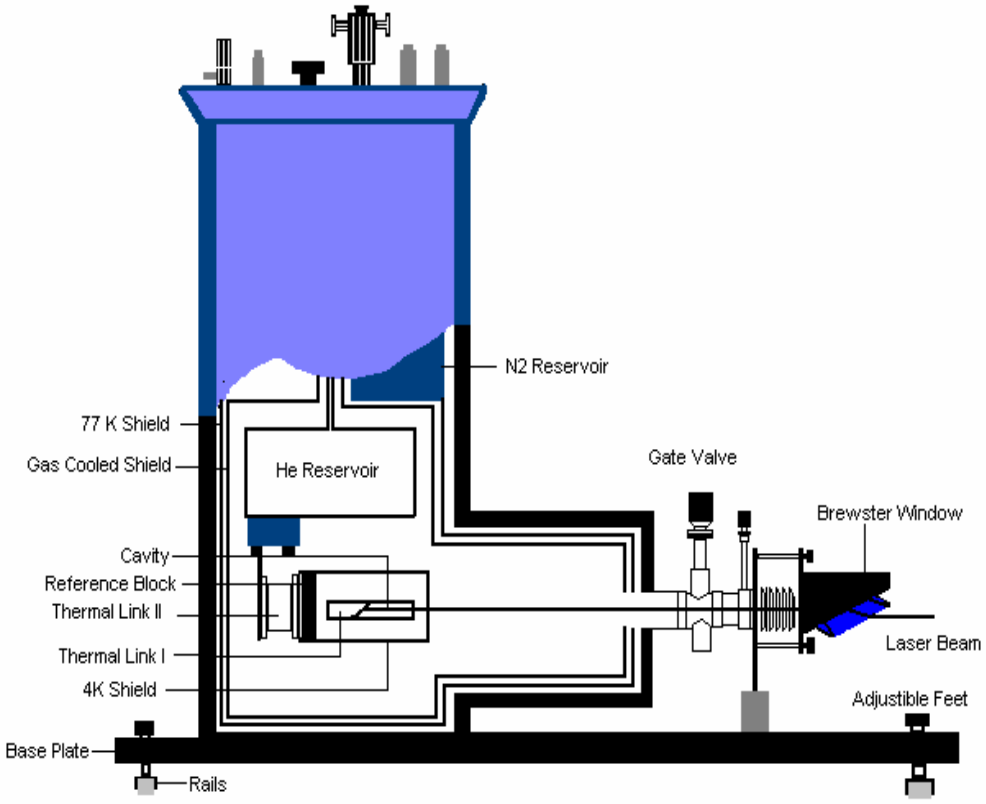

Figure 2.2: High accuracy cryogenic radiometer system.

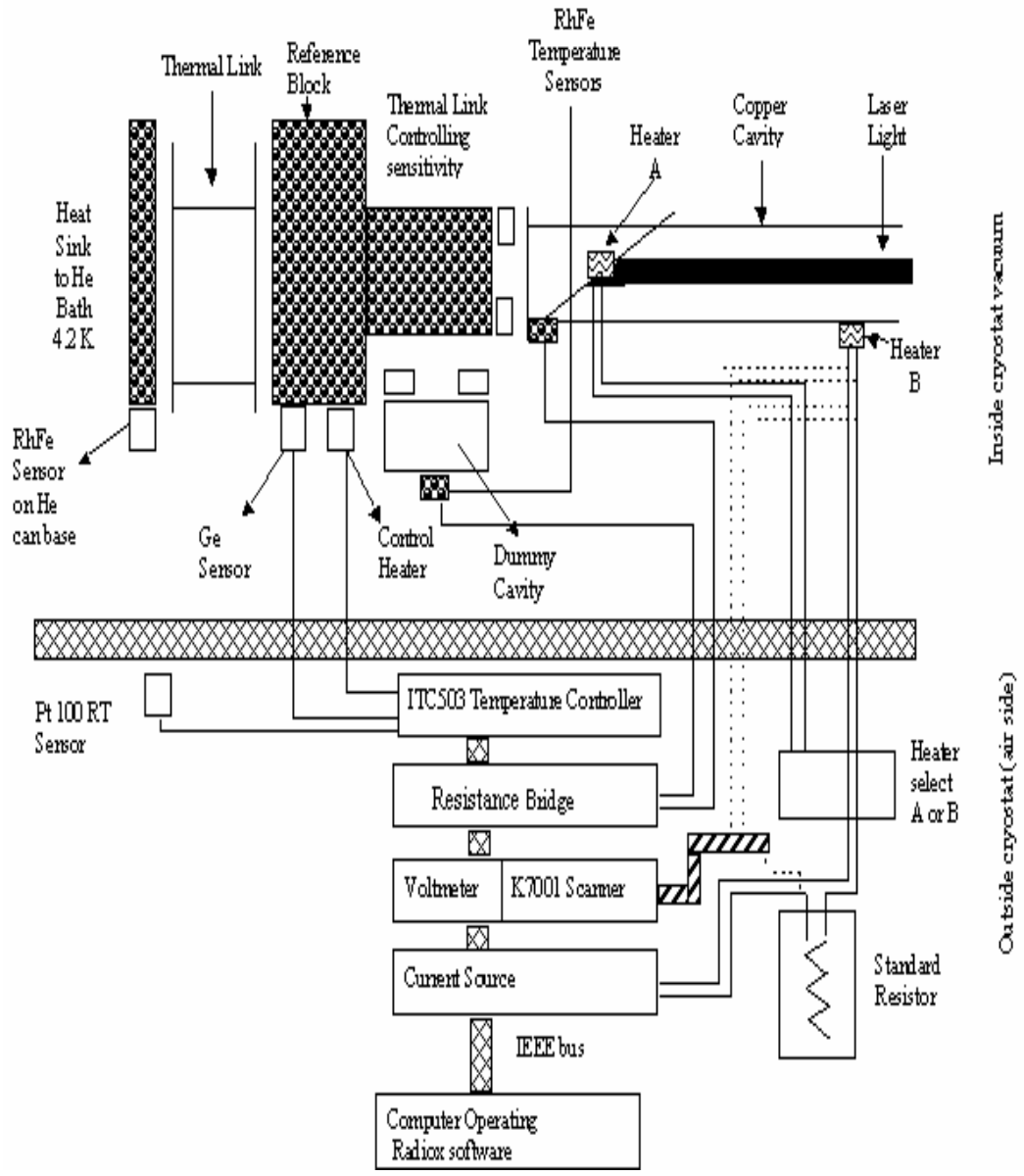

Figure 2.3: Cryogenic Radiometer Wiring and Electronic Scheme.

A digital voltmeter is used in the system for multi-purpose measurements through the scanner. The measuring quantities include the cavity heater voltage, the standard resistor voltage, the scattered light level and the internal temperature of the standard resistor.

2.2.2.1 The Absorptivity of the Cavity

The absorptivity of a diffusely reflecting cavity, α, can be calculated by using either the integral equation method [44] or the series reflectivity method [45,46]; both methods are a function of the physical dimensions of the cavity as well as the surface emissivity. The absorptivity of a specular reflecting cavity can be calculated from the series reflectivity method and is a much simpler calculation involving ray tracing.

The radiometer cavity used in UME optics laboratory was designed in NPL is made of electro-formed copper and is cylindrical in shape. It is 50 mm in diameter and 150 mm long. The front face of the cavity is closed with a plate containing a 10 mm entrance aperture; the other end of the cavity is closed by a back wall inclined at 30° to the cylinder axis. Inside the cavity is coated with a diffusely reflecting Pt black paint (diffuse reflectance of about 1% in the visible region of the spectrum); except the bottom end, which is coated specularly reflecting NiP black paint (specular reflectance of 5% in the visible region of the spectrum). The absorptivity of the cavity has been calculated for a beam of visible radiation entering the cavity through the aperture along the axis of the cylinder. The beam is incident on the back wall and the cavity geometry is designed so that the specular component of the reflection is nearly totally absorbed (99.9998% after the fifth reflection). Consideration need only be given to the diffuse component of the reflection and this has been calculated using the series reflectivity method from the equation [46]

$$\alpha = 1 - \rho \cos\theta r^2 / (r^2 + L^2) \qquad (2.1)$$

where ρ is the hemispherical diffuse reflectance of the wall and θ is the angle of incidence of the beam at the rear wall. From equation 2.1 and using r = 5.0 mm, L = 150 mm, ρ = 0.01 and θ = 60°, the diffuse absorptance of the cavity is calculated to be 0.99999 in any part of the visible spectrum. This value of the cavity absorptance has also been confirmed experimentally by calibrating the cavity absorbance at NPL.

Cavities of this size can obviously be constructed for both ambient temperature ESRs and cryogenic radiometers. However, another factor that must be

taken into consideration when designing a cavity is the time constant: the time taken for thermal equilibrium to become established in the cavity after a power change.

Consider a constant radiant power Q absorbed in a cavity at temperature T_C and connected by a heat link of thermal resistance R to a reference block at temperature T_R. For a small temperature difference $dT = T_R - T_C$ and an incremental time period dt, the heat flow equation can be written as [47]

$$Qdt - (dT / R)dt = CdT \tag{2.2}$$

which can be solved to give the well-known equation

$$dT = RQ(1 - \exp[-t / RC]) \tag{2.3}$$

where C is the thermal capacity of the cavity and is equal to the mass of the cavity times its specific heat. Thus the temperature of the receiver will rise exponentially with a time constant $\tau = RC$. If the cavity is made of copper, then by cooling the cavity from 293 K to 4 K the specific heat of the cavity decreases by about 1000 and τ is correspondingly reduced. τ for the cavity (mass = 5 g) at 4 K has been measured experimentally to be few seconds, whereas at 293 K it would be of the order of many minutes. Therefore, large cavities are impracticable for ambient temperature ESRs and smaller cavities are normally used which cannot be made so highly absorbing and hence require the application of large corrections (with their associated uncertainties) for the incomplete absorption of the incident radiation in the cavity. The advantage of cooling the radiometer to 4 K is that a large cavity can be constructed with a high absorptance and an acceptable time constant.

2.2.2.2 The Electrical Heaters

Heaters used in cryogenic radiometer and their electrical connections are shown in Figure 2.4. The electrical heating of the cavity is usually in the form of

Joule heating by passing a current through an electrical resistance attached to the cavity. Wire heaters wound non-inductively around the cavity, or more recently thin-film heaters deposited directly onto the cavity, have been employed. However, whichever type of heater is used, leads will be necessary to connect the heater to a power supply. Power will also be generated in these leads which it is difficult to account for in the power measurement, but which will cause an additional temperature rise of the cavity. Ambient temperature ESRs have been constructed with various features designed to overcome this problem, but it still remains a source of uncertainty for this type of ESR.

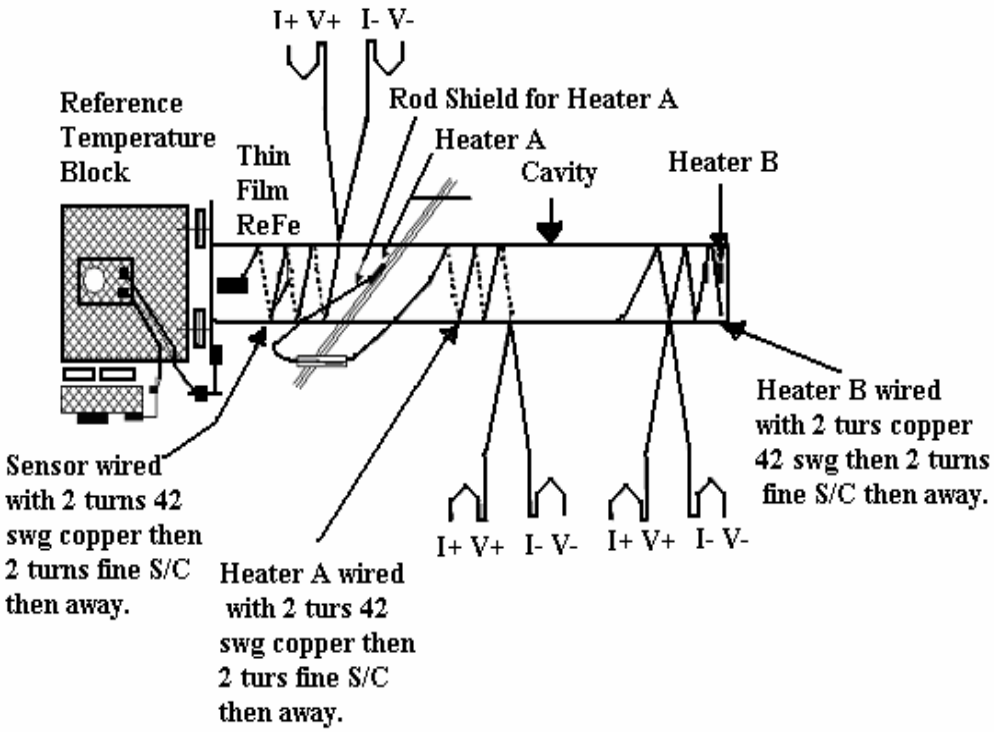

Figure 2.4: Cryogenic radiometers electrical heater system.

A typical heater arrangement for a cryogenic radiometer is shown in figures 2.3 and 2.4. The heaters are located on the cavity; a current from a constant-current source is

passed through the heater and a standard resistance connected in series. The potential differences developed across the resistances are measured with a digital voltmeter. The power generated in the heater is given by

$$P = \frac{V_h V_s}{R_s} \tag{2.4}$$

where V_h and V_s are the voltages across the heater and the standard resistance R_s, respectively [48]. The advantage of cooling the cavity is that superconducting wire can be used to make the final connections between the heater and the reference block. This ensures that all the power is dissipated as heat in the heater windings and that the measurement P is an exact measure of the power supplied. Temperature responses of cavity to the electrical heating of heaters on the cavity (Heater A and Heater B) are shown in the figures 2.5 and 2.6 respectively.

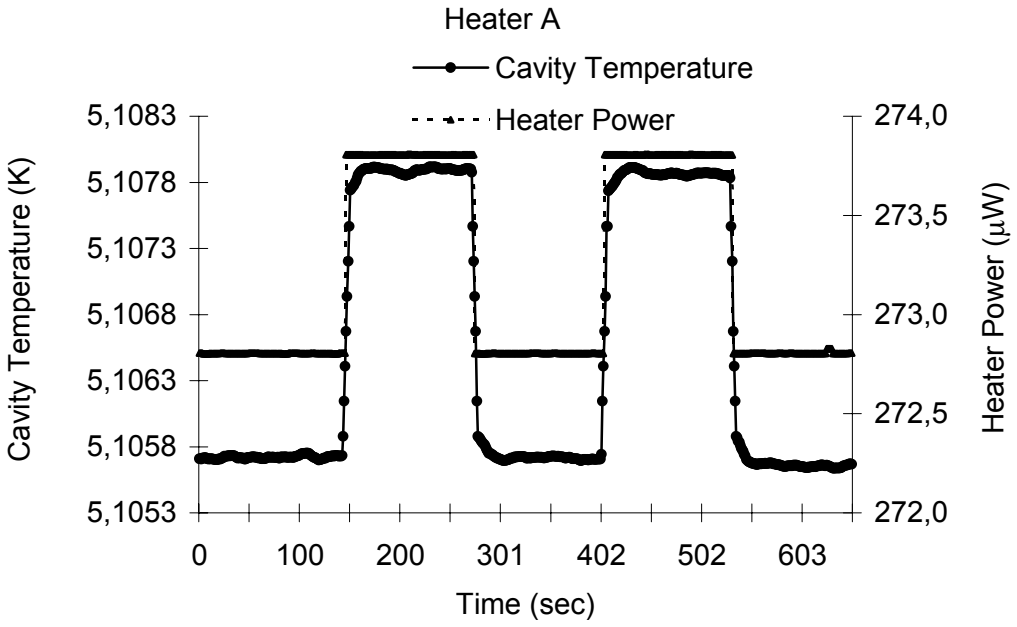

Figure 2.5: Temperature response of cavity to the heater A.

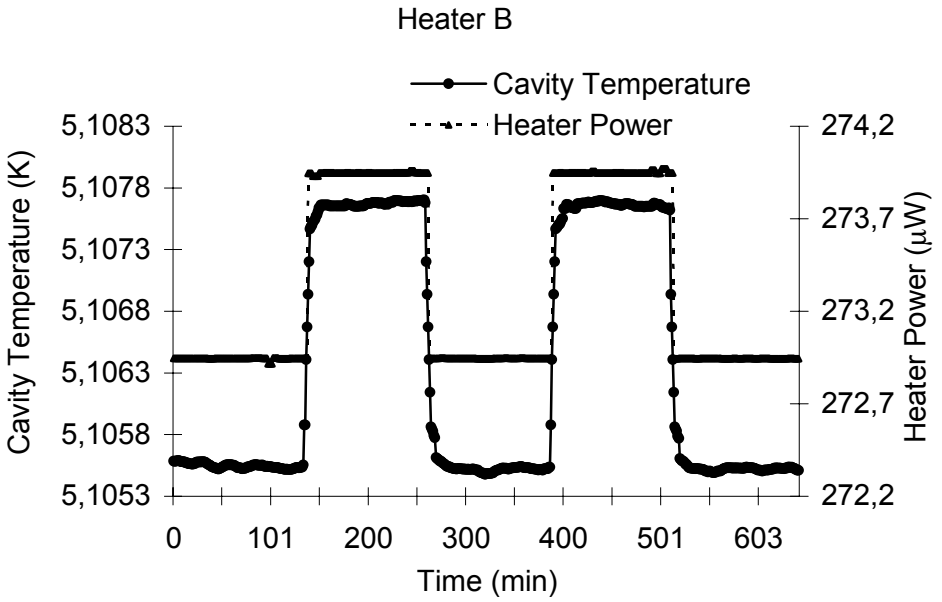

Figure 2.6: Temperature response of cavity to the heater B

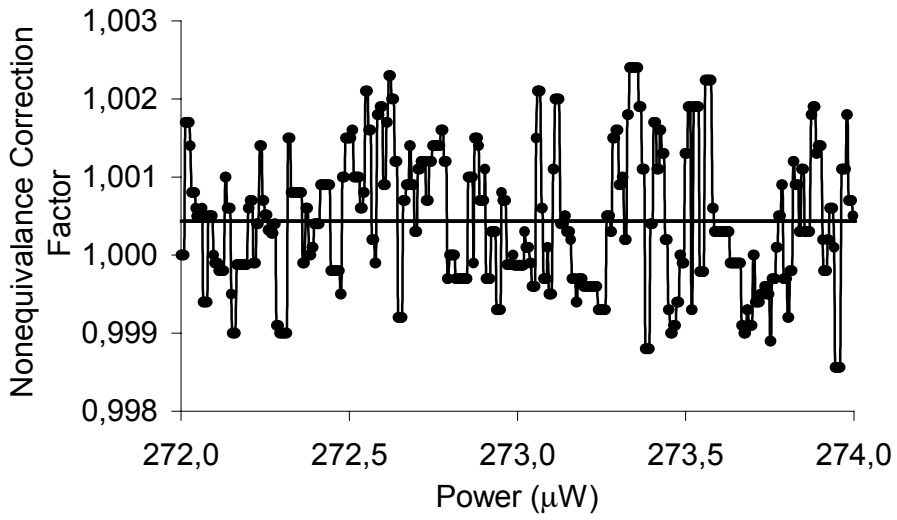

Figure 2.7: Non-equivalence correction factor versus power.

The requirement of electrical substitution cryogenic radiometer is that a given quantity of power absorbed by the cavity will lead to a certain temperature rise regardless of whether the source is electrical or optical. The non-equivalence correction factor for the optical and electrical heating was calculated and shown in the figure 2.7.

2.2.2.3 The Heat Flow Path

A thermally conducting heat path that connects the cavity and the reference block is shown in figure 2.3. To show that the same fraction of heat generated in the cavity, either by the absorption of the radiant flux or by passing a current through the heater, will flow along this heat path by conduction to the reference block the following conditions must be fulfilled [21]:

a) There is no change in the radiative loss from the cavity when the electrical power is substituted for the radiant power.

b) All the leads to the heater are thermally connected to the heat link, thereby preventing an alternative heat conduction path from the cavity.

c) The heater is securely connected to the cavity to prevent overheating when a current is passed.

d) There are no energy losses or gains by conduction or convection during the measurement sequence.

2.2.2.4 The Temperature Sensors

The temperature sensor used to measure the temperature of reference block is a germanium resistance thermometer, GRT. This type of thermometer consists of a small chip of n-type doped germanium supported in a strain-free manner with side

arms for attaching potential and current leads, the chip is enclosed in a capsule, typically 3 mm diameter and 8.5 mm long, filled with helium gas [49]. GRT's temperature range varies from 0.5K to 30K. GRTs are extremely sensitive; 3mV across the sensor produces about 1mK temperature rise between 1.5 and 10 K and hence are very suitable for use in cryogenic radiometers.

The temperature sensor used to measure the temperature of cavity, He reservoir, and heater is rhodium-iron thermometer (RhFe). RhFe has positive temperature constant and its time constant for the non inductively wound heaters is of the order of second, for the thin film heaters it is millisecond. RhFe's temperature range varies from 1.4K to 325 K. Unlike most metals and alloys; dilute RhFe alloys (typically rhodium + 0.5% iron) still have an appreciable change in their resistivity at very low temperatures and, therefore, make good sensing elements for resistance thermometers. Wire wound RhFe thermometers have been available for the past fifteen years [50], but these are physically large devices and not suitable for this application. However, it is now possible to deposit a thin film of RhFe (with the similar resistivity characteristics to those of the wire) on a slab of sapphire, 6 mm x 5 mm x 0.5 mm [51]. A line pattern is then etched on the film and trimmed to give a resistance of approximately 450 Ω at 293 K falling to 40 Ω at 5 K. There are possible advantages, which are at present being experimentally assessed, for using this device instead of a GRT as the cavity thermometer. These include:

a) Better thermal contact to the cavity as the thermal anchoring of the leads is less critical,

b) A higher measuring current can be used (100 μA) before the self-heating of the thermometer becomes unacceptable,

c) The resistance of the thermometer can be measured more easily with this higher measuring current using commercial a.c. resistance bridges (a.c. measuring systems have advantages over d.c. systems, for example, in that thermal e.m.f. effects are eliminated),

d) The response, $\delta\Omega/\delta T$, for any thin-film RhFe thermometer of the same type is virtually identical over the temperature range 5 to 10 K (this is not the case for a GRT). Hence, if a thin-film thermometer is also used to measure the

temperature of the reference block, then the resistance ratio of the reference block thermometer vs. the cavity thermometer (which can be measured on one bridge circuit) will remain constant for small fluctuations of the reference block temperature.

In conclusion, the temperature sensor is not a limiting factor in the accuracy of either an ambient temperature or cryogenic radiometer.

2.2.2.5 Temperature of Reference Block

The reference block shown in figure 2.3 is a block of copper, which is connected to the liquid helium reservoir. The temperature of the block is controlled near 4.2 K with a stability of better than 10^{-5} by a temperature controller and an ac resistance bridge again; the high thermal diffusivity of copper facilitates this control [48]. This constant temperature provides a reference temperature for the relative temperature measurements of absorbing cavity. Because of the high thermal diffusivity (thermal conductivity/specific-heat capacity) of metals at low temperatures, it is relatively straightforward to control the temperature of a block of copper to a few tenths of a mK.

2.2.2.6 Radiometer Sensitivity

Radiometer sensitivity is determined by two parameters:

a) The fist one is the temperature rise of cavity for a given power input, the greater the temperature rise the greater the sensitivity. The temperature rise can be calculated with the following equation that is a function of the thermal conductivity of the heat link and its physical dimensions [52].

$$Q = \frac{CA(T_C^{2.35} - T_R^{2.35})}{2.35L} \tag{2.5}$$

where C is the thermal conductivity, A is the cross sectional area and L is the length of heat link.

b) The second parameter is the responsivity of temperature sensor.

2.2.2.7 Temperature Ranges of Cryogenic Radiometer

The upper temperature limit of cryogenic radiometer is the critical temperature of the superconductor used for the heater leads and is about 10 K. It is possible that with the development of high temperature superconductors this limit will be increased and the constraint may then arise from decreasing thermal diffusivity and the radioative losses from the cavity.

The lower limit is fixed by the temperature of reference block. Using ^{3}He cryostat or dilution refrigerators the lowest achievable temperature using pumped ^{4}He bath is about 0.8 K. But it has been shown that problems can arise if the cavity temperature is in the region of 3.5 K and blow because in this temperature region hydrogen gas, the major component of residual gas in the vacuum chamber condenses [52]. The exact temperature for condensation take place is unique to each radiometer depending upon the gas pressure of the system.

2.2.2.8 Power Ranges of Cryogenic Radiometer

Because of temperature limits there are problems with maximum and minimum power using cryogenic radiometer. The upper limit will be influenced by three factors [52]:

a) The boil rate of liquid helium reservoir, since all the power absorbed in the cavity will eventually pass in to the liquid;

b) The temperature stability of reference block, this will be more difficult to achieve with a large heat flow;

c) A large heat flow might create significant temperature gradient in the cavity.

The lower limit will be influenced by two principle factors:

I. The sensitivity of temperature sensing, which may in turn be limited by the thermal anchoring the heater and thermometer wires to the cavity;
II. The changes in the radiant losses from the cavity due to fluctuations in the temperature of surroundings.

As a conclusion the lower limit should be of the order of microwatt and upper limit should be milliwatt.

2.2.3 Measurement Preparations

The radiometer was evacuated to a pressure of about 10^{-5} Pa (10^{-7} Torr) using turbo molecular pumping system. Then nitrogen and helium reservoirs were filled with liquid nitrogen and after 12 hours the helium reservoir was emptied and liquid helium was transferred into it. The cavity took about 2 hours to cool from 77 K (liquid nitrogen temperature) to 4.2 K (liquid helium temperature). The radiometer was maintained in the cooled condition and ready for immediate use. The accuracy of measurements using the cryogenic radiometer strongly depends on the power stabilization of the laser beam, cleaning and the transmittance measurements of Brewster window and minimization of scattered light.

2.2.3.1 Power Stabilization of Laser Beam

In ESCR, high accuracy measurements can be obtained using a collimated and polarized light with a typical power level of 1mW. This is only achieved by using laser sources because of high intensity, monochromatic and geometrically well-defined beams. However, lasers have unstable power, that is, their power fluctuates in time. These undesired fluctuations could be compensated using laser power stabilizer systems (LPS). In order to compensate fluctuations in the optical power and generate a geometrically well-defined Gaussian laser beam, LPS system was used which is shown in figure 2.8.

The LPS consists of an electro-optic modulator (EOM), a calibrated beamsplitter, a temperature controlled monitor photodiode and control electronics to monitor and operate the first two elements. This instrument is a precision instrument for measuring, modulating and stabilizing laser beam power. The LPS uses a liquid crystal cell (calcite) to perform the attenuation as shown in figure 2.9 a and b. Besides optical power control setups, calcite is also used for optical beam polarization and phase control systems [53].

As a laser stabilizer, the LPS contain a servo, which removes drift and power-supply noise from the beam. Optics module consists of laser input and output apertures of 4 mm diameter, mounting holes, neutral density filter (ND) (figure 2.10) switch for controlling lasers in excess of 200 mW.

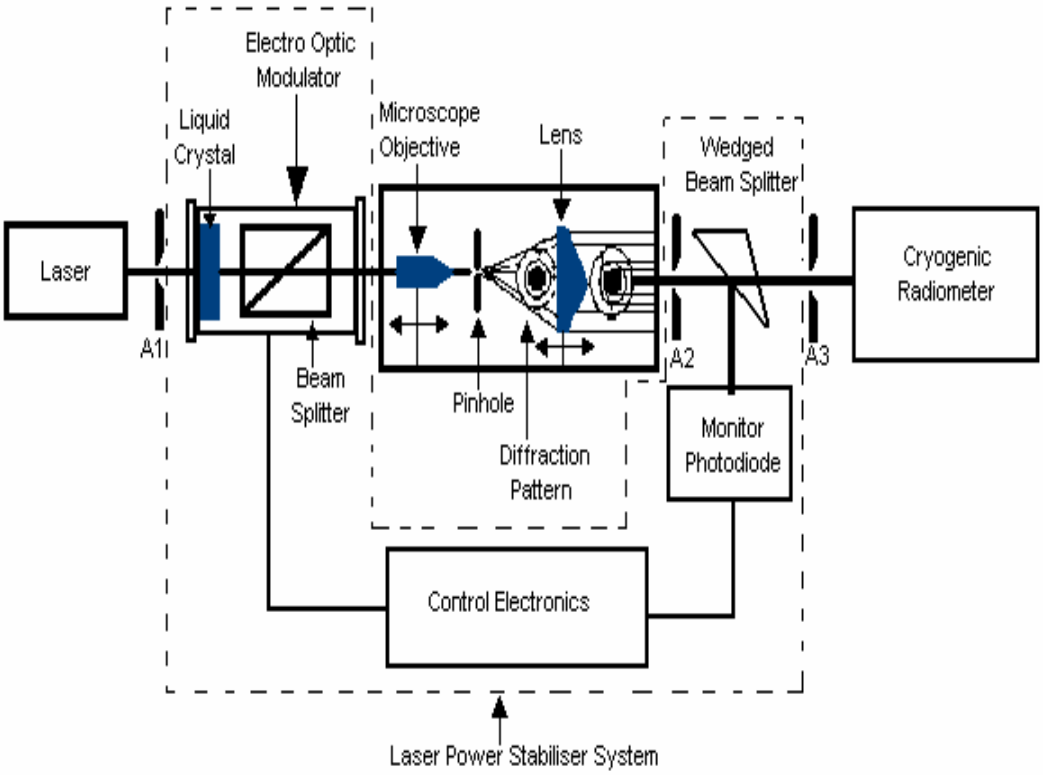

Figure 2.8: Laser Power Stabilizer System, A1, A2 and A3 are apertures.

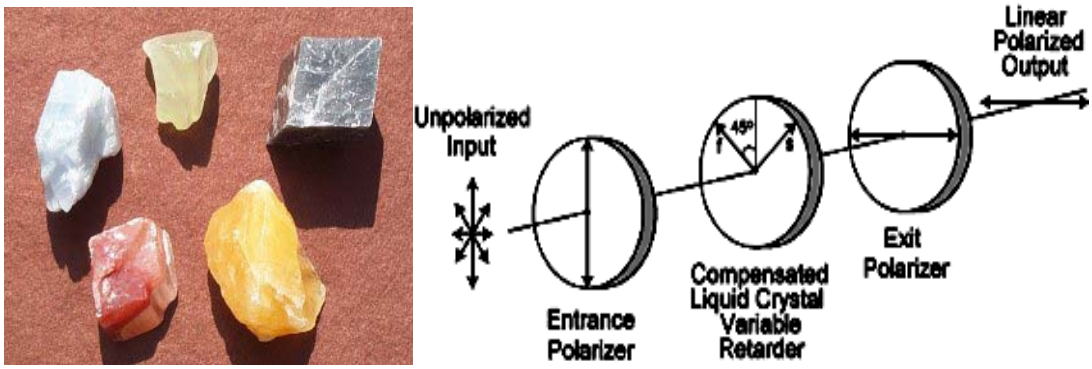

(a) (b)

Figure 2.9: a: Calcite crystal, b: polarizer made from calcite.

(a) (b) (c)

Figure 2.10: Neutral density filters and their effect on the photographs.

ND filters are the camera's equivalent of colourless sunglasses. They simply reduce a scene's brightness without changing colour [54]. ND filters are used excessively by photographers; in figure 2.10. b and c effects ND filter on the photograph is illustrated. Vertically polarized laser light incident on the LPS 's optics

module first passes through a liquid crystal modulator, which variably dims the beam, through electro-optic modulation. The light passes through a field aperture to a precision beam splitter, which transmits %98 of the incident light. The optical beam after passing through the EOM partially reflected from the wedged fused-silica beam splitter. In figure 2.11, you can see a wedged beam splitter. Here a wedged beam splitter is used because with parallel substrates the second surface reflection can overlap the first surface reflection and lead to unwanted spectral channelling [55]. The higher the parallelism, the worse the problem. This is true for beams with a coherence length longer than the thickness of the substrate. The reflections from the surface of the wedge are not parallel and also slightly separated. The reflected beams from a wedged beam splitter separate as you move away from the beam splitter and so allow you to use the reflection from only one surface. You should avoid overlap of reflected beams when using a laser or narrowband monochromatic source.

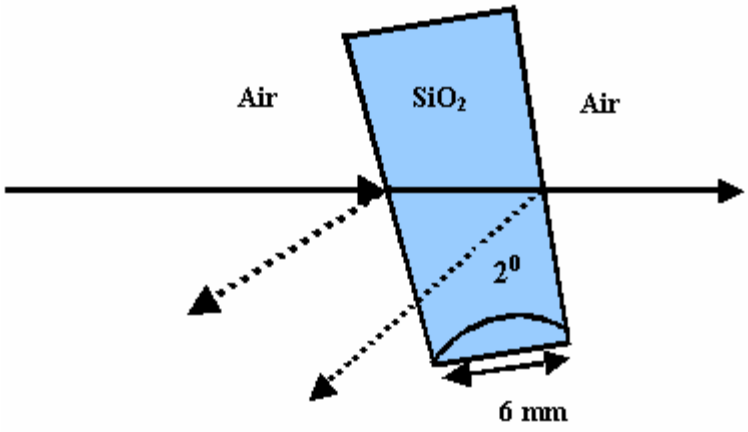

Figure 2.11: Wedged beam splitter.

Precision monitor photodiode receives the reflected beam from the wedged window and send it back to the EOM. Monitor photodiodes are generally used in

constant power circuits, because they provide a current output proportional to the light input, and that current can be used by a feedback mechanism to adjust the optical power [56]. To insure maximum accuracy, the temperature of this photodiode is servo-controlled to a constant 33±0.05 °C. This temperature control eliminates long-term drift and error due to detector temperature variations. The feedback loop controls the power in the optical beam so as to get the constant signal. In about 30 minute the desired stability can be reached. In the figures 2.12-2.15, power stabilization of Ar^+ , Nd:YAG, and He-Ne laser beams between 30-180 minute time intervals are displayed. The time required for stabilization is approximately 30 minutes, and the stability achieved for each laser is at few parts in $10^{-5.}$

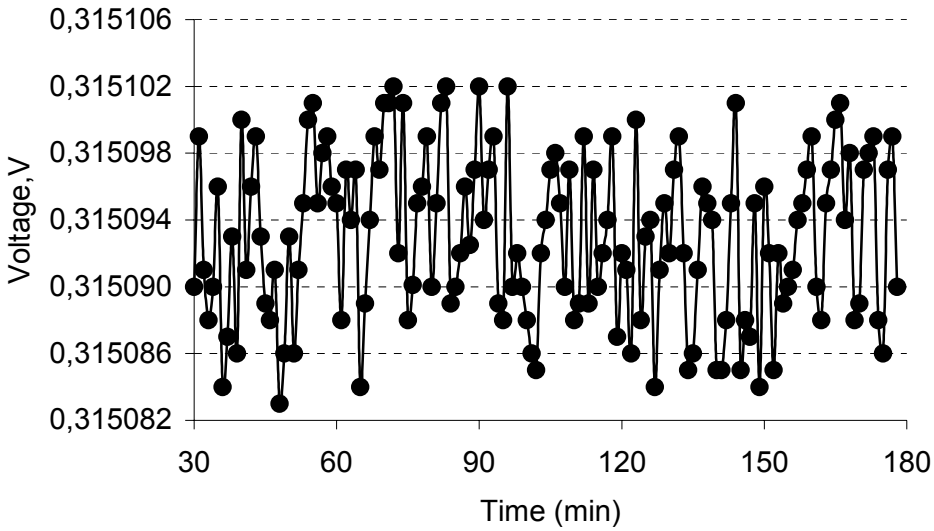

Figure 2.12: Variation of stabilized Ar^+ (488.0 nm) laser beam in time

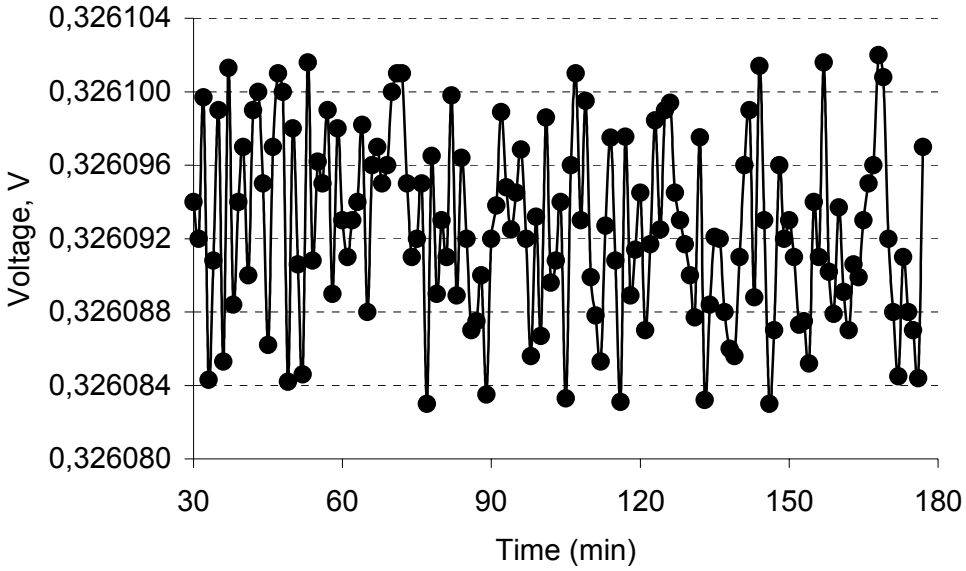

Figure 2.13: Variation of stabilized Ar^+ (514.5 nm) laser beam in time

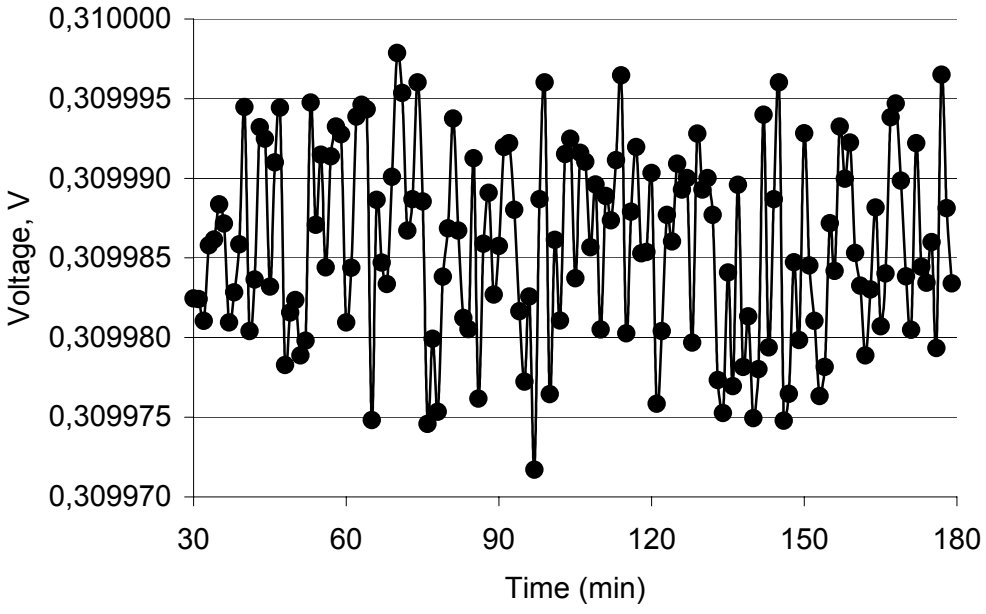

Figure 2.14: Variation of stabilized Nd:YAG (532 nm) laser beam in time

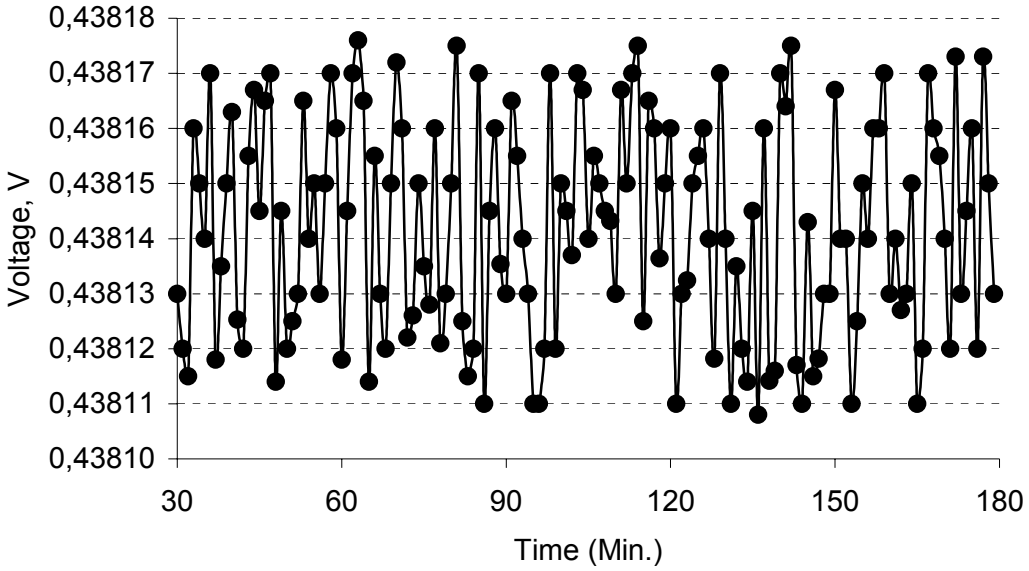

Figure 2.15: Variation of stabilized He-Ne (632.8 nm) laser beam in time

A microscope objective (x10), a pinhole (25 μm in diameter) and a collimating lens were used to produce a clean Gaussian laser beam (TEM00) (figure 2.16 a) with a suitable dimension. By slightly defocusing the laser beam into the pinhole airy diffraction patterns (figure 2.16 b) were created. Then, by using suitable recollimating lens in front of the diffracted beam, the beam of 3 mm diameter ($1/e^2$ points) was obtained. Please note that the dimension mentioned here is the dimension of the bright spot at the centre of diffraction pattern. A variable iris was used to allow only this bright spot to pass through. To measure the beam shape of the lasers used in the measurements a CCD beam analyser was used in the figure 2.8 after the wedged beam splitter. The recorded beam shapes of lasers are shown in the figure 2.17.

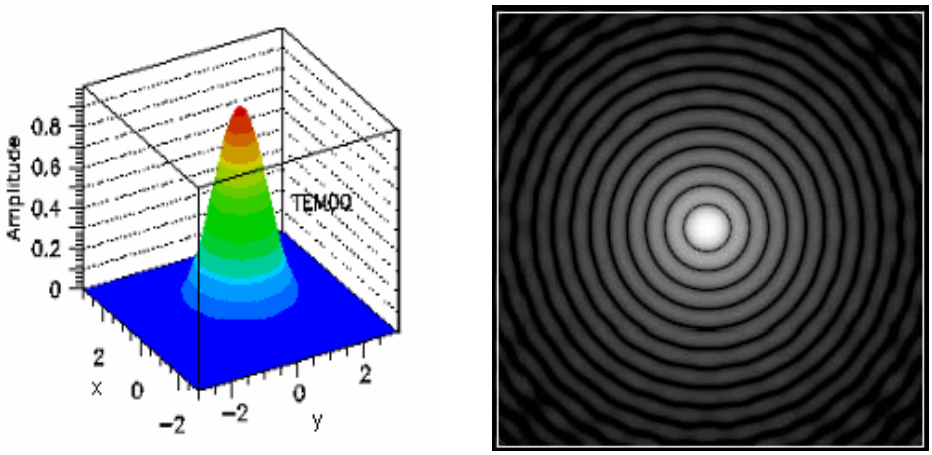

(a) (b)

Figure 2.16: a: Gaussian beam, b: diffraction pattern.

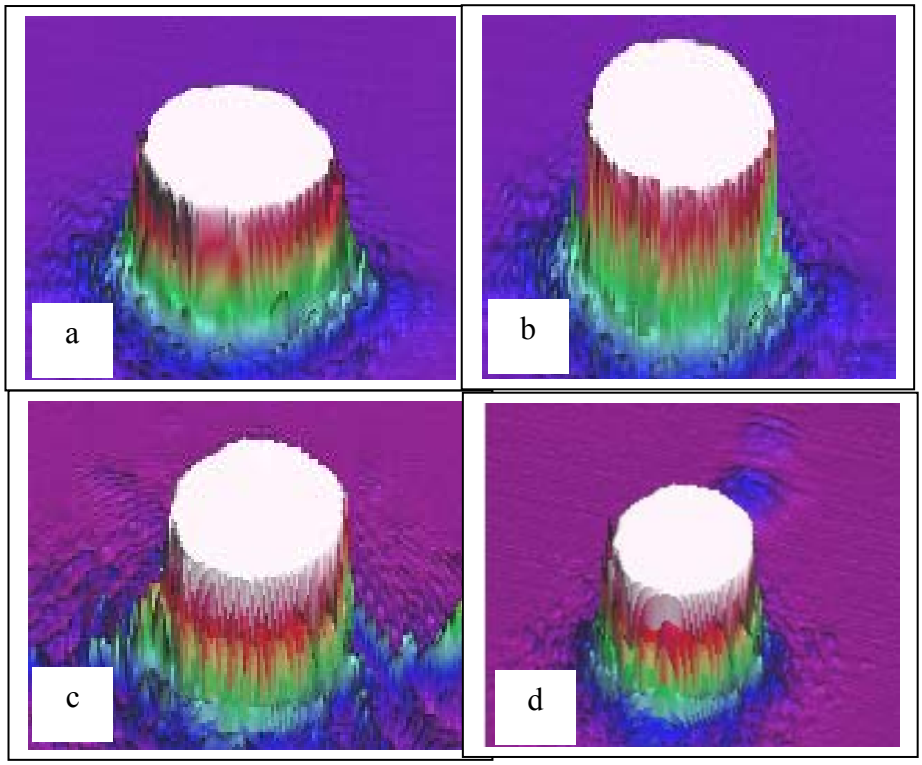

Figure 2.17: Beam shape of lasers used in the measurements a) Ar^+ at 488 nm, b) Ar^+ at 514.5 nm, c) Nd:YAG at 532 nm and d) He-Ne at 632.8 nm.

2.2.3.2 Transmittance Measurements of Radiometer Entrance Window

Generally window itself has the major contribution to the uncertainty, because contamination present on the window and deviations from the Brewster angle results unwanted scatter and absorption of the optical beam [47]. Therefore window was released and cleaned using suitable solutions like ethanol, and lens paper with drop and drag method and process repeated until the 0.999 transmittance was achieved [57]. Then window was placed on a gimbal holder (figure 2.18 a) and adjusted to Brewster angle.

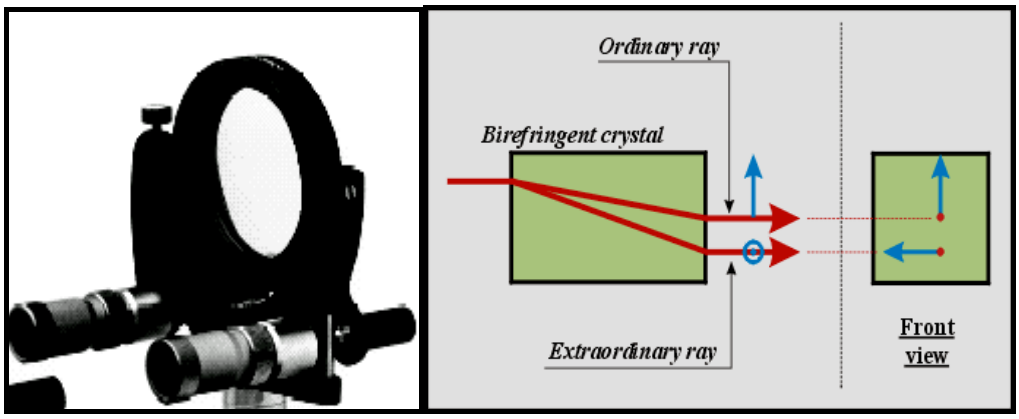

(a) (b)

Figure 2.18: a-Gimbal holder, b-birefringence effect of liquid crystal.

The transmittance of Brewster angle window was obtained by taking the ratio of the signals measured from silicon based trap detector when the window was present and not present in the path of the optical beam (Figure 2.19). Theoretically vertically polarized laser beam should pass through the window without any loss at the Brewster angle but when lasers pass through the EOM due to Kerr effect their polarization is affected [58]. Kerr effect is the development of birefringence (figure

2.18.b) when an isotropic transparent substance is placed in an electric field. Birefringence is the division of light into two components (an "ordinary" η_0 and an "extraordinary ray"η_e), found in materials, which have two different indices of refraction in different directions (i.e., when light entering certain transparent materials, such as calcite, splits into two beams which travel at different speeds). Birefringence is also known as double refraction [58]. In order to reform the polarization a Glan-Laser polarizer is located behind the wedge beam splitter (Figure 2.20). Glan-Laser polarizer is an air spaced calcite polarizing prism mounted in black anodized aluminum housing for use with low to medium power lasers black anodized aluminum housing for use with low to medium power lasers. The measurements carried out with and without using polarizer are displayed in table 2.2.

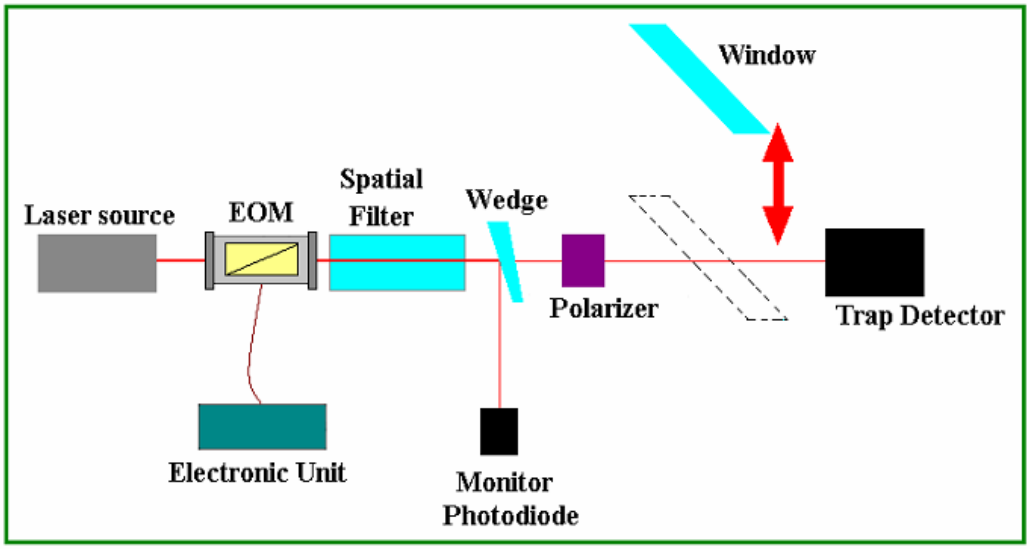

Figure 2.19: Transmittance measurement set up for the window

As shown in table 2.2, extra polarizer enhances the transmittance, and at all wavelengths the transmittance better than %99.9 was obtained. After completion of

window transmittance, it was remounted to the radiometer entrance and the window chamber evacuated for at least one hour. Then window was adjusted for minimum reflection to obtain the Brewster angle.

Table 2.2: Transmittance measurements of window at Brewster angle

Wavelength, λ (nm)	457.1	488.0	514.5	532	632.8	1064
Transmittance, T % (without polarizer)	99,865	99,872	99,875	99,875	99,883	99.891
Transmittance, T % (with polarizer)	99.948	99.949	99.961	99.961	99.961	99.962
Uncertainty (parts in 10^5)	9.5	5.0	4.8	4.6	4.1	9.1

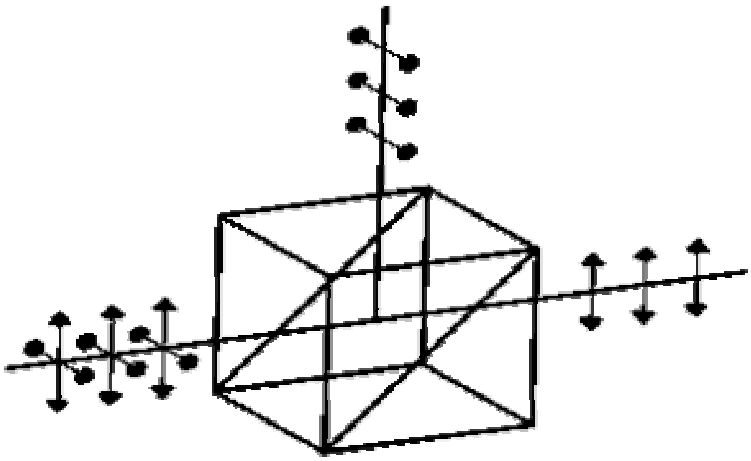

Figure 2.20: Glan Laser polarizer.

2.2.3.3 Minimization of Scattered Light

Stabilized and vertically polarized optical beam enters to the radiometer through the window inclined to Brewster angle. Absorbing cavity is about 50 cm behind the window. A quadrant photodiode (Figure 2.21) with 45 mm diameter active area and 9 mm diameter central hole is located close to the entrance of the absorbing cavity. Quadrant photodiode is one type of detector, which is used for the detection of position of the laser beam. It consists of four photodiodes arranged in four quadrants of a circular structure. These photodiodes are electronically connected in quadrature to compare the intensity in each half of the beam, both horizontally and vertically. There is null signal from the quadrant photodiode when all the four quadrants receive same amount of light. If the beam is displaced from the center, we get the output from the quadrant photodiode. This output is the measure of the displacement of the beam and the sign of the output indicates the direction of displacement. To get accurate measurements the laser beam should be Gaussian, as it is now in our case. The optical beam enters the cavity passing through this aperture (Figure 2.22).

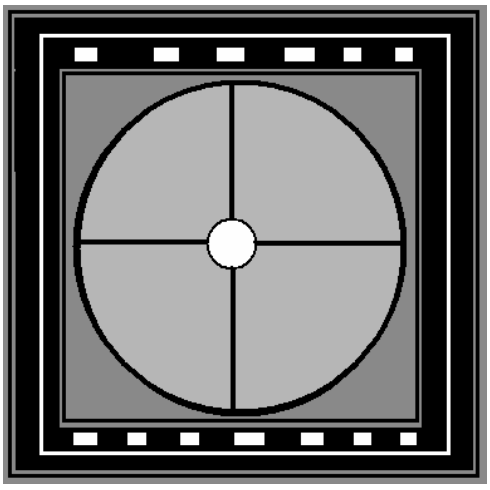

Figure 2.21: Quadrant photodiode.

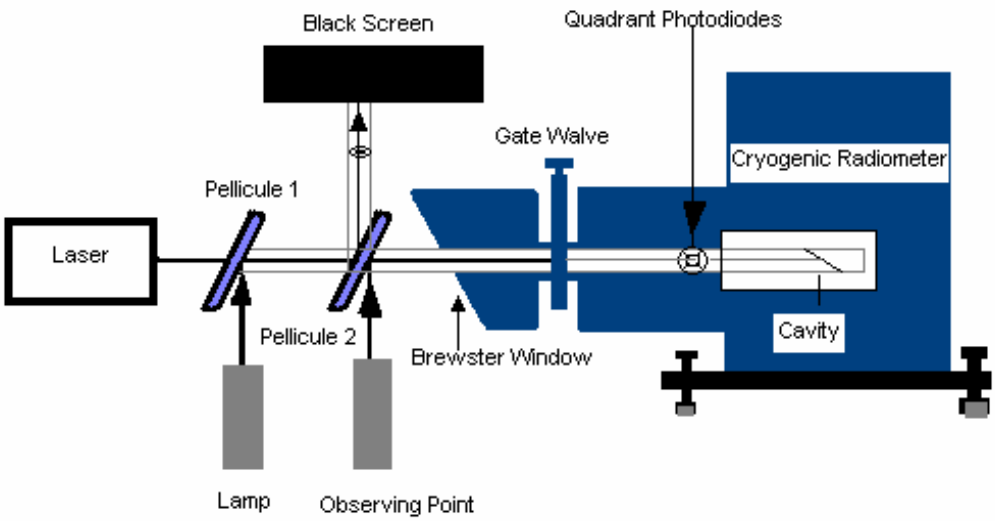

Figure 2.22: Set up for the minimization of scattered and adjustment of light into the cavity.

The part of the beam that is not aligned and scattered due to window falls on the quadrant photodiodes. In order to minimize the fraction of the beam incident to quadrant photodiodes optical beam was aligned using the method described in [57]. Namely, the optical beam path was closed with the gate valve present about 10 cm behind the window. Then two pellicule beam splitters were aligned to 45° with respect to optical axis, pellicule is a French word-meaning camera. First pellicule was illuminated with a lamp. The illuminated path and the optical beam strikes to the gate valve were observed on the blackened screen through the second pellicule. The radiometer was adjusted until the optical beam passed at the center of illuminated path. Then the gate valve was opened and the precise adjustments were done until the optical beam entered to the cavity. Scattered portion of beam is observed from the quadrant photodiodes (Figure 2.23). The radiometer was then carefully aligned until the signals from quadrant photodiode were minimized. The optical power detected from these photodiodes was summed and this result was noted as correction value of scattered laser light for optical power measurements.

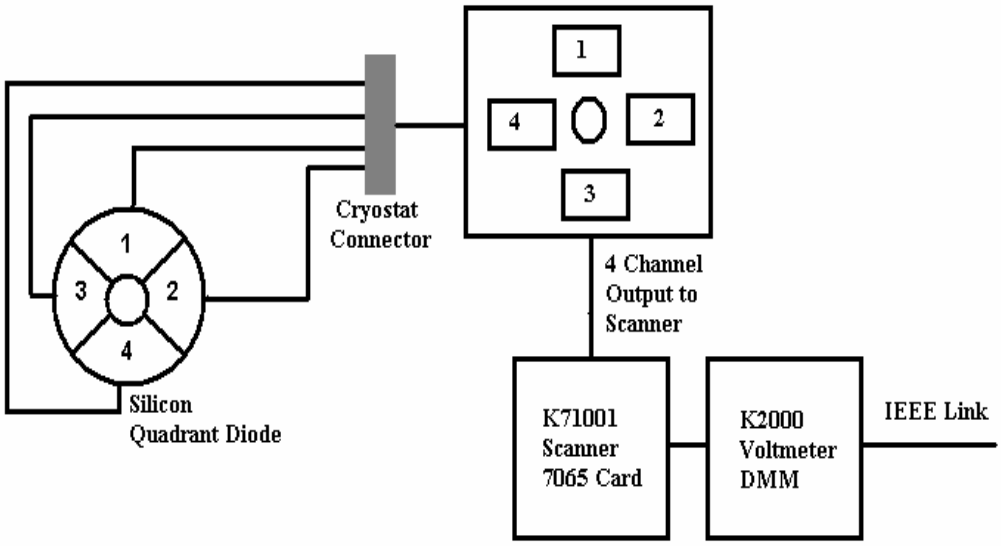

Figure 2.23: Quadrant Diode Wiring Rotue in Cryogenic Radiometer.

2.2.4 Measurement and Calculation of Laser Power

Optical power measurements were performed using static substitution method. This method based on sandwiching optical temperature between two electrical temperature points. The range of estimated electrical power levels applied to give temperature slightly above and below the optical temperature is determined with thermal link calibrations and they should not be less than the cavity sensivity. Hence, before starting the optical power measurements thermal link calibration of the cavity has to be done to determine the cavity sensivity. Thermal link calibration correlates power with temperature by applying series electrical powers to the cavity (Figure 2.24).

In the static substitution method a measurement cycle consists of three optical points (which should all be identical temperature) and two electrical points calculated to be slightly above and slightly below the optical value [59]. The procedure used to find the optical power for a measurement cycle of static substitution method is as follows (Figure 2.25).

a- Optical power is applied to the cavity until its temperature stabilizes,
b- The optical beam turned off and an electrical current is applied such that to obtain the electrical temperature above the optical temperature,
c- The electrical current turned off and optical power is applied again,
d- After temperature stabilization a second electrical-substitution current is applied to obtain the electrical temperature below the optical temperature.

The cycle continues with optical-electrical (high)-optical-electrical (low) as shown in figure 2.25. In order to minimize errors from power fluctuations, measurement cycles were repeated at least twenty times. The optical power was then calculated by using equation 2.6 according to each group of optical and its adjacent electrical powers [59].

$$P_{opt} = P_{iE1} + (P_{iE2} - P_{iE1})\frac{(T_{i,opt} - T_{iE1})}{(T_{iE2} - T_{iE1})} \tag{2.6}$$

where P and T designate power and temperature respectively, the subscript *opt* stands for optical measurement, *iE1* and *iE2* stands for electrical measurements in the i^{th} measurement cycle respectively. The measurements were repeated after 24 hours and it is shown that power variations are almost in the same limits as shown in figures 2.26-2.29.

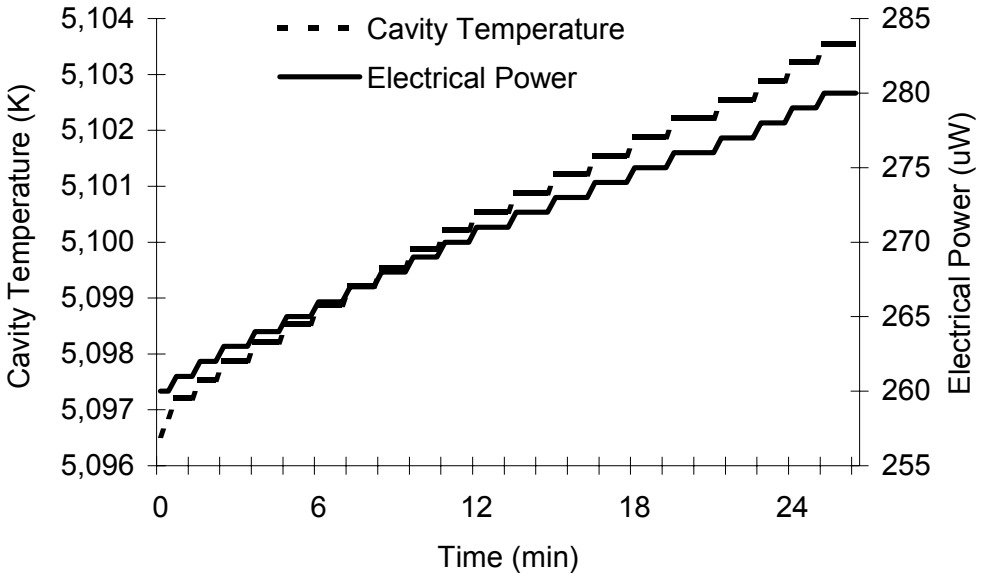

Figure 2.24: Thermal calibration of absorbing cavity.

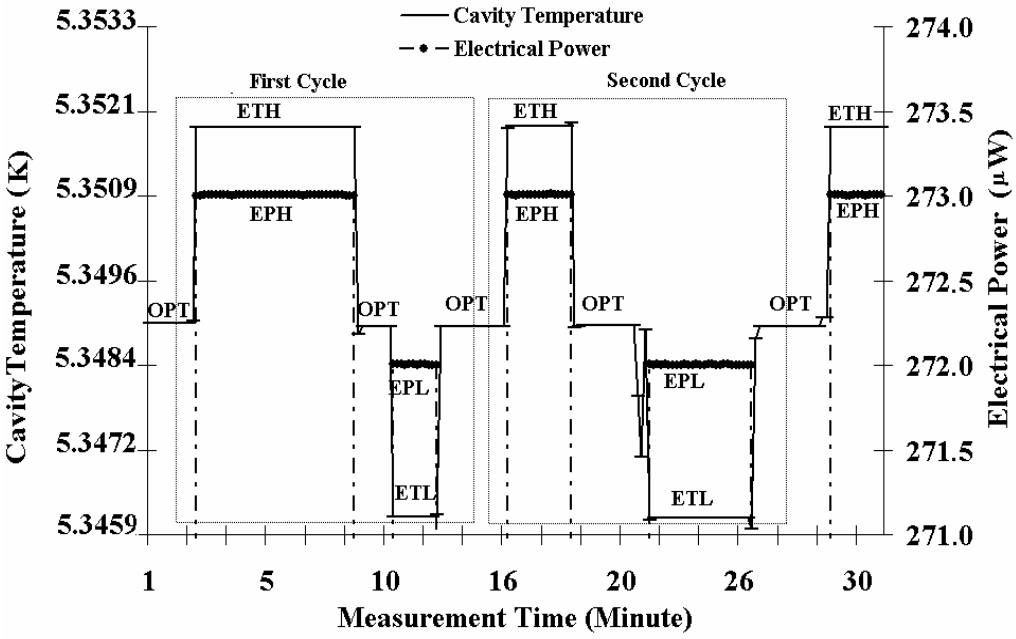

Figure 2.25: Static substitution method for the optical power measurements. OPT designate optical temperature, ETH and ETL electrical high and low temperatures, EPH and EPL electrical power high and low respectively.

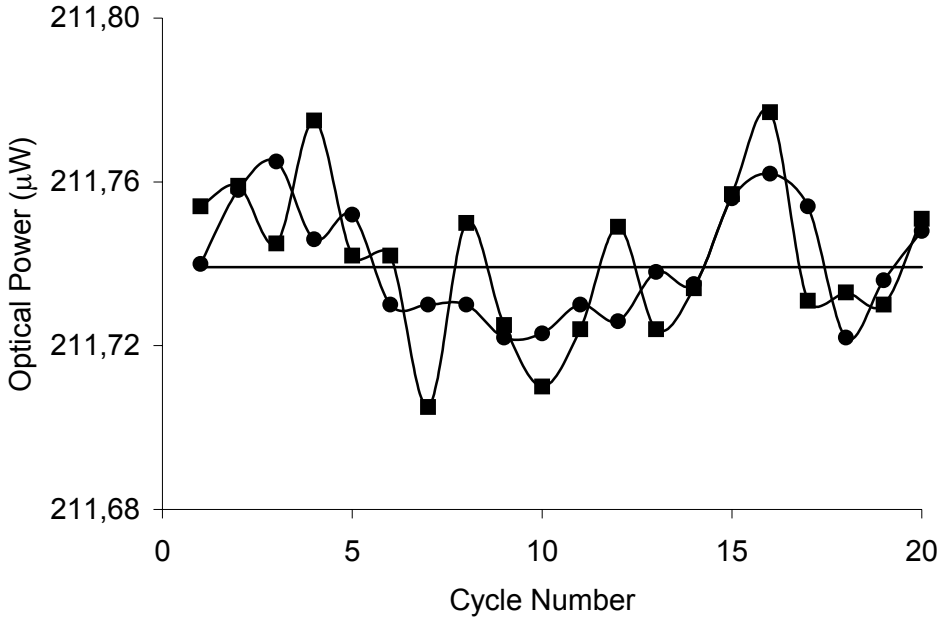

Figure 2.26: Illustration of optical power measurements of Ar^+ (488.0 nm) laser.

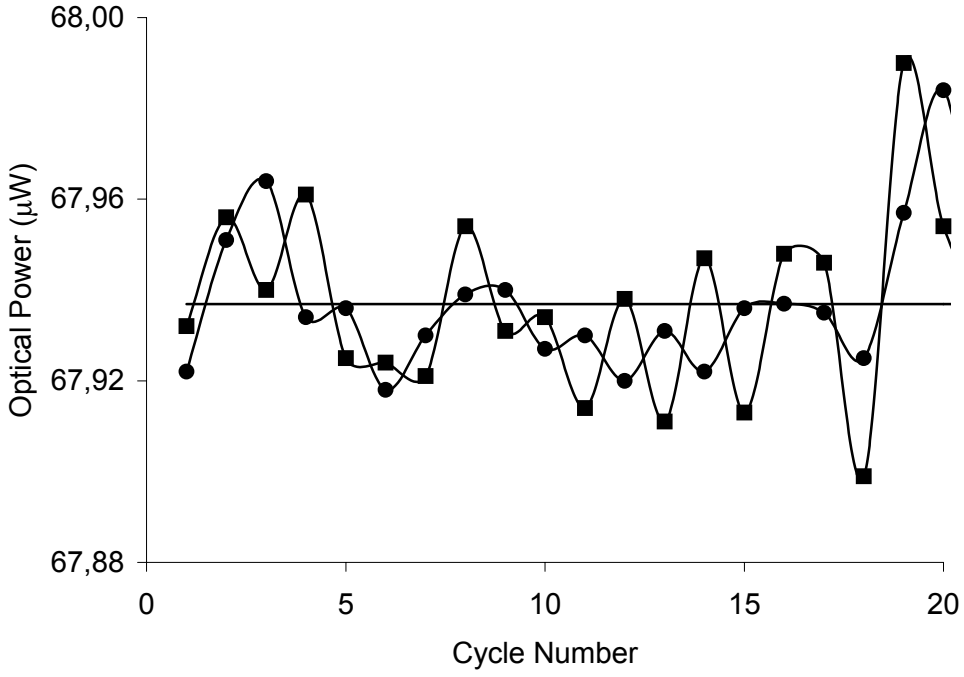

Figure 2.27: Illustration of optical power measurements of Ar^+ (514.5 nm) laser.

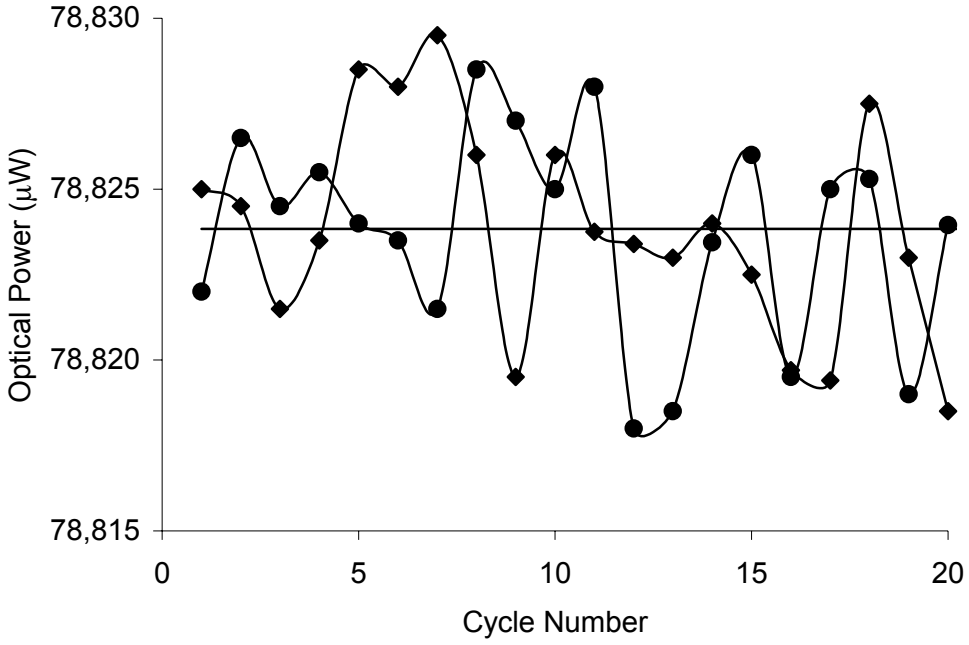

Figure 2.28: Illustration of optical power measurements of Nd:YAG (532 nm) laser.

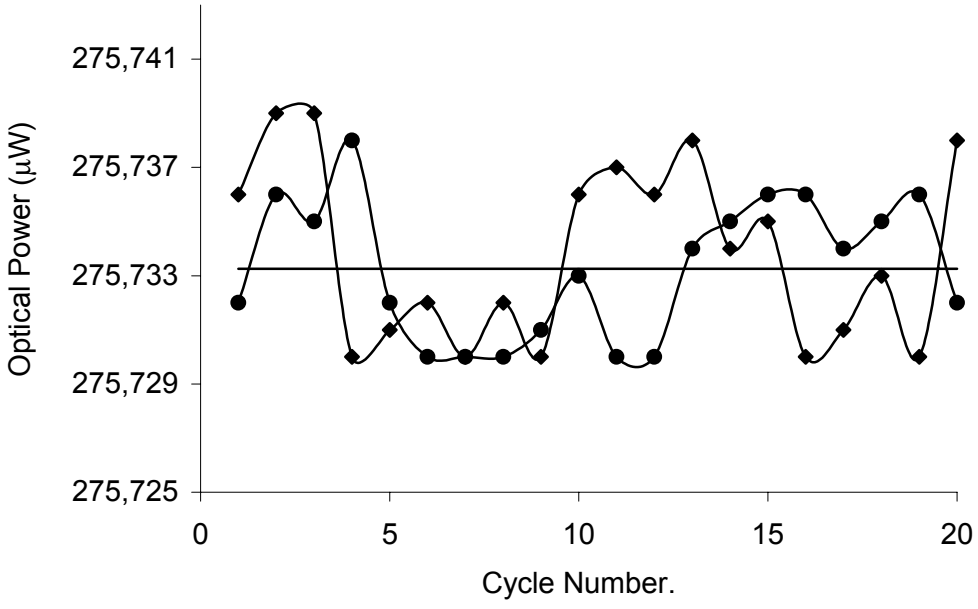

Figure 2.29: Illustration of optical power measurements of He-Ne (632.8 nm) laser.

Since the optical radiation can be reduced by scattering S(λ), by the window transmittance τ(λ),by the imperfect cavity absorbance α(λ),and the optical electrical nonequivalence N, the measured optical power should be corrected for these parameters [60,61] .

$$P_{corr.opt}(\lambda) = \frac{1}{\tau(\lambda)}\left[\frac{NP_{opt}}{\alpha(\lambda)} + \mathrm{S}(\lambda)\right] \tag{2.7}$$

The radiation sources used with our radiometer are Ar+, He-Ne and Nd:YAG lasers. The absolute optical power measurement results and uncertainty in each wavelength are presented in the table 2.3 along with the emission lines of each laser. The combined relative standard uncertainty at each wavelength is shown in Table 2.4. In the table 2.4 various source of uncertainties and their contribution to the optical power measurements were calculated at 632.8 nm according to guide to expression of uncertainty measurements in 1993, and listed as an uncertainty budget [62].

Table 2.3: Optical power measurements at various laser wavelengths and corresponding uncertainties

Laser	Wavelength (nm)	Optical Power (μW)	Combined Uncertainty Parts in 10^4
Ar+	488.0	66.342	1.26
Ar+	514.5	66.199	1.26
Doubled Nd:YAG	532	489.128	1.26
He-Ne	632.8	275.977	1.26
Nd:YAG	1064	501.601	1.53

Table 2.4: Uncertainty budget for optical power measurement at 632.8 nm wavelength

Source of uncertainty	Relative standard uncertainty x 10^{-4}
Optical Temperature	0.02
Electrical Temperature	0.01
Electrical Power	0.11
Window Transmittance	0.32
Scattered Optical Power	0.23
Cavity Absorbance	0.05
Repeatability of Optical Power Measurements	0.45
Non-equivalence	0.15
Expanded uncertainty (k=2)	1.26

CHAPTER 3

TRANSFER STANDARDS AND REALIZATION OF ABSOLUTE SPECTRAL RESPONSIVITY SCALE

3.1 Trap Detectors

To link the high accuracy measurements obtained from the ESCR to the other optical power measurements, trap detectors have been used as transfer standards [26]. Trap detectors are constructed from single photodiodes, arranged in such a way that a beam reflected from a photodiode surface is always directed to the surface of another photodiode. The number of photodiodes in a trap detector varies from 3 to 6. The basic idea behind the trap detector construction is to reduce the high reflectance of a detector consisting of a single photodiode.

Trap detectors constructed in UME are reflection type trap detectors, shown schematically in figure 3.1 consists of three Hamamatsu S1337-11 windowless photodiodes (Figure 3.2). Diodes are arranged in such a way that incoming beam undergoes five reflections. In this process most of the incoming radiation is absorbed and the residual beam is returned back along the incoming beam. Moreover, in this arrangement sensitivity of photodiodes to the polarization of incident radiation is removed.

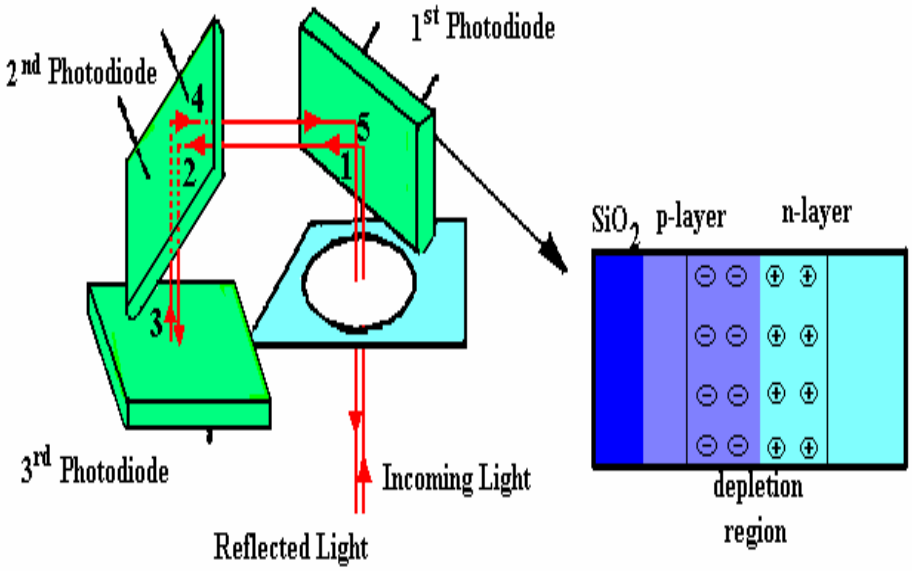

Figure 3.1 : Internal structure of trap detector silicon photodiode

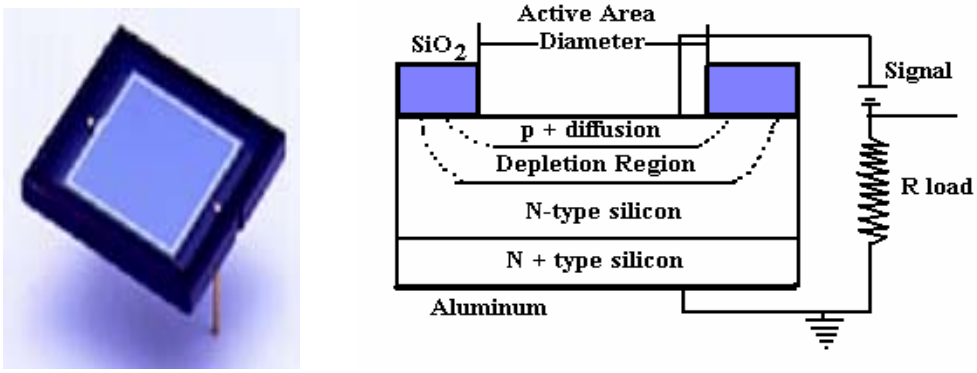

Figure 3.2: Illustration of single photodiode and its internal structure

3.2 Optical Characterizations of Trap Detectors

The characteristics and influence parameters of trap detectors were studied carefully, having in view their use as transfer instruments. The characteristics that trap detectors should have are [25-26]:

a- Low noise equivalent power;
b- Polarization independency;
c- Low non linearity;
d- Good spatial uniformity;
e- Good temporal stability;
f- Low reflectance losses;
g- High quantum efficiency;
h- Predicted spectral responsivity in the visible region.

3.2.1 Noise equivalent power (NEP)

One of the important figures of merit, which depends on noise characteristics, is the noise equivalent power (NEP). This is defined as the optical power that produces a signal voltage (or current) equal to the noise voltage (or current) of the detector. The noise is dependent on the bandwidth of the measurement, so that bandwidth must be specified. Frequently it is taken as 1 Hz. The equation defining NEP is [63]

$$NEP = \frac{EAV_N}{V_S(\Delta f)^{1/2}} \tag{3.1}$$

where E is the irradiance incident on the detector of area A, V_N is the root mean square noise voltage within the measurement bandwidth Δf, and V_S is the root mean square signal voltage. The NEP has units of watts/$(Hz)^{1/2}$, usually called "watts per root hertz." From the definition, it is apparent that the lower the values of the NEP, the better are the characteristics of the detector for detecting a small signal in the presence of noise.

We measured the NEP by first measuring the voltage noise at the output of our detectors. This linear spectral density has units of $V \bullet Hz^{-1/2}$. We convert this to an equivalent optical noise by dividing by the responsivity (A/W) and the transimpedance gain (V/A). This yields a NEP with units of $W \bullet Hz^{-1/2}$.

The noise figures of photodiodes used in trap detectors are so good that the lowest detectable power is limited by the operational amplifier used with the detector. By the careful choice of amplifier the noise equivalent power of these photodiodes can be as low as $5x10^{-15}$ W over the visible spectral region.

3.2.2 Polarization Dependency

The responsitivity of good transfer standards shouldn't depend on the polarization state of the beam to be measured. In order to remove the polarization sensitivity, the photodiodes as shown in figure 3.1 are arranged each to lie in different plane. In this arrangement incident beam after five specular reflections emerge from the trap detector with the same polarization as incident beam. Measuring the change in the responsitivity of trap detectors as they were rotated about the linearly polarized beam axis, sensitivity of the trap detectors to beam polarization was checked. Linearly polarized (polarization ratio is 250:1) and power stabilized (better than 10^5) He-Ne laser at 632.8 nm was used as a light source. Detectors were placed in the beam and rotated around the beam axis to examine the effect of rotation of the plane of polarization. Signals from trap detectors were recorded as a function of the rotation angle and normalized to a value obtained at an arbitrarily chosen origin, to detect relative variation of responsitivity. The maximum relative variations were obtained are ± few parts in 10^4 as shown in figure 3.3. This means that any misalignment of detectors would lead to a relative standard uncertainty of about 10^4 in the determination of the responsitivity. Therefore, in order to avoid changes due to misalignment, the detectors must always be oriented the same way with respect to the direction of polarization thought calibrations.

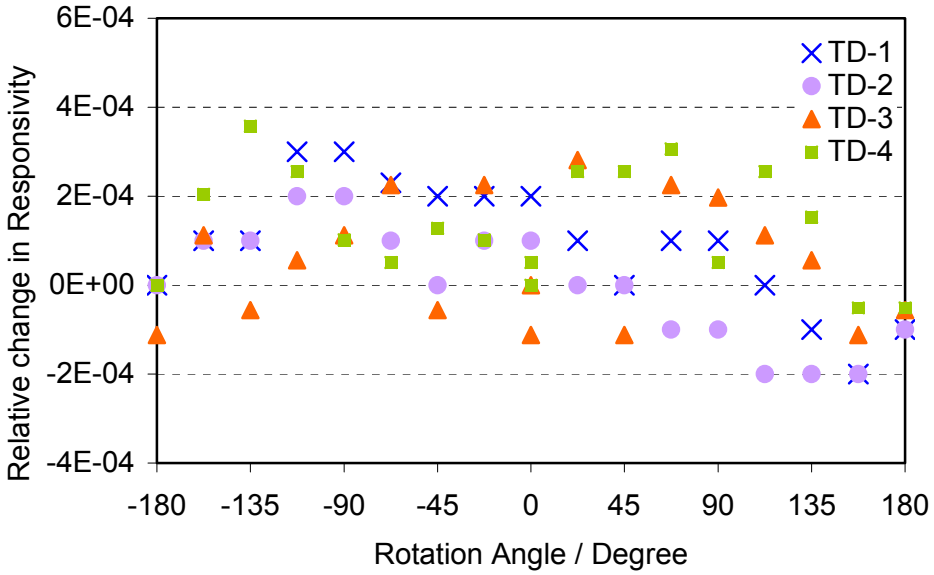

Figure 3.3 : Relative change in responsitivity of trap detectors as a function of the rotation angle about beam axis.

3.2.3 Non-Linearity

A detector is said to be linear if its output signal is directly proportional to the incident power. Detectors are often linear within certain power level limits, which are often termed as their dynamic range. Noise will determine the lowest level of incident light that is detectable. The upper limit of the linearity is determined by the maximum current that the detector can handle without becoming saturated. Saturation is a condition in which there is no further increase in detector response as the input light is increased [64]. Linearity may be quantified in terms of the maximum percentage deviation from a straight line over a range of input light levels, which is called non-linearity. The non- linearity of trap detectors was measured using the flux-addition technique. Intensity stabilized He-Ne laser with a stability of 0.006% was used as the light source. Laser beam was split into two beams A and B, of about the same powers as shown in figure 3.4. Blocking one each time and superimposing them on the detector, photo-currents I_A, I_B and I_{AB} were measured.

Using recorded data the non- linearity N is calculated from the following relation [33,34,65].

$$N(I_{AB}) = \frac{(I_{AB} - I_A - I_B)}{I_{AB}} \tag{3.2}$$

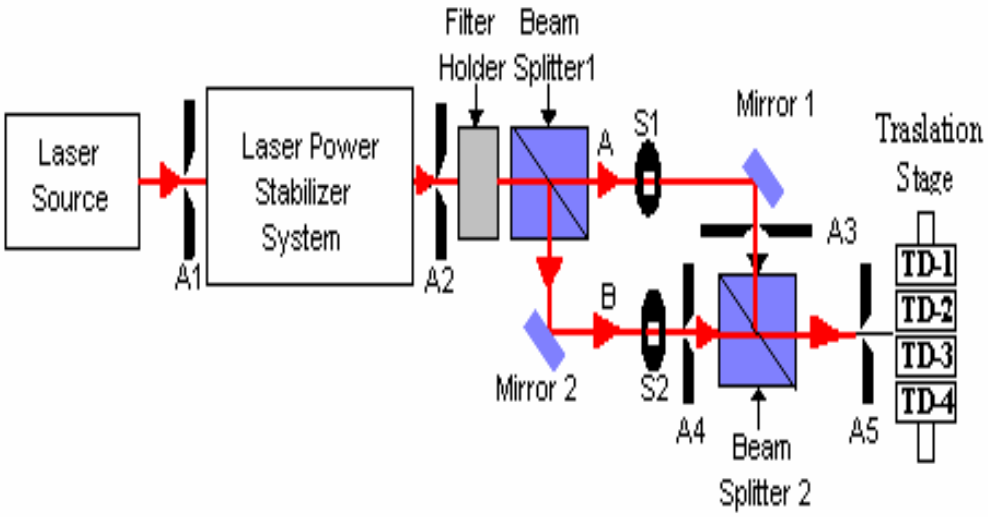

Figure 3.4: Non-linearity measurement set up. A1, A2, A3, A4 and A5 are apertures, S1 and S2 are shutters.

Four silicon based trap detectors were used for the measurements. Figure 3.5 represent the non-linearity each trap detectors. Measurements were done at 632.8 nm He-Ne laser and a series of neutral density filters were used to attenuate the flux incident on the detector. At about 0.80 mW power level non-linearity varies between $1x10^{-5}$ and $2x10^{-5}$ and above 0.80 mW non-linearity increases. Therefore the responsitivity of trap detectors is linear to within few parts in 10^{-5}. There are many factors that affect the non-linearity of silicon photodiodes, therefore trap detectors. Most important factors are: series resistance of photodiodes, the diameter of the incident beam, photocurent and size of the active area of photodiode[66-68].

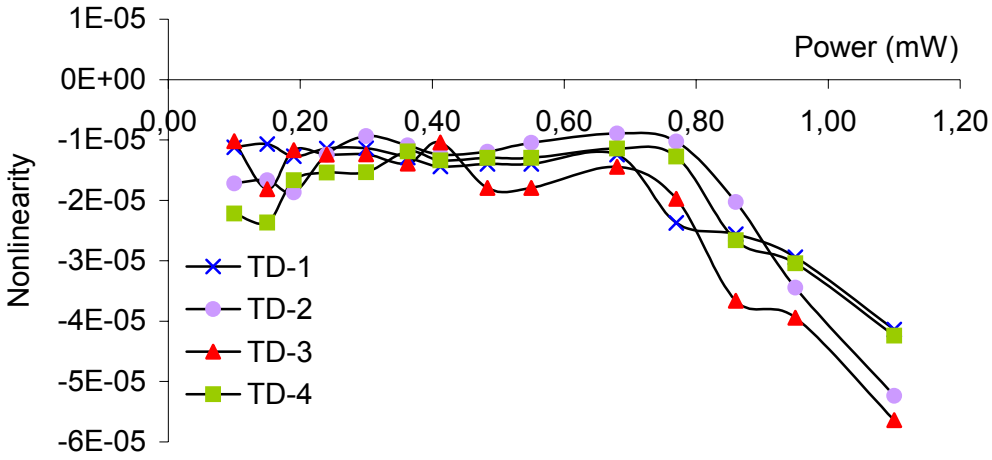

Figure 3.5: Non-linearity measurement of silicon based trap detectors TD-1, TD-2, TD- 3 and TD-4.

3.2.4 Spatial Non-uniformity

This is the variation of responsivity as a function of position across the detecting surface. A spatially uniform detector would have no changes in responsivity across the detecting surface. The spatial uniformity of silicon photodiode and trap detector were sperately investigated by scanning the surface of silicon photodiode and entrance aperture of trap detector with an intensity stabilised He-Ne laser (632.8 nm) beam of 1.1 mm diameter at 0.5 mm intervals in two perpendicular axes using the set up given in figure 3.6. The uniformity of these detectors was obtained by dividing their responses at the selected point to the maximum responsivity value. Within the 4mm diameter as shown in figures 3.7 and 3.8 the change in the spatial uniformity of single silicon and trap detectors were obtained as about 0.003%.

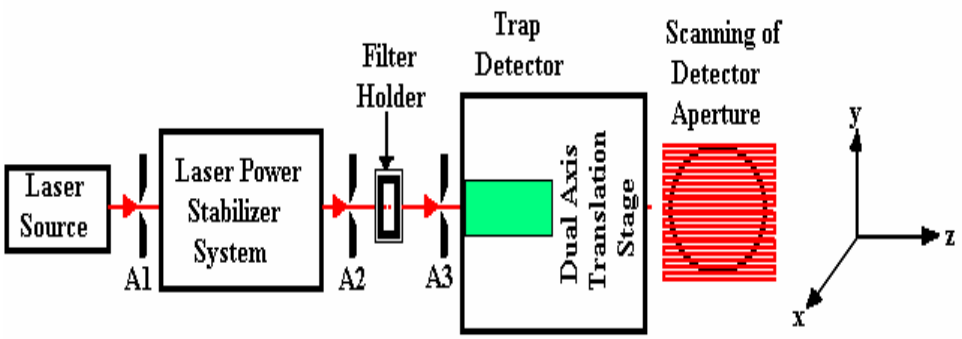

Figure 3.6: Spatial uniformity measurement set up.

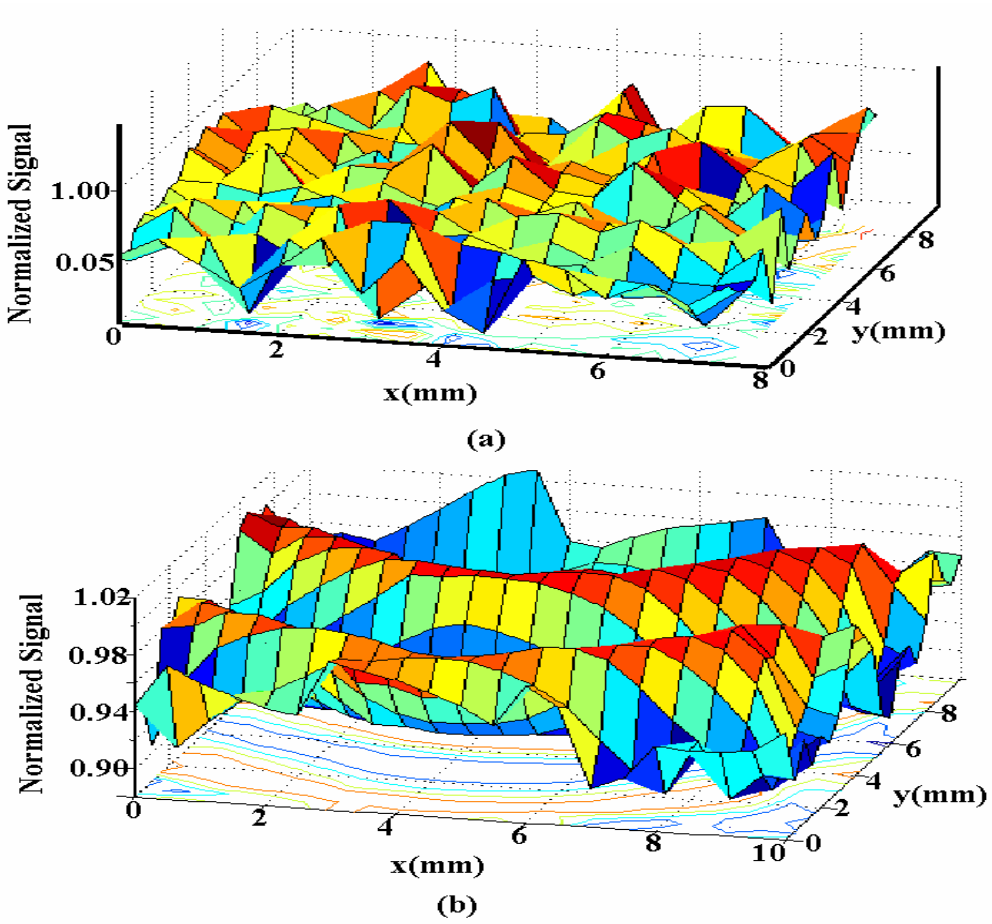

Figure 3.7: Relative spectral responsitivity maps of trap detector and silicon photodiode in two-dimensional view.

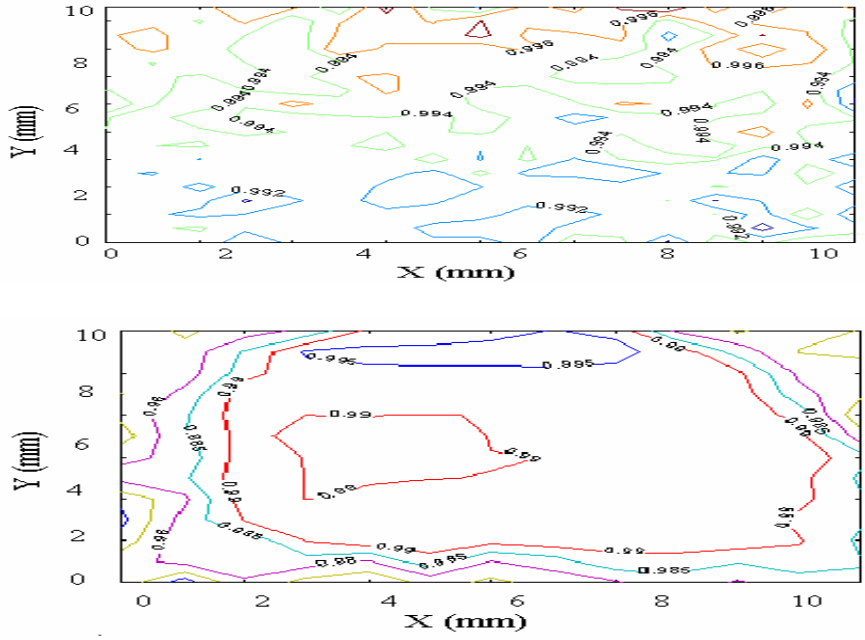

Figure 3.8: Relative spectral responsivity maps of silicon photodiode and trap detector in one dimensional view.

3.2.5 Temporal Stability

This refers to the lack of change of the responsivity with time. The spectral responsivity of trap detectors were measured four times in a year at four laser wavelengths and found to be constant to 0,02% as shown in figure 3.9.

The spectral responsivity of all types of silicon photodiodes has been shown to be sensitive to changes in humidity [69-70]. This has been correlated by Köhler and shown to be due to changes in the specular reflectance of the photodiodes [70]. However trap detectors are only sensitive to changes in the reflectance of individual photodiodes to the fifth power. This means that trap detectors are extremely insensitive to changes in humidity. It is possible some loss of spectral responsivity may occur if dust particles reside on the individual silicon photodiodes increasing the diffuse reflectance. However, careful handling of the trap detectors should prevent this being a significant effect.

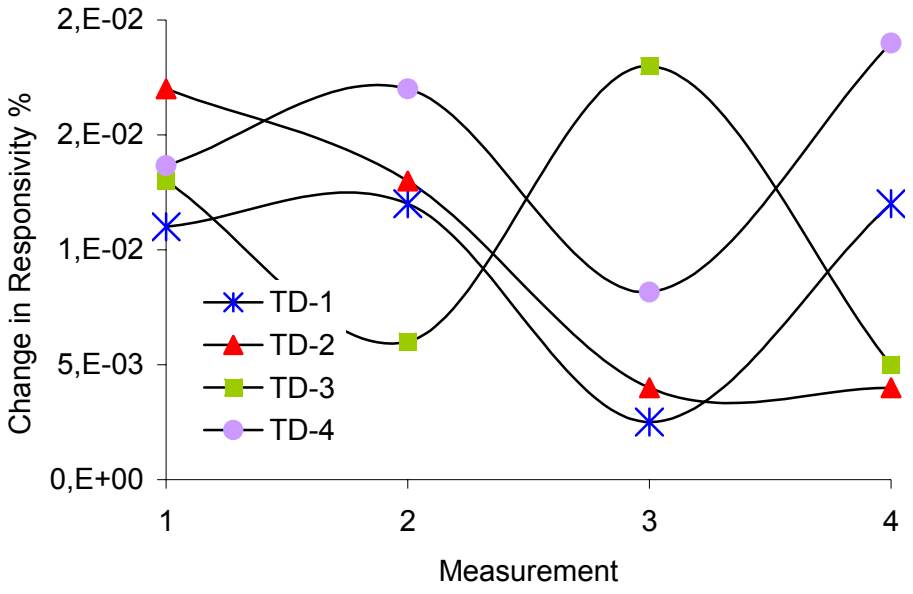

Figure 3.9: Response stability of trap detectors at 632.8 nm He-Ne laser wavelength.

3.2.6 Reflectance Losses

The basic idea behind the trap detector construction is to reduce the high reflectance looses of a detector consisting of a single photodiode. The incident photon in a trap detector undergoes five reflections and the residual beam is reflected along the incident beam. The absolute reflectance of this residual beam in trap detector was measured using Ar-Ion laser at 457.1nm, 488 nm and 514.5 nm wavelengths, Nd:YAG at 532 nm and He-Ne laser at 632.8 nm wavelength using the set up given in figure 3.10.

A stabilized laser beam was aligned to incident a point close to the rim of a mirror. The reflected beam from the mirror falls on the trap detector. Any reflected beam from this trap detector was measured using another trap detector. The measurements were repeated by interchanging the detectors. The repeatability in these measurements was of the order of 10^{-4}.

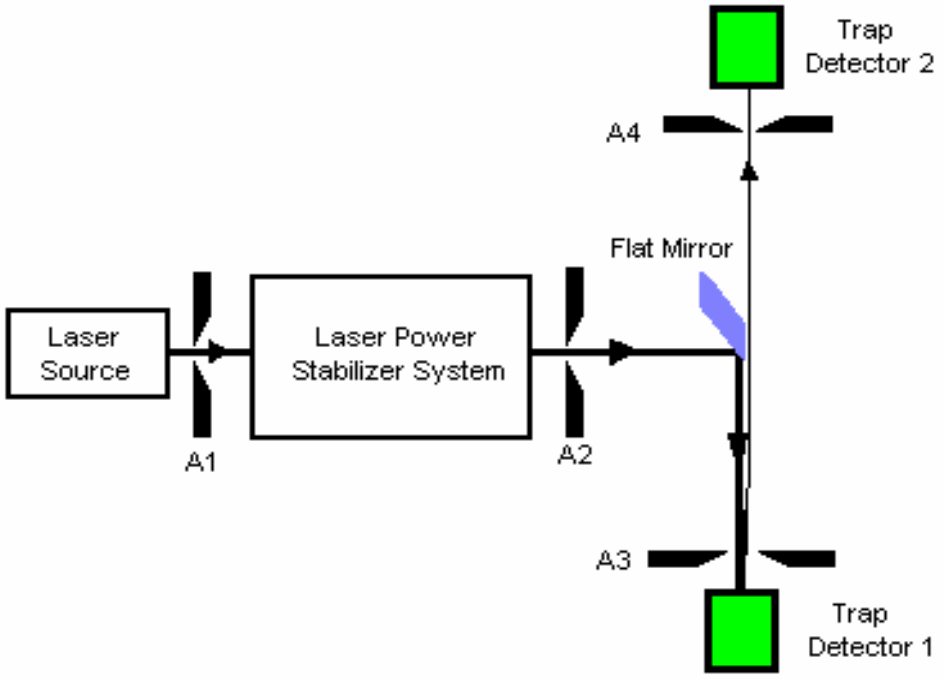

Figure 3.10: Set up for the absolute reflectance measurements of trap detectors.

Relative spectral reflectance's of trap detectors from 350 nm to 850 nm were measured using Tungsten halogen lamp, double monochromator and light aligning components as shown in figure 3.11. The collimated beam reflected from the edge of flat mirror and incident on the reference and trap detector respectively. The direct signal is measured from these detectors; the reflected beam from these detectors is focused onto the photomultiplier tube to be measured. The measurement results are displayed in the figure 3.12.

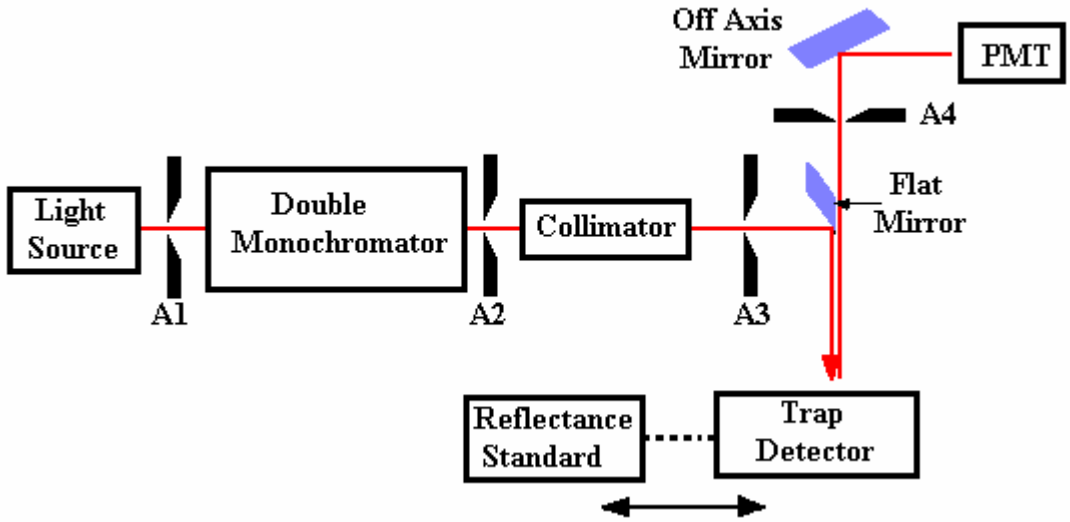

Figure 3.11: Set up for the relative reflectance measurements of trap detectors. A1, A2, A3 and A4 are apertures, PMT is photo multiplier tube.

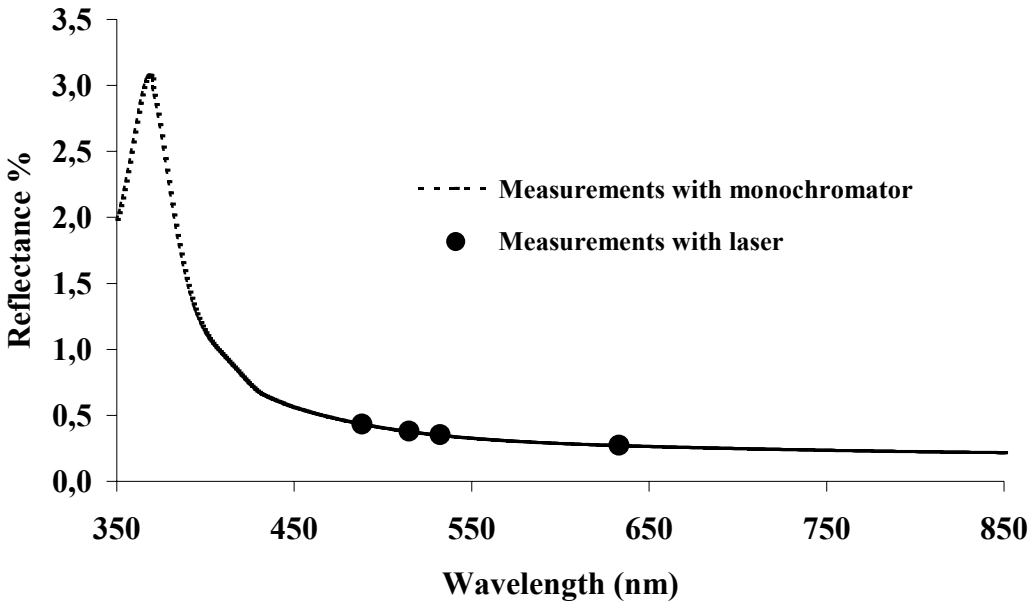

Figure 3.12: Illustration of reflectance of trap detectors

3.2.7 Quantum efficiency

Quantum efficiency is defined as the ratio of countable events produced by photons incident on the detector to the number of photons. Quantum efficiency may be defined as internal quantum efficiency (IQE) and external quantum efficiency (EQE). The IQE is the number of electron hole pairs is created per absorbed photons; the EQE is the number of number of electron hole pairs created per incident photons. [71] The quantum efficiency is basically another way of expressing the effectiveness of the incident radiant energy for producing electrical current in a circuit.

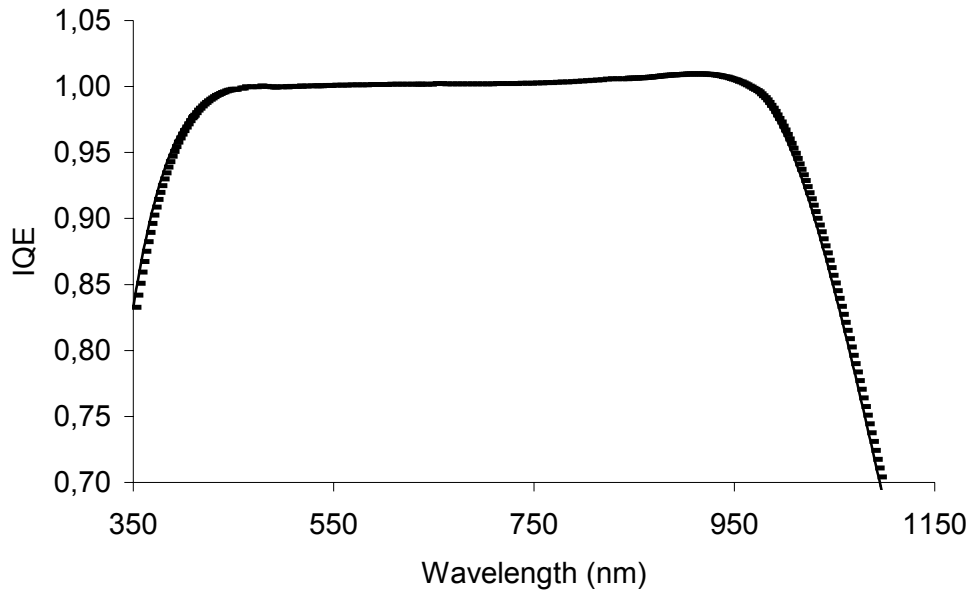

Figure 3.13: Internal quantum efficiency of trap detector.

The most important advantage of silicon photodiode trap detectors is that IQE is close to unity [9,25,26,28]. This means the spectral responsivity of trap detector would not be changed in time and it would be linear over many orders of irradiance.

Any deflections from unity are called internal quantum deficiency, which is due to the trap charges at the Si and SiO_2 interface [26]. This charge attracts the electrons (the minority carrier in this region) and reduces the number reaching the depletion region. To calculate the quantum efficiency of the photodiode it is necessary to quantify this loss mechanism. Typical IQE of silicon photodiode is shown in figure 3.13. As shown from figure 3.13 there is reduction from unity, which come from following reasons. Incident photon on a silicon photodiode create electron or hole pairs and they are measured when they reach the depletion region where the high field separates them, figure 3.14. Any photon absorbed within the depletion region will result in the measurement of an electron in the external circuit, i.e unity external quantum efficiency. Mid-visible photons are likely to be absorbed in this region. Photons redder than these are likely to be absorbed beyond this region and those bluer before it.

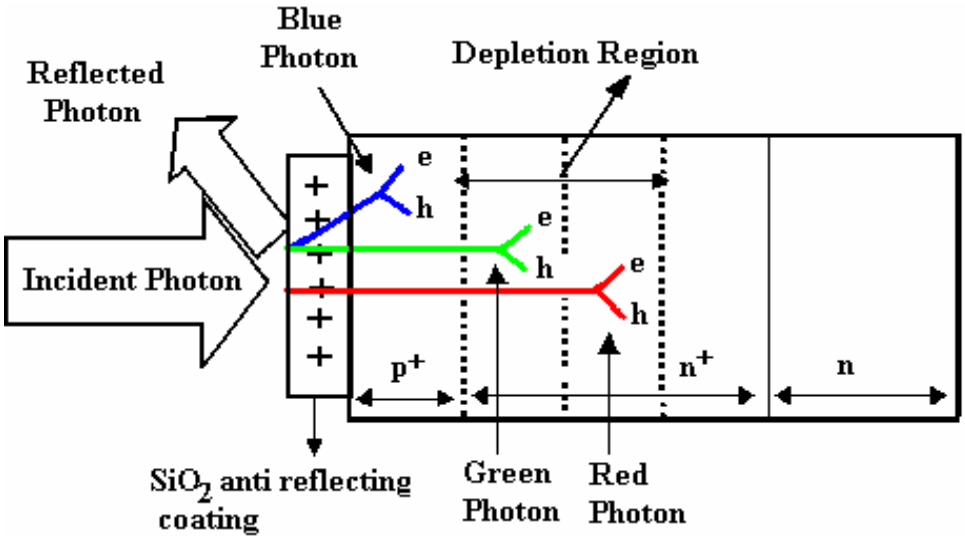

Figure 3.14: Diagrammatic representation of interaction of light with a silicon photodiode as a function of wavelength.

When red photons are absorbed they generate an electron hole pair but not in the depletion region. Before diffusing to this region some of these carriers will recombine. These will not be measured and so the quantum efficiency will be reduced. Blue photons are also not absorbed in the depletion region and must diffuse to it for collection.

3.2.8 Responsitivity

Responsitivity is defined as the detector output per unit of input power. The units of responsitivity are either amperes/watt (alternatively milliamperes/milliwatt or microamperes/microwatt, which are numerically the same) or volts/watt, depending on whether the output is an electric current or a voltage. Knowledge of the responsivity allows one to determine how much detector signal will be available for a specific application. The responsivity R(λ) of trap detector is given by [72],

$$R = [1 - \rho(\lambda)][1 - \delta(\lambda)]\frac{e\lambda}{nhc} \tag{3.3}$$

where e is the elementary charge, λ is the wavelength in vacuum, h is the Planck constant, c is the speed of light in vacuum, n is the refractive index of medium, ρ(λ) is the reflectance of trap detector and δ(λ) is the internal quantum deficiency of trap detector, and 1- δ(λ) is the internal quantum efficiency.

The absolute responsivities of trap detectors at laser wavelengths were measured by calibrating them against ESCR and the results are displayed in figure 3.15.

So far the characterization of trap detectors that used to link the high accuracy optical powers obtained from ESCR to the other system were studied. It was found that the trap detectors made from silicon photodiodes, in the visible region have low reflectance (~1%), high IQE (~100%), good spatial uniformity (~3×10^{-5}) and non-linearity (~10^{-5}).

Since the absolute optical power can be measured at discrete laser wavelengths the responsivity of trap detectors can only be measured at discrete wavelengths. This is

limited value for the users requiring the broader spectral coverage. To meet these needs the responsivity values of trap detector were obtained with interpolating and extrapolating the measured values.

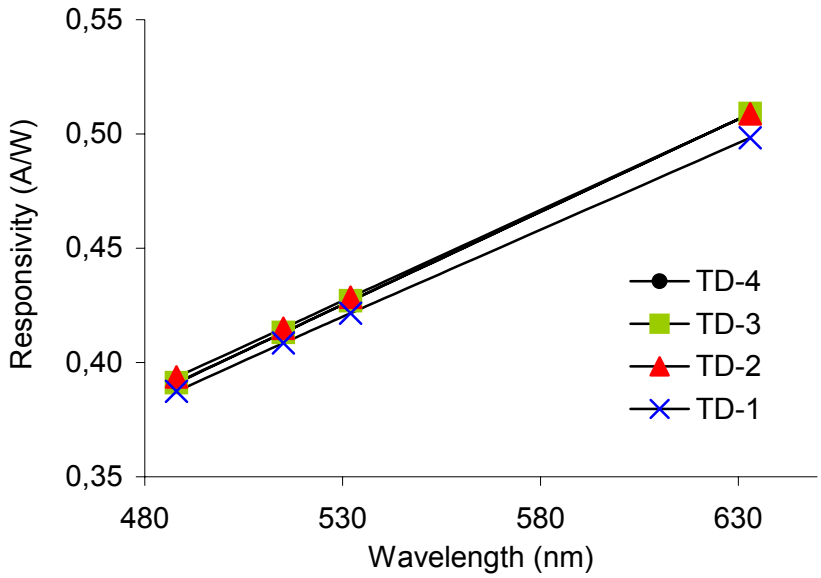

Figure 3.15: Absolute responsivity measurements at 488 nm, 514.5 nm, 532 nm and 632.8 nm wavelengths using ESCR.

3.3 Interpolation and Extrapolation of Responsivity

Since the spectral responsivity of silicon photodiode in equation 3.3 is determined by the reflectance of the diode surface and the quantum efficiency, finding suitable theoretical models that best fit the measured values for reflectance and quantum efficiency the responsivity of trap detector can be obtained.

3.3.1 Calculation of the Reflectance of Trap Detector

A photodiode can be described as a Si substrate with a thin layer of SiO_2 on the surface as shown in figure 3.16. The reflectance of the photodiode can be calculated from the thickness of the SiO_2 layer and the known refractive indices n_2 for SiO_2 and n_3 for Si. In the visible region, the refractive index of the SiO_2 is practically real (n); however, for Si the complex refractive index has real and imaginary parts (n, k) [72].

The transmission of UV, visible and infrared radiation through the media and the behaviour of such radiation at all interface between different media are aspects of the general behaviour of electromagnetic waves which are governed by Maxwell's field equations. These equations may be written as [73]

$$\begin{aligned} &\vec{\Delta}.\vec{D} = 4\pi\rho \\ &\vec{\Delta}.\vec{B} = 0 \\ &\vec{\Delta}\,x\,\vec{E} + \frac{1}{c}\frac{\partial \vec{B}}{\partial t} = 0 \\ &\vec{\Delta}\,x\,\vec{H} = \frac{4\pi}{c}\vec{j} + \frac{1}{c}\frac{\partial \vec{D}}{\partial t} \end{aligned} \qquad (3.4)$$

In these equations, E and H are electric and magnetic field vectors respectively. These two field vectors are often used to describe an electromagnetic field. The quantities D and B are called the electric displacement and magnetic induction respectively. These two quantities are introduced to include the effect of the field on matter. The quantities ρ and j are electric charge density and current density respectively, and may be considered as the source of the fields E and H. These four Maxwell's equations completely determine the electromagnetic fields and are the fundamental equations of the theory of such fields.

Consider a ray coming from the air (refractive index n_1) to the surface of the photodiode at an angle of θ_1 with respect to the normal of surface as shown in figure 3.16. Part of the beam is reflected from the surface of SiO_2. The transmitted beam is

again partly reflected from the interface between SiO_2 and Si and remaining beam is transmitted.

The amplitudes of reflected and refracted waves in terms of incident wave can be obtained using the Maxwell's equations for homogeneous, isotropic and source free media (ρ =0, j=0) and equations 3.4. In order to obtain the electric and magnetic fields in different media the kinematical and dynamical properties of the fields at the interfaces should be considered. Kinematical properties describe the equivalence of incident θ_1 and reflected θ_2 angles and Snell's law. Dynamical properties describe the intensities of reflected and refracted waves in terms of incident wave and phase change and polarization.

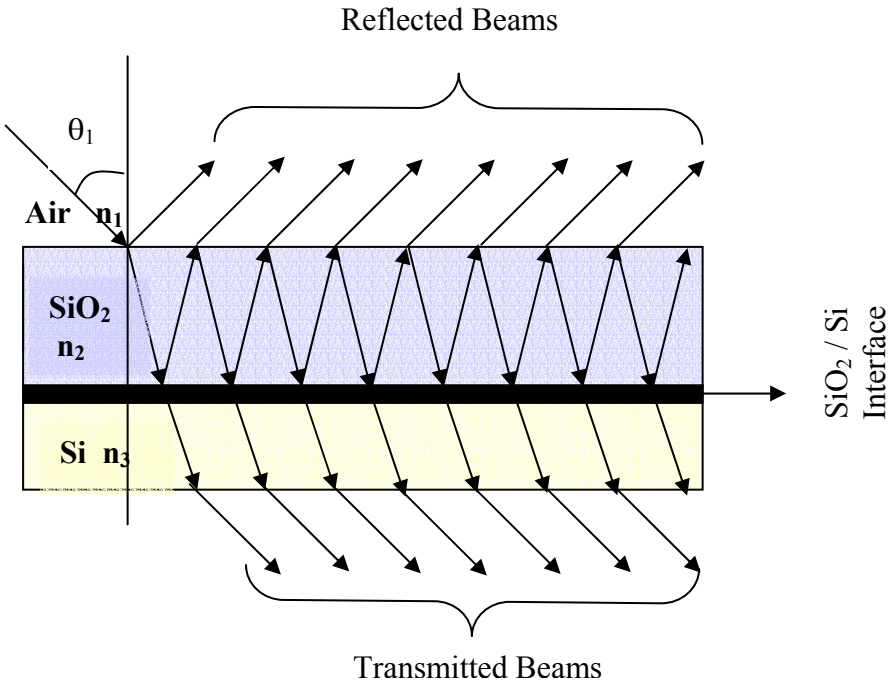

Figure 3.16: Photodiode structure with behaviour of fields at the interface between silicon and silicon dioxide.

Kinematical properties of electric and magnetic fields at the interface require that both the spatial and time variations should be same [73]. Dynamical properties of electric and magnetic fields at z=0 requires the continuity of fields at z=0. That is

$$
\begin{aligned}
&(\varepsilon \vec{E}_1 + \varepsilon \vec{E}_2 - \varepsilon' \vec{E}_3).\hat{n} = 0 \\
&(\vec{k}\, x\, \vec{E}_1 + \vec{k}\, x\, \vec{E}_2 - \vec{k}'\, x\, \vec{E}_3).\hat{n} = 0 \\
&(\vec{E}_1 + \vec{E}_2 - \vec{E}_3) x \hat{n} = 0 \\
&(\frac{1}{\mu}\vec{k}\, x\, \vec{E}_1 + \frac{1}{\mu}\vec{k}\, x\, \vec{E}_2 - \frac{1}{\mu'}\vec{k}'\, x\, \vec{E}_3) x \hat{n} = 0
\end{aligned}
\tag{3.5}
$$

The first two equations describe the continuity of normal components of electric displacement and magnetic induction. The last two equations describe the continuity of tangential components of electric and magnetic fields.

The amplitudes of reflected and refracted waves from medium m to n (m,n=1,2,3) in the interface of two media can be obtained using the continuity equations 3.5.

In applying these boundary conditions it is convenient to consider two separate situations, one in which the incident plane is linearly polarized with its polarization vector perpendicular to the plane of incidence (the plane defined by k and n), and the other in which the polarization vector is parallel to the plane of incidence.

First consider the electric field perpendicular to the plane of incidence, as shown in figure 3.17 a. All the electric fields are shown directed away from the viewer. The orientations of the magnetic field vectors are chosen to give a positive flow of energy in the direction of the wave vectors. Since the electric fields are all parallel to the surface, the first boundary condition in equations 3.5 yields nothing. The third and fourth equations in 3.5 give

$$
\begin{aligned}
&E_{01} + E_{02} - E_{03} = 0 \\
&\sqrt{\frac{\varepsilon}{\mu}}(E_{01} - E_{02})\cos\theta_i - \sqrt{\frac{\varepsilon_3}{\mu_3}} E_{03}\cos\theta r = 0
\end{aligned}
\tag{3.6}
$$

while the second, using Snell's law, duplicates the third, The relative amplitudes of the reflected and refracted waves can be found from equations 3.6 are given as [74]

$$r_{mn} = \frac{n_m \cos\theta_m - n_n \cos\theta_n}{nm\cos\theta_m + n_n \cos\theta_n} \tag{3.7}$$

$$t_{mn} = \frac{2n_m \cos\theta_m}{n_m \cos\theta_m + n_n \cos\theta_n} \tag{3.8}$$

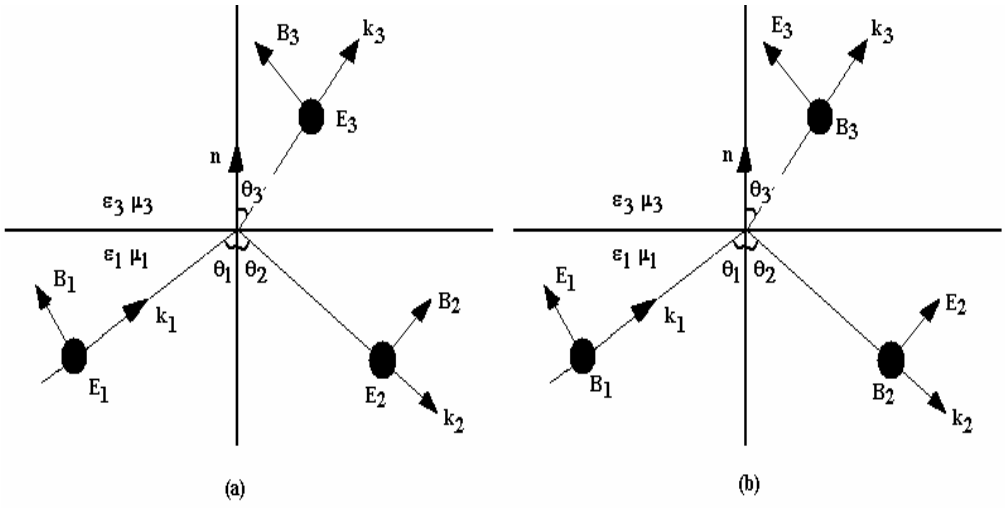

Figure 3.17: Reflection and refraction with the polarization, a) perpendicular to the plane of incidence, b) parallel to the plane of incidence.

If the electric field is parallel to the plane of incidence, as shown in the figure 3.17 b the boundary conditions involved are normal D, tangential E and; the first, third and fourth equations in 3.5. The tangential E and H continuous demand that

$$\cos\theta_i\left(E_{01}-E_{02}\right)-\cos\theta_r E_{03}=0$$
$$\sqrt{\frac{\varepsilon}{\mu}}\left(E_{01}+E_{02}\right)-\sqrt{\frac{\varepsilon_3}{\mu_3}}E_{03}=0 \tag{3.9}$$

The relative amplitudes of reflected and refracted fields are therefore for parallel-polarized light[74]

$$r_{mn}=\frac{n_n\cos\theta_m-n_m\cos\theta_n}{n_n\cos\theta_m+n_m\cos\theta_n} \tag{3.10}$$

$$t_{mn}=\frac{2n_m\cos\theta_m}{n_n\cos\theta_m+n_m\cos\theta_n} \tag{3.11}$$

At the interface between Si and SiO_2 the reflectance and transmittance coefficients are complex The refracted angles θ_2 and θ_3 in SiO_2 and Si respectively can be calculated using Snell's law as

$$\theta_2=\arcsin\left(\frac{n_1\sin\theta_1}{n_2}\right) \tag{3.12}$$

$$\overline{\theta}_3=\arcsin\left(\frac{n_1\sin\theta_1}{\overline{n}_3}\right) \tag{3.13}$$

The partial reflections results in an infinite series of inter reflections between the surfaces of SiO_2 layer. The phase difference between two subsequent wave fronts existing in the front surface of SiO_2 layer is

$$\beta=\frac{2\pi}{\lambda_1}n_2 t\cos\theta \tag{3.14}$$

where λ_1 is the wavelength in the air and t is the thickness of the layer.

The reflection coefficient amplitude for Si photodiode can be obtained as follows. Consider a ray incident from air (refractive index n_1) upon a parallel plate of transparent silicon dioxide of thickness and refractive index n_2. The situation is illustrated in figure 3.16.

The incident light partially reflected and transmitted at the first interface. A portion of light again reflected back and remaining one transmitted as shown in figure 3.18. The total reflectance r of the plate for rays incident at the angle θ will be the sum of all the radiance emerging to the top as in the figure 3.18. For a plate of infinite extent, there will be an infinite number of inter reflections and overall reflectance will be as given in 3.18.

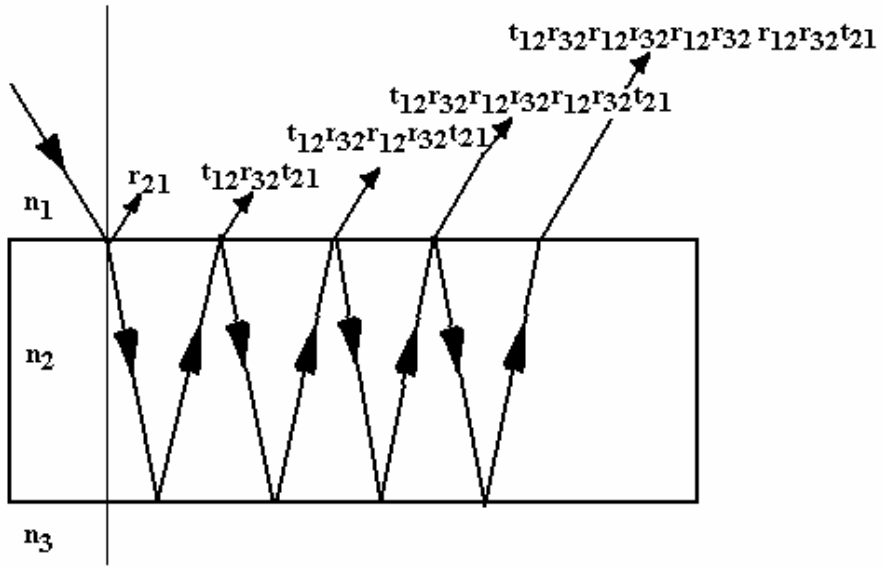

Figure 3.18: Illustration of multiple reflections between two interfaces.

$$
\begin{aligned}
r &= r_{21} + t_{12}r_{32}t_{21} + t_{12}r_{32}r_{12}r_{32}t_{21} + t_{12}r_{32}r_{12}r_{32}r_{12}r_{32}t_{21} + t_{12}r_{32}r_{12}r_{32}r_{12}r_{32}r_{12}r_{32}t_{21} + \ldots\ldots \\
&= r_{21} + t_{12}r_{32}t_{21} + t_{12}r_{32}^2r_{12}t_{21} + t_{12}r_{32}^3r_{12}^2t_{21} + t_{12}r_{32}^4r_{12}^3t_{21} + \ldots\ldots \\
&= r_{21} + t_{12}r_{32}t_{21}(1 + r_{32}r_{12} + r_{32}^2r_{12}^2 + r_{32}^3r_{12}^3 + r_{32}^4r_{12}^4 + \ldots\ldots)
\end{aligned}
\qquad (3.15)
$$

Using the following identity in these geometrical series

$$\sum_{i=0}^{\infty}\left(x^{i}\right)^{2}=\frac{1}{1-x^{2}},|x|\langle 1 \tag{3.16}$$

the amplitude reflection coefficient for the photodiode obtained as

$$\bar{r}=r_{12}+\frac{t_{12}t_{21}\bar{r}_{23}\exp(-2i\beta)}{1+r_{12}\bar{r}_{23}\exp(-2i\beta)} \tag{3.17}$$

The intensity reflection coefficient can be calculated from the amplitude of reflection coefficient as

$$\rho_{S,P}(\theta_1)=\left|\bar{r}\right|^{2} \tag{3.18}$$

Because of the geometry of device, the angle of incidence of these reflections is twice 45° for the s plane of polarization, once normal incidence, and twice 45° for the p plane of polarization. Thus the reflectance of trap detector is [74]

$$\rho ref=\rho(0°).\rho^{2}{}_{S}(45°).\rho^{2}{}_{P}(45°) \tag{3.19}$$

By using equations 3.7-3.8, 3.10-3.11, 3.17- 3.19 the spectral reflectance's of silicon photodiodes and trap detector were calculated over a wavelength range extending from 250 to 850 nm for polarized beams either in the plane perpendicular to the plane of incidence -s plane or in the plane parallel to the plane of incidence -p plane. Calculations were done for two angles of incidence: 45° and an angle close to 0°. The choice of these two angles was determined by the geometry of the trap detector.The calculated reflectance values s are presented in figures 3.19-3.22. In VIS and NIR regions the calculated reflectance's of a silicon photodiode are below 30 % and 45 % for the beams in the plane parallel and perpendicular to the plane of incidence respectively. For the normal incidence of beam it is at the order of %. In

the UV region the reflectance become higher therefore corrections need to applied become larger. On the other hand the reflectance of trap detector include two reflected beams from the plane perpendicular to the plane of incidence two parallel beams reflected from the plane parallel to the plane of incidence and one reflected beam from the plane normal to the plane of incidence. Hence reflectance in the VIS region decreased below 0.5 % which increase the external quantum efficiency about sixty times compare to single photodiode.

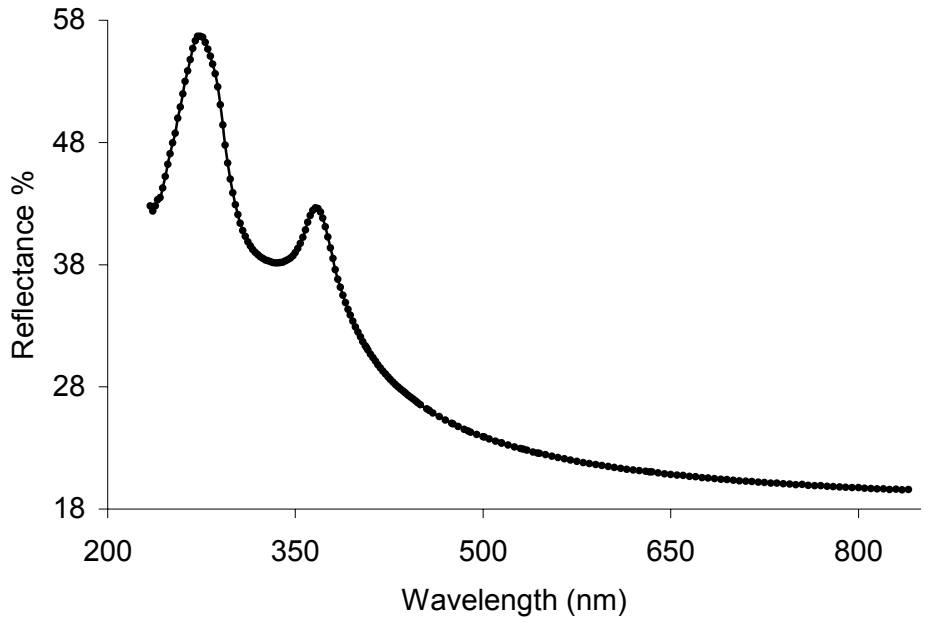

Figure 3.19: Calculation of reflectance of p polarized light at 45^0.

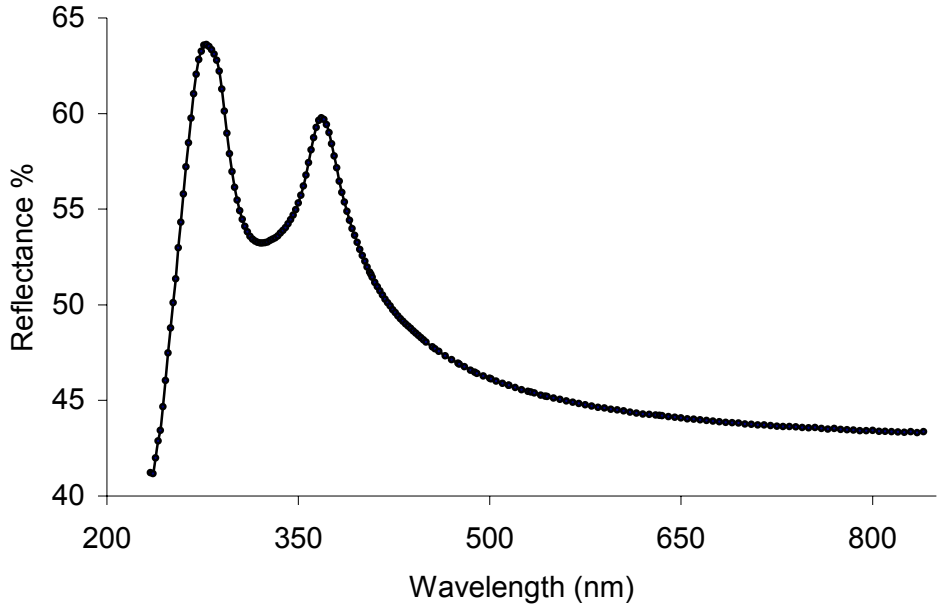

Figure 3.20: Calculation of reflectance of s polarized light at 45^0.

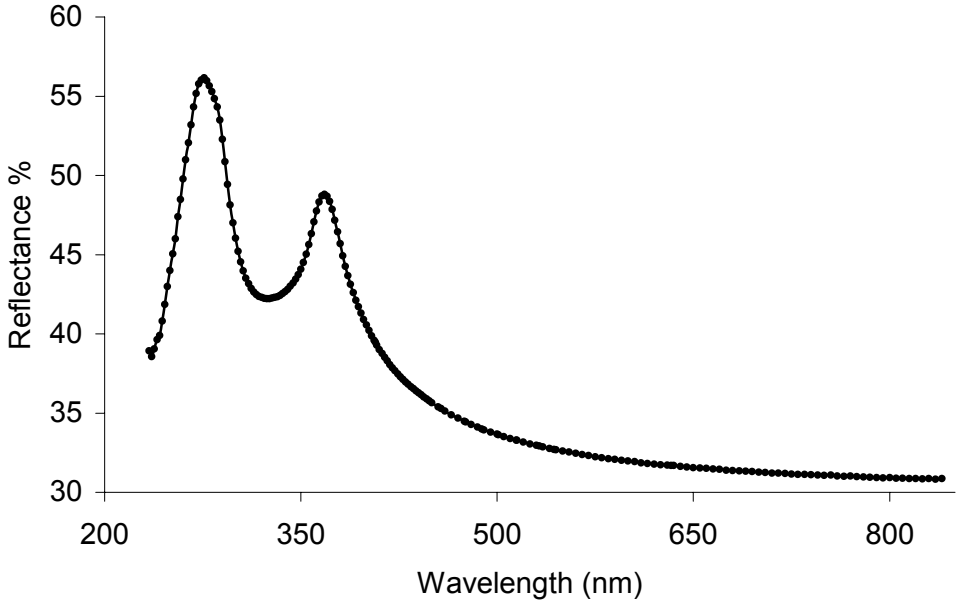

Figure 3.21: Calculation of reflectance of s polarized light at 0^0.

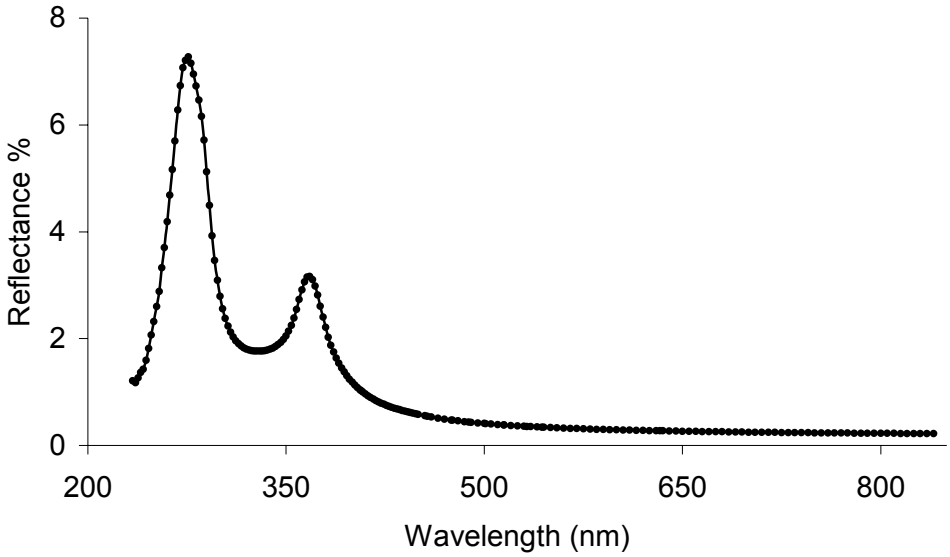

Figure 3.22: Calculation of reflectance of trap detector.

3.3.2 Calculation of the Quantum Efficiency of Silicon Photodiode

Silicon photodiodes have IQE close to unity. That is for every photon incident on the photodiode one electron hole pairs are created. However doe to some loss mechanisms all the created electron hole pairs wouldn't contribute to the current measured in the external circuit. Therefore EQE would be a few tenths of a percent below unity in the mid visible region of the spectrum and decreases further elsewhere. Therefore in the mid visible region quantum efficiency can me modelled as a function of wavelength based on physics of photodiodes.

3.3.3 Models Used for the IQE Calculations of Silicon Photodiodes

- The first models used for the IQE calculations is developed by Geist et al [75] which is one parameter model describes the wavelength dependence of IQE as

$$IQE = 1 - \delta = K[A_1 \exp(-\lambda / \lambda_1) + A_2 \exp(-\lambda^2 / \lambda_2^2)] \qquad (3.20)$$

where K, A_1, A_2, λ_1 and λ_2 are free parameters needs to be determined so as to fit this equation to the measured IQE values shown in figure 3.23. This is a mathematical model, does not based on physics of photodiodes.

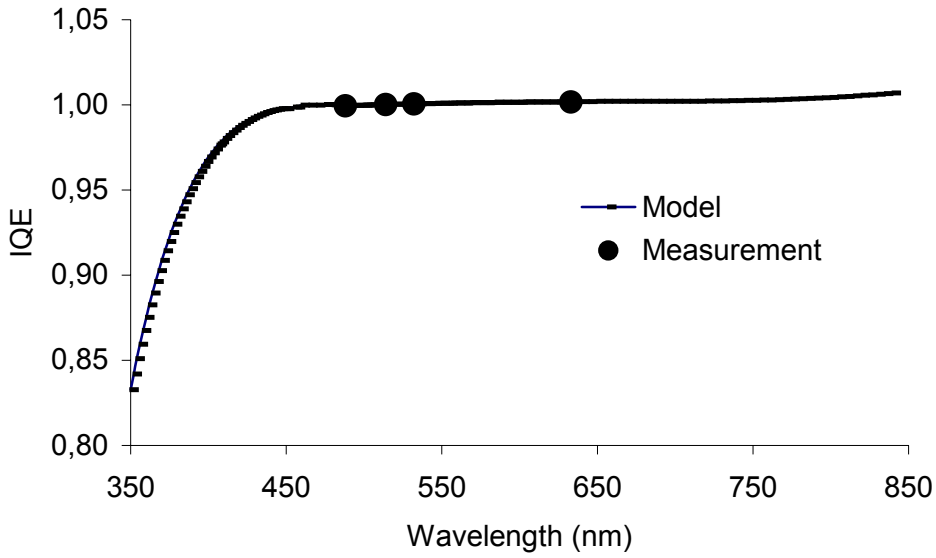

Figure 3.23: Measured and modeled (first model) IQE of trap detector.

- Second model used for the IQE is again developed by Geist [76]. This model approximates the effects of recombination loss at the Si/SiO_2 interface by collection efficiency that increases linearly from value of P at the interface to a value of unity at the depth T into the photodiode. The value T is expected to be roughly equal to the distance from the interface to the front of the depletion region. The losses at the near infrared wavelengths are modeled by a term that approximates the internal quantum efficiency distribution in the uniformly doped bulk region behind the depletion region. The complete model equation for the IQE of the photodiode is given by

$$IQE(\lambda) = P + \frac{1-P}{\alpha(\lambda)T}[1 - \exp[-\alpha(\lambda)T]] - \frac{h}{\alpha(\lambda)L^2}\exp[-\alpha(\lambda)H] \qquad (3.21)$$

where $\alpha(\lambda)$ is the absorption coefficient of silicon at wavelength λ, H is the sum of the widths of the front layer and depletion regions, h is the width of the bulk region, L is the minority carrier diffusion length in the bulk region. Wavelength dependency of absorption coefficient as shown in figure 3.24 calculated from [36], and the IQE for this model is obtained as shown in figure 3.25.

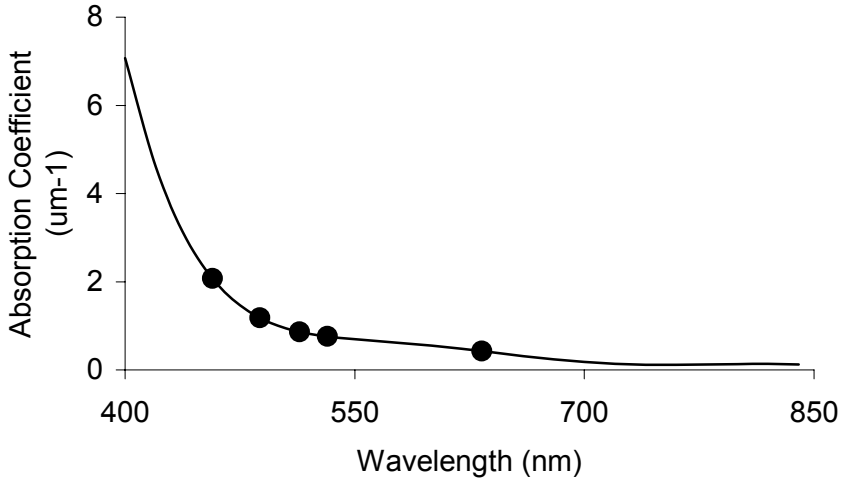

Figure 3.24: Absorption coefficient of silicon photodiode.

Although this model works quite well in the visible region, it does not ideally reproduce data in the near infrared region. So a new model that give a slight decrease in the IQE at near infrared wavelengths with the same functional form was developed.

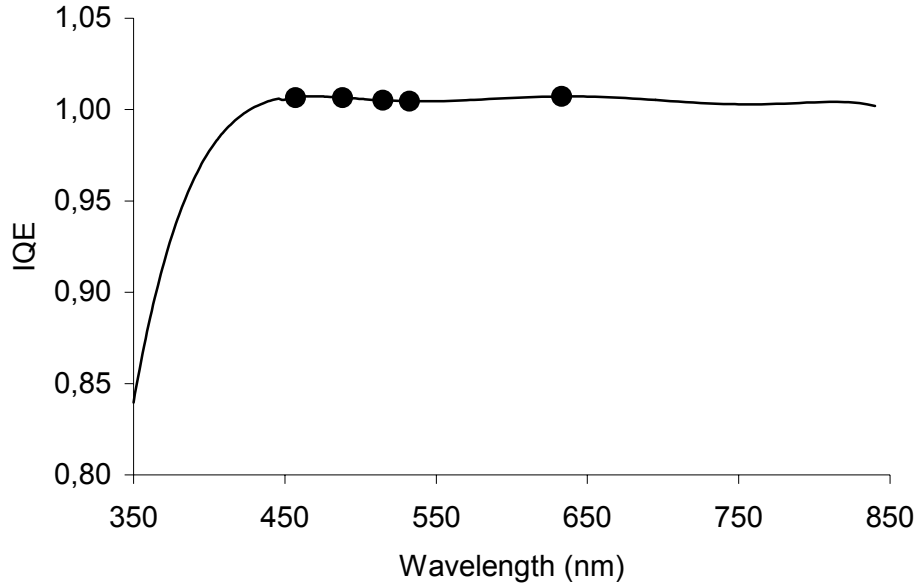

Figure 3.25: Measured and modeled (second model) IQE of trap detector.

- This model is the same as previous one except a term added to it to represent a loss caused by light exiting (or being absorbed) at the back and of the photodiode and can be dropped if nearly all of the light is absorbed before reaching the back end [36]. This model is given as

$$IQE = P_f + \frac{1-P_f}{\alpha(\lambda)T}\{1-\exp[-\alpha(\lambda)T]\} - \frac{1-P_b}{\alpha(\lambda)(D-T)} \{\exp[-\alpha(\lambda)T] - \exp[-\alpha(\lambda)D]\} - P_b \exp[-\alpha(\lambda)h] \quad (3.22)$$

where P_f is the quantum efficiency at the SiO_2/Si interface. This model assumes that the quantum efficiency increases starting from SiO_2/Si interface and reaches its maximum value at the p-n junction of the diode at depth T, then it linearly decreases until P_b, the bulk value of silicon, is reached at depth D.

- Another model used to calculate EQE is based on numerical modeling of photodiodes. This model does not provide equation with adjustable fitting parameters but formulas are normalized two data points for EQE one at the blue end of the

spectrum one at the near infrared end. This model is derived from physics of photodiode as follows.

In a photodiode the number of electron hole pairs contribute to the current is given by [77]

$$EQE = \frac{j_h + j_e}{AF_0} \tag{3.23}$$

where j_h and j_e are electron and hole current densities respectively, A is the surface area incident photon flux. The electron and hole current densities can be obtained by solving the transport and continuity equations for the photodiode [78]. Solutions of transport and continuity equations give the quantum efficiencies for electron and holes as follows [79-80]

$$EQE_n(\lambda) = \frac{\alpha L_n}{\alpha^2 L_n^2 - 1}\left[\frac{\frac{S_f L_n}{D_n} + \alpha L_n - \left(\frac{S_f L_n}{D_n}\cosh(\frac{w}{L_n}) + \sinh(\frac{w}{L_n})\right)e^{-\alpha x}}{\frac{S_f L_n}{D_n}\cosh(\frac{w}{L_n}) + \sinh(\frac{w}{L_n})} - \alpha L_n e^{-\alpha w}\right] \tag{3.24}$$

$$EQE_p(\lambda) = \frac{\alpha L_p}{\alpha^2 L_p^2 - 1}\left[\alpha L_p - \frac{\frac{S_b L_p}{D_p}\cosh(\frac{l}{L_p}) + \sinh(\frac{l}{L_p}) - (\frac{S_b L_p}{D_p} - \alpha L_p)e^{-\alpha l}}{\frac{S_b L_p}{D_p}\cosh(\frac{l}{L_p}) + \sinh(\frac{l}{L_p})}\right] \tag{3.25}$$

Where D_p and D_n are hole and electron diffusion coefficients; L_p and L_n are hole and electron diffusion lengths, S_f and S_b are front and back surface velocities and l is thickness of n and p sides.

These are the equations describing the external quantum efficiency for hole and electron currents. To calculate EQE_P and EQE_n the parameters L_p, L_n, D_p, D_n, S_f, S_b, l and w are needed. L_p, L_n, D_p, D_n, l and w can be calculated for a silicon photodiode. [81]. The remaining parameters S_f, can be S_b obtained by normalizing the above

equations to the data points one at the blue end of the spectrum and one at the near infrared end.

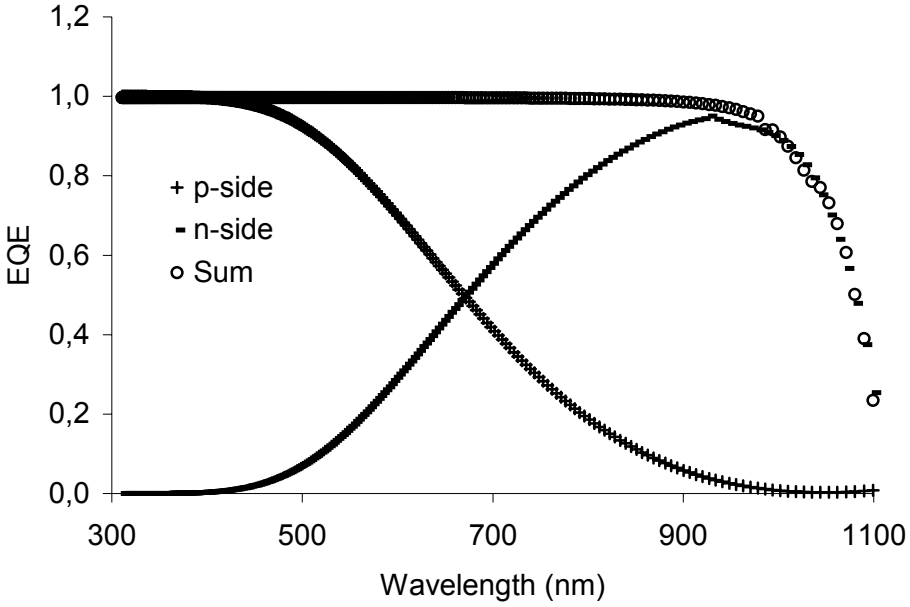

Figure 3.26: Modeling of EQE of trap detector.

3.3.4 Realization of responsivity scale from 350 nm to 850 nm

Spectral responsivity of a trap detector as given in equation 3.3 is defined with the reflectance and the internal quantum efficiency. Having seen that both the internal quantum efficiency and the reflectance of trap detector obtained effectively by the combination of measurements and developed models, the spectral responsivity scale can be realized using equations 3.3, 3.19 and 3.20. Comparing the calculated and measured values, it was seen that there is a good agreement between them. Hence we decided to use this model for the realization of spectral responsivity from 350 nm to 850 nm as shown in figure 3.27. Spectral responsivity in this interval is

realized with a relative standard uncertainty of 0.25 %. Various sources of uncertainty and their contributions to uncertainty are given in table 3.1.

Table 3.1: Uncertainty budget for responsivity measurements of trap detectors

Source of uncertainty	Relative standard uncertainty x 10^{-2}
Absolute responsivity	0.025
Light stability	0.050
Homogeneity	0.020
Nonlinearity	0.002
Polarization sensitivity	0.010
Multimetre	0.001
Transimpedance	0.002
Stray light	0.020
Scattered light	0.050
Diffuse Stray light	0.050
Temperature variation	0.050
Long term stability	0.020
Interpolation	0.010
Reflectance	0.008
Repeatability of Responsivity Measurements	0.074
Expanded uncertainty (k=2)	0.25

3.3.5 Extension of Responsivity Scale to UV (250 nm) and NIR (2500 nm)

Expanding responsivity measurements beyond the modelled IQE of trap detectors requires different calibrated detectors. Detectors are required that cover the spectral regions of measurement interest and also overlap with the trap modelled IQE spectral region. If the relative responsivity of the detector were known, comparison with trap detectors would then transfer the spectral responsivity scale to the detector. This detector could then be used as transfer standard.

One method to extend the spectral range of the responsivity measurements is to use a spectrally flat detector. The spectrally flat detector could be calibrated by comparison with the trap detector as a working standard. A second method is to use a spectrally flat detector to measure the relative responsivity of another detector. This detector could then be calibrated by comparison with the trap detector and used as a working standard. The latter method was used to extend the spectral range of responsivity measurements. The transfer method described here uses one broadband, spectrally flat pyroelectric detector. The flatness of the responsivity is determined by measuring the reflectance from the pyrolectrics surface.

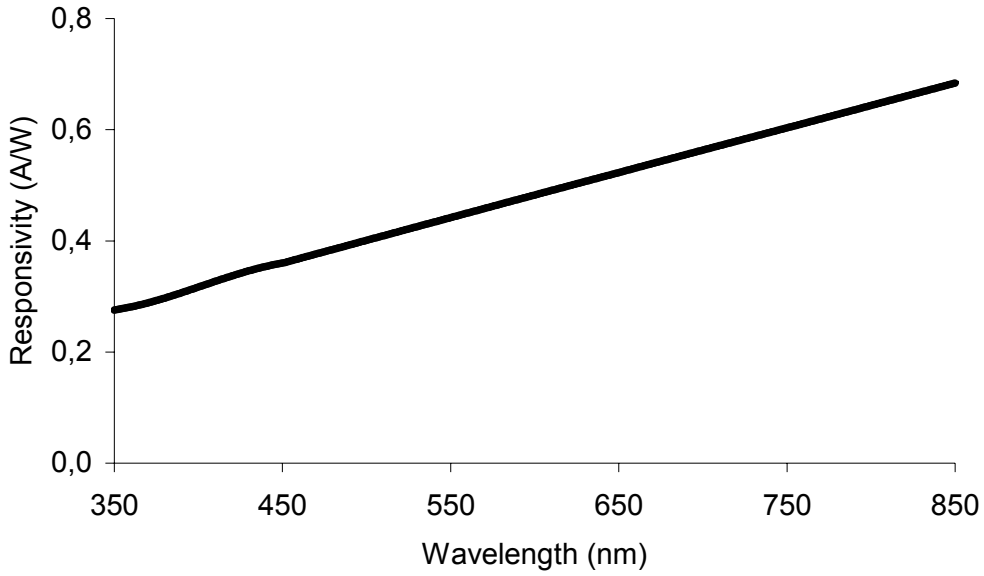

Figure 3.27: Responsivity of trap detectors obtained from combination of measured and modeled values.

CHAPTER 4

REALIZATION OF RELATIVE SPECTRAL RESPONSIVITY SCALE

4.1 Electrically Calibrated Pyroelectric Radiometer (ECPR)

The Electrically Calibrated Pyroelectric Radiometer (ECPR) system is a ±1% absolute accuracy radiometer, has been used as a transfer standard from UV to mid-IR range [82]. It can measure the total power and irradiance of continuous wave sources. The most common application for the ECPR is to transfer an absolute radiometric calibration to another detector or light source with a high degree of accuracy. This is accomplished by measuring either the total power (Watts) of collimated sources that under fill the detector aperture or the irradiance (W/cm^2) of extended sources that overfill the detector aperture. The exceptionally flat spectral response insures broadband sources are measured with the same accuracy as monochromatic light, allowing the ECPR to calibrate visible and IR detectors, standard lamps, blackbody emitters, laser power meters, UV exposure meters, etc [82].

The ECPR system as shown in figure 4.1 composed of a readout (Rs-5900), a pyroelectric probe (RsP-590), and an optical chopper (CTX-515). The major components are illustrated in the block diagram in figure 4.2.

4.1.1 Readout

The Rs-5900 Readout consists of LED indicators for the active measurement status (Watts or W/cm) and the active probe (RsP-590 Pyroelectric or RsP-595 Silicon), the mode enunciator for power measurement or system test mode. A 12-button keypad allows for numeric entry and selection of system functions such as

Units (Watts and dBm), Range Select, Auto Ranging, Calibration Factor Recall/Store, and the various Test Modes. It also provides access to various signal test points for system test and calibration, including the Preamp Out, Direct Out and Mixer Out.

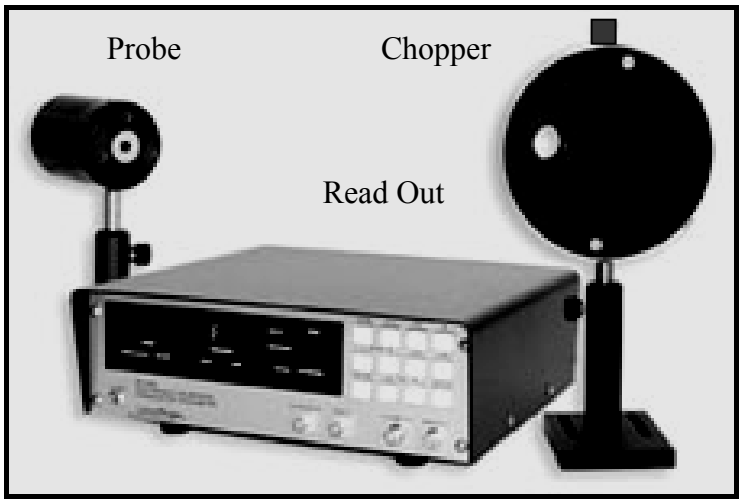

Figure 4.1: Electrically Calibrated Pyroelectric Radiometer System.

4.1.2 Pyroelectric Probe

The grooving requirement for sensitive infrared detectors that operate at room temperature motivated the development of the pyroelectric detector. The pyroelectric detector is important because it has proven to outperform other un-cooled thermal detectors. The most important pyroelectric detectors consist of triglycerine sulfite (TGS), strontium barium niobate, polyvinyline fluoride, and lithium tantalate ($LiTaO_3$) [83].

Pyroelectric material of ECPR present in UME made from $LiTaO_3$, has a spontaneous or permanent polarization. This polarization is governed by the material temperature, by the crystal symmetry and bonding. The known pyroelectric materials

are dielectrics, and change in polarization results in a proportional change in dielectric constant [83]. This temperature dependent polarization causes charge to flow if connected to external circuit. The pyroelectric detector is coated with a gold-black which functions as both a spectrally flat absorber for the incident optical radiation and the heating resistor for the electrical substitution servo-loop circuit. The pyroelectric probe consists of a pyroelectric detector assembly and preamplifier in a common housing.

4.1.3 Chopper

CTX-515 is a 15 Hz, 50% duty cycle optical chopper. It both modulates the optical signal impinging on the RsP-590 Probe and provides the reference signal to the lock-in circuitry in the Rs-5900 Readout. A phototransistor is mounted in the chopper housing diametrically opposite to aperture to generate an electrical reference signal having 50% duty cycle and 180^0 out of phase from the chopped signal. The 2.5 cm diameter aperture can be rotated to adjust the phase relationship between the optical signal and the electrical reference signal. A part of this reference signal is amplified and passed through the front electrode of the detector to provide electrical heating signal. The other part of the reference signal is used for phase sensitive rectification in the lock in amplifier.

4.2 Operation of ECPR

The ECPR employs a unique auto-nulling electrical substitution technique that precisely generates and measures an electrical signal equivalent to the optical signal incident on the probe [82]. The radiation to be measured is interrupted by 15 Hz 50 % duty cycle chopper. This is placed as close as possible to the radiation source so as to minimize chopped background radiation [83]. When the chopped optical signal is aligned to incident on the pyroelectric material, the resulting time variation in its temperature will produce a measurable ac current. This current can be

detected by use of a lock-in amplifier, with the chopping frequency used as the reference. Since the ECPR is tuned to a single frequency, its operation is affected by the phase and waveform of the chopped radiation. The optimum condition is a square optical waveform out of phase with the electrical drive. This is obtained with a narrow radiation beam centered in the chopper aperture. Measurement errors due to non-centering of radiation through the chopper aperture may be minimized using an oscilloscope as shown in figure 4.3.

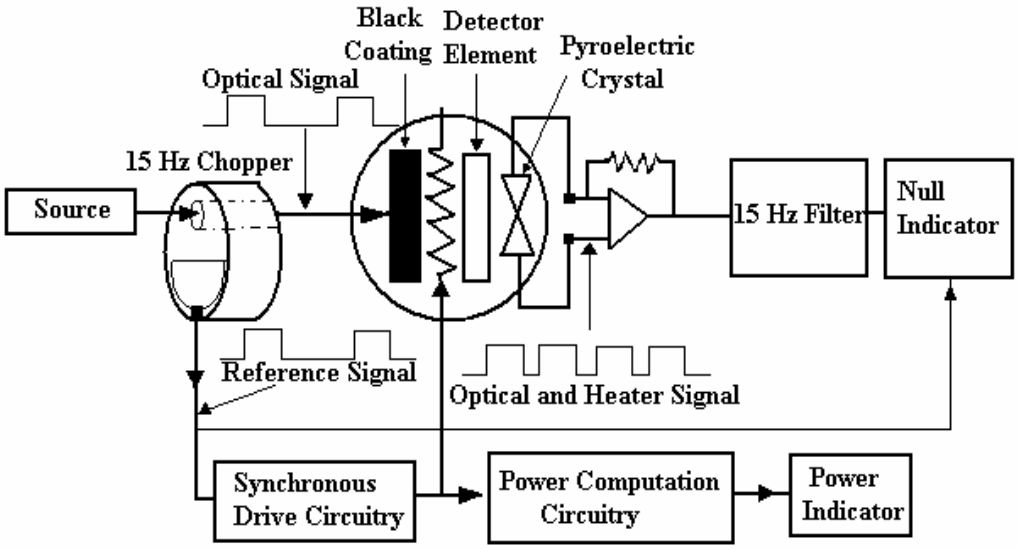

Figure 4.2: Schematic diagram of electrically calibrated pyroelectric radiometer.

The ECPR also incorporates frequency sensitive lock-in amplifier circuitry that automatically rejects any input optical signal that is not frequency matched to the chopping rate, thereby insuring that any optical radiation that strikes the detector without having passed through the optical chopper is ignored [83].

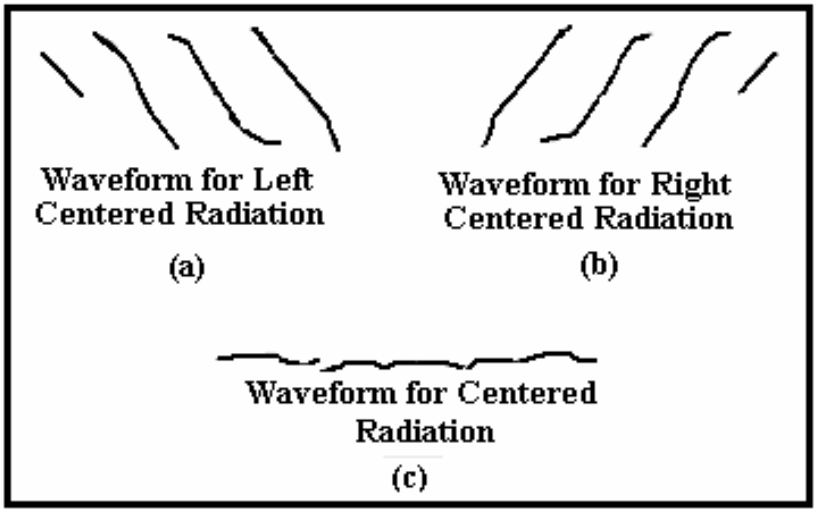

Figure 4.3: Chopper arrangement of ECPR.

When the chopper is open the pyroelectric detector produces a thermal signal proportional to the optical power incident on the gold-black absorber material. When the chopper shuts the servo-loop generates electrical current pulses that pass through the gold-black, which now functions as a precision heating resistor. This electrical power (I^2xR) causes the pyroelectric detector to produce a thermal signal proportional to the electrical power [84]. The servo-loop increases the magnitude of the current pulses until the null condition is reached at the output of the synchronous rectifier circuit. At this point the optical power is equal to the electrical power, and the electrical power is digitized and displayed. Wave form representations of optical and reference signals at various stages are illustrated in figure 4.2. When optical and electrical heating are balanced, the detector output is approximately a square wave at twice the chopping frequency.

The detector output is processed by a current mode preamplifier designed to have a flat response up to approximatelly 500 Hz. The resultant low impedance signal is fed into a waveform independent synchronous rectifier, locked to the chopper, and adjusted so as to measure the difference between the integrated signals within successive half periods at 15 Hz. The output of the synchronous rectifier (null

indicator) is zero when the optically and electrically induced thermal signals are equal.

4.3 Optical Characterizations of ECPR

To test the performance of ECPR the response non-uniformity, non-linearity, chopper duty cycle and reflectivity of pyroelectric probe have to be investigated.

4.3.1 Response Non uniformity

Spatial non-uniformity of detector response occurs primarily because of thickness variations in the detector element. $LiTaO_3$ is a hard, brittle material and it is proven to be quite difficult to obtain a high degree of surface flatness and parallelism with thin samples required for proper operation. The resulting response variation is important for two reasons. First, it directly limits accuracy attainable with a small illuminated area such as that characteristic of laser measurements. Second, when combined with the difference between electrically and optically excited areas, it leads to an overall correction factor [83,85,86]. One approach to the problem is to map the optical response over the detector surface. The map can then be used to obtain a correction factor for a particular radiation distribution of interest.

The spatial non-uniformity in the response of ECPR is shown in Figure 4.4. These data were obtained by scanning the detector over a 5 mm x 5 mm region in 0.5-mm steps, using the same size beam as was used for the measurements. The signals were normalized to a value obtained at the center of detector to detect relative variation of responsivity. For the region within about 3 mm x 3 mm of the center, the maximum variation in the detector response is ± 0.84%. This rather substantial non-uniformity is likely to vary from detector to detector and could be improved with a better absorbing coating.

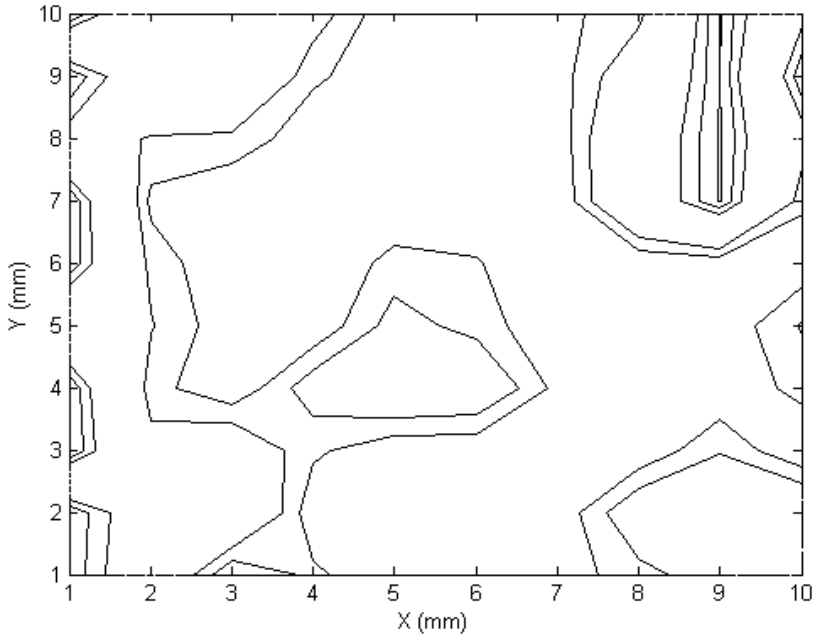

Figure 4.4: Spatial response variation of the pyroelectric detector.

4.3.2 Reflectance Measurements

Since thermal detectors rely on only the amount of heat energy delivered, their response is independent of wavelength. Being thermal detector pyroelectric materials have spectrally flat response over a broad wavelength range. The change in the responsivity of these detectors is due to the reflectance of the face electrodes and other materials placed on the detector surface to efficiently convert optical energy into thermal energy [83]. Therefore spectral responsivities of these detectors are derived from spectral reflectance measurements.

The spectral reflectance of pyroelectric probe of ECPR is measured using monochromator, collimator, integrating sphere, lock in amplifier, ECPR head and detector system as shown in figure 4.5. As radiant sources tungsten halogen lamp is used. Silicon photodiode trap detector, InGaAs and HgCdTe detectors are used for detecting the signals. The spectral reflectance is compared with a white barium sulphate ($BaSO_4$) reflectance standard. A collimated beam oriented to incident to the

ECPR sensitive surface. The measured signal from radiation reflected from $BaSO_4$ is used as the value for 100% reflectance. The spectral reflectance of ECPR at each wavelength is calculated from the averages of 50 measured reflectance values. The reflectance ρ at wavelength λ (Figure 4.6) was calculated using following equation.

$$\rho = \frac{A_{pd}(\lambda) - A_b(\lambda)}{A_{sd}(\lambda) - A_b(\lambda)} \tag{4.1}$$

In this expression, $A_{sd}(\lambda)$, is the average reflected signal of the white standard, $A_{pd}(\lambda)$ is the average reflected signal of the pyroelectric detector, and $A_b(\lambda)$ is the average signal of the background.

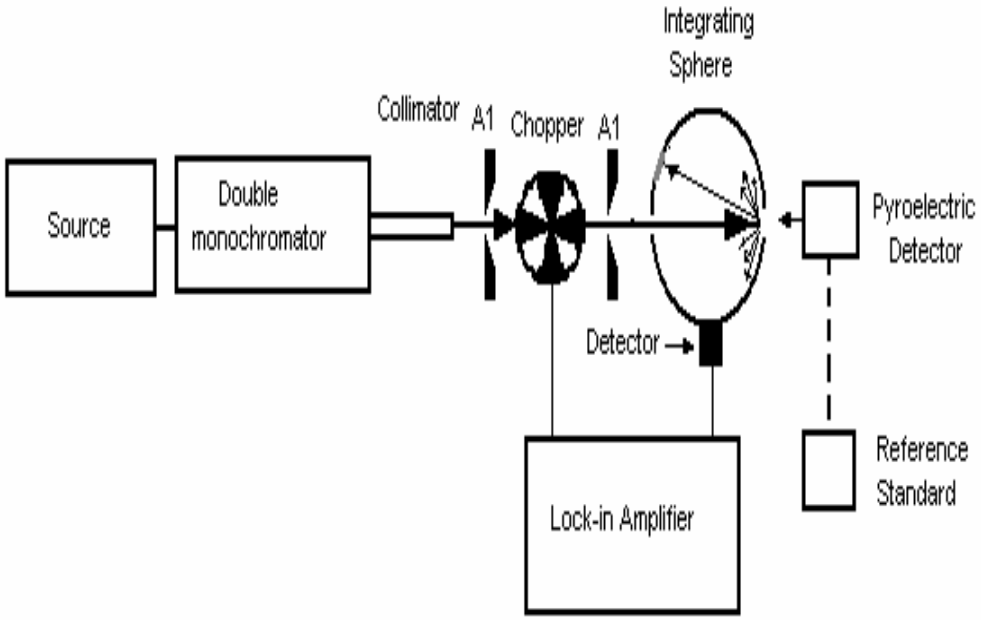

Figure 4.5: Reflectance measurement set up for pyroelectric detector.

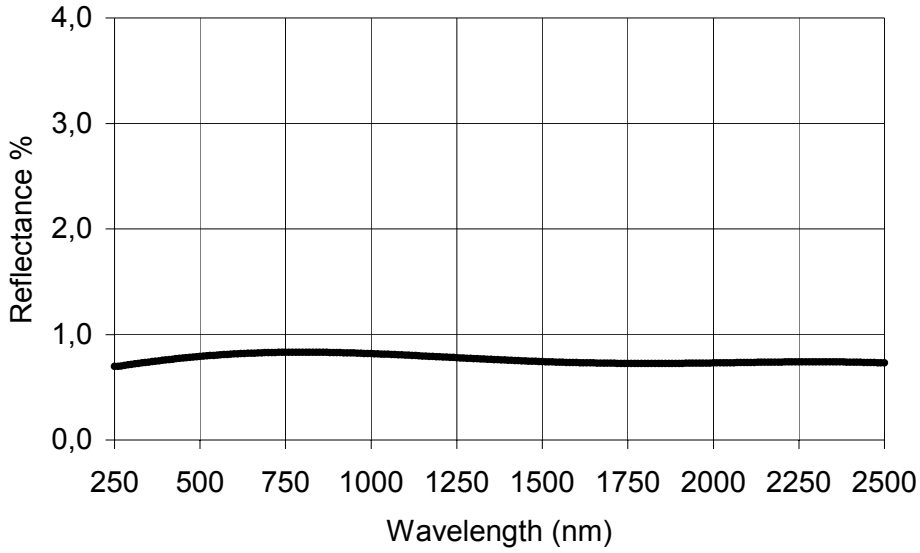

Figure 4.6: Spectral reflectance of gold-black coated pyroelectric detector versus wavelength.

4.3.3 Response Non-linearity

To measure the response linearity of pyroelectric detector, comparison with a linear reference detector technique was used. Intensity stabilized He-Ne laser with a stability of 0.006% was used as the light source. The radiant power response was measured with mechanically chopped, 632.8 nm wavelength laser beam for input. Neutral density filters were used to attenuate the laser power at seven levels ranging from 1 mW to 1 nW. The reference for the response linearity of pyroelectric detector was a silicon based trap detector. During the test pyroelectric detector position was altered with the reference trap detector position. Comparing the measurements results a linearity of on the order of 10^{-5} was obtained.

4.3.4 Responsivity Measurements

Pyroelectric materials are inherently spectrally flat over a broad wavelength range. Therefore the spectral responsivity of a pyroelectric detector dependens on reflectance of the face electrodes and other materials placed on the detector surface to efficiently convert optical energy into thermal energy [83,85-87]. The absorbance of the gold black coating determines the relative spectral responsivity, provided the transmition through the detector is negligible and the reflectance is low. Then the relative spectral response of the detector can be determined from a spectral reflectance measurement, if we assume that the gold black transmittance is negligible and the relative detector response is proportional to 1 minus the measured reflectance. Using the law of conservation of energy the absorptance $\alpha_p(\lambda)$ is given as [87]

$$\alpha_p(\lambda) = 1 - \rho_p(\lambda) \tag{4.2}$$

where $\rho_p(\lambda)$ is the reflectance and the transmittance $\tau_p(\lambda)$ is assumed to be equal to zero. The predicted spectral responsivity $R_p(\lambda)$ of the pyroelectric detector is [87]

$$S_p(\lambda) = \left[1 - \rho_p(\lambda)\right] CF_p \quad \left[\frac{A}{W}\right] \tag{4.3}$$

where CF_p is the calibration factor, which scales the output signal to the optical power received by the pyroelectric detector, is determined by calibrating ECPR against ESCR.

Besides the reflectance of pyrolectric detector coating the main parameter that mostly affect the calibration factor to be slightly different is spatial non-uniformity. Therefore in order to obtain a correction factor to compensate the effects arise from illuminated area, we multiplied equation 4.3 with a homogeneity correction factor HCF_p need to be mapped over the detector surface.

$$R_p(\lambda) = \left[1 - \rho_p(\lambda)\right] \times CF_p \times HCF_p \qquad \left[\frac{A}{W}\right] \tag{4.4}$$

4.3.5 Calibration of ECPR against ESCR

The optical system used to calibrate ECPR system against ESCR is shown in figure 4.7. The responsivity of ECPR was measured in terms of Amper/Watt. Intensity stabilized laser beam was sent into the ESCR where optical power was measured absolutely. Then the current response of ECPR was measured by moving it into the optical path entering ESCR.

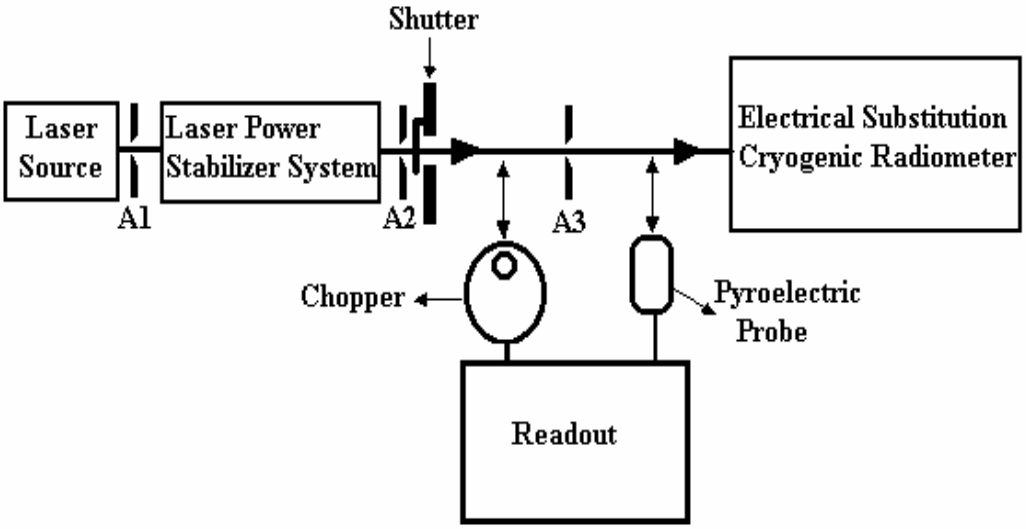

Figure 4.7: Responsivity measurement of ECPR system against ESCR.

As it was mentioned with ECPR the optical and electrical signals equated that is when null condition is reached data can be recorded. However signal-displaying time is too short due to the null condition time. So, the limited data can be recorded

during each null condition time. To get more data in each null condition time we developed 8-channel 8-bit ADC card, which is ISA bus compatible, to take electrical voltage directly related to the power level of light. Main element of the card is an ADC 0808, which has tri-state (1, 0, Hi-Z). This card is capable of reading the voltage proportional to the power level of light through ISA bus when the null condition led turn on. A physical link was made between the null condition LED of ECPR and the 3rd bit of status port parallel port, which operates in Standard Parallel Port (SPP) mode. A suitable software instruction based on C/C++ is made so that when the null condition is reached, the mentioned 8-bit ADC samples the voltage proportional to light power level. The voltage data is stored on the files that are opened by software, which can be opened under MS Excel. Voltage is taken in parallel format through 0x303 H address over the data port of ISA and the data is processed in the software developed. The conversion time of ADC is 100μsec and reference voltage is 2,5 volt. The resolution of card corresponding to this reference voltage is approximately is 10 mV.

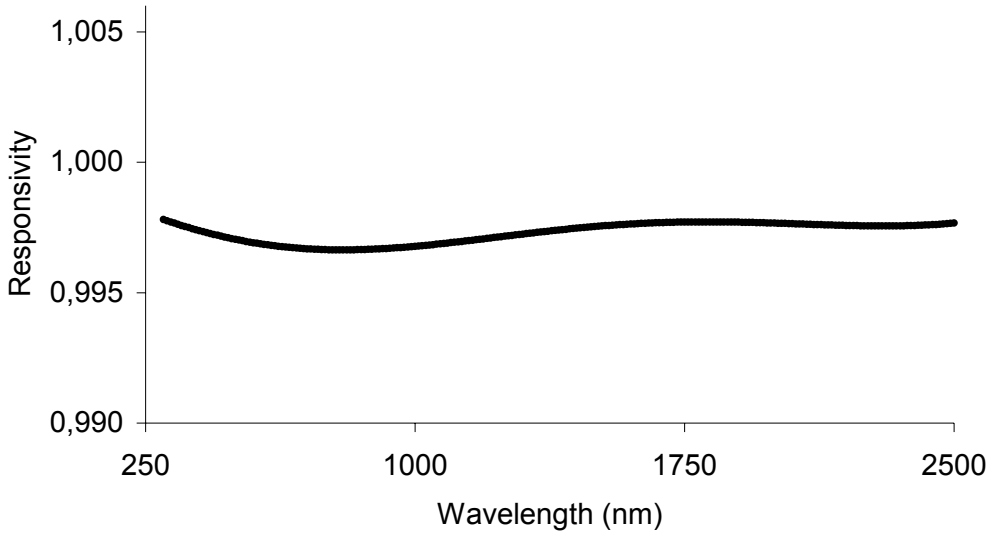

Figure 4.8: Spectral reflectance measurement results of pyroelectric detector.

ECPR was calibrated against ESCR at vertically polarized tunable Ar+ (488 nm, 514.5 nm), He-Ne (632.8 nm) and Nd:YAG (532 nm) lasers wavelengths with a standard uncertainty of 0.50 %. The sources of uncertainty and their contributions to uncertainty are given in the table 4.1 . At four laser wavelengths an average calibration factor of 1.005 was found. After determining the calibration factor, using equation 5 and reflectance values measured in section 4.5.2 the spectral responsivity was realized from 250 nm to 2500 nm.

Table 4.1: Uncertainty budget for responsivity measurements of ECPR.

Source of uncertainty	Relative standard uncertainty x 10^{-2}
Power	0.006
Light stability	0.002
Homogeneity	0.126
Wavelength calibration	0.020
Reflectance	0.173
Repeatability of Responsivity Measurements	0.128
Expanded uncertainty (k=2)	0.50

4.4 Relative Spectral Responsivity Measurements of Working Standards Using Spectrometer

The relative spectral responsivity scale at UV and NIR wavelengths is made in conjunction with the reference spectrometer. The configuration of the reference spectrometer for spectral responsivity measurements is shown in figure 4.9. The central unit of a reference spectrometer is the monochromator whose basic elements are shown in figure 4.9 and its important parameters are given in the table 4.2. Having interchangeable gratings and order sorting filters, it covers the range 200 nm to 30 μm, and it is fully programmable via PMC3B dual output stepping motor drive

[88]. In double monochromator design independent control of two halves achieves a degree of wavelength tracking. Accurate wavelength tracking allows a narrow central slit, which optimizes the signal to scattered light ratio.

Table 4.2: Monochromator parameters.

General Specifications	
Focal Length	300 mm
Slits	10μm to 10 mm variable
Slit Height	20 mm
Number of Gratings	3
Grating Size	68 mmx84mm
Aperture Ratio	f / 4.1 (at all grating angles)
Resolution	0.1nm at reduced slit height, 0.3 nm with full slight height of 20 mm.
Dispersion	2.7 nm / mm
Mechanical Resolution of Grating Drive	0.0018 degrees per motor step
Wavelength Acquisition Speed	1000 nm / sec
Wavelength Accuracy	± 0.2 nm
Wavelength Reproducibility	± 0.5nm

The input optics of spectrometer in figure 4.9 includes a spherical concave and a cylindrical concave mirrors to image the source onto the monochromator entrance slit with a magnification of two. This magnification provides a complete illumination of the grating aperture with some overfilling. The overfilling increases the stray light slightly, but minimizes sensitivity to misalignment. The purpose of the cylindrical mirror is to correct for astigmatism of the optical system [89]. The mirrors are made from glass; substrate, aluminum coating, and magnesium fluoride overcoat which makes the reflections of the input optics independent of wavelength in the spectral ranges of interest. The light emitted by the source and reflected by the condensing mirrors passes; the order-sorting filter wheel before reaching the entrance slit. The order sorting filters are interchanged at nominal wavelengths to stop the

radiation from higher-order diffraction of spectrum that would overlap with the working range. The order sorting filters used in the monochromator are given in the table 4.3. The flat mirror diverts the light from the slit to the first collimating mirror, which in turn illuminates the diffraction grating by a parallel white light beam.

The monochromator holds up three, permanently mounted gratings on a rotating turret (Table 4.3). Grating selection and positioning are completely programmable. A combination of mechanical gearing and micro stepping results in a resolution of 500000 steps per revolution of the turret and the wavelength acquisition speeds in excess of 500 nm/sec in the visible. The grating disperses the light and a narrow-band (near-monochromatic) beam is focused to the exit slit by the second collimating mirror and via a rotary flat mirror. This mirror is rotated away to view the beam onto the second exit slit during the alignment of the condensing optics.

In double monochromator grating in each halves must be rotated in exact synchronisation. This is be achieved by mechanically linking them together. To avoid backlash of the grating drive mechanism introducing uncertainty in the wavelength alignment it scan the spectrum in only one direction, usually from short to long wavelengths.

Table 4.3: Spectrometer parameters; filters and gratings.

FILTERS					GRATINGS		
Number	nm	Number	nm		Lines/mm	Max. Wavelength (nm)	Blaze Wavelength (nm)
1	0	5	2000				
2	400	6	3800		1800	900	500
3	700	7	7000		600	2500	1600
4	1200	8	12000		100	16200	9000

The light beam emerging from the slit is diverted and collimated by a 90-degree off axis parabolic mirror. A small limiting circular aperture is placed in front

of the exit slit to decrease the scattered light from the slit blades of the monochromator. A baffle with a circular aperture is used to stop the stray light scattered by the off -axis mirror. This optical set-up can also be applied for measurements of spectral transmittance, reflectance, and responsivity The light sources used in the measurements are tungsten halogen and deuterium lamps. Their spectral distributions are given in the figures 4.10, 4.11. These lamps cover a wide spectral range, including the UV, VIS and NIR regions. Although the quartz tungsten halogen lamp produce useable outputs in the UV region, at least down to 200 nm, the output of these short wavelengths is quite low and declines rapidly with wavelength. Deuterium arc lamp overcome this limitation of the quartz tungsten halogen lamp in this spectral region, and they do so with little output above a wavelength of 500 nm except for a strong but narrow emission line at about 660 nm [90].

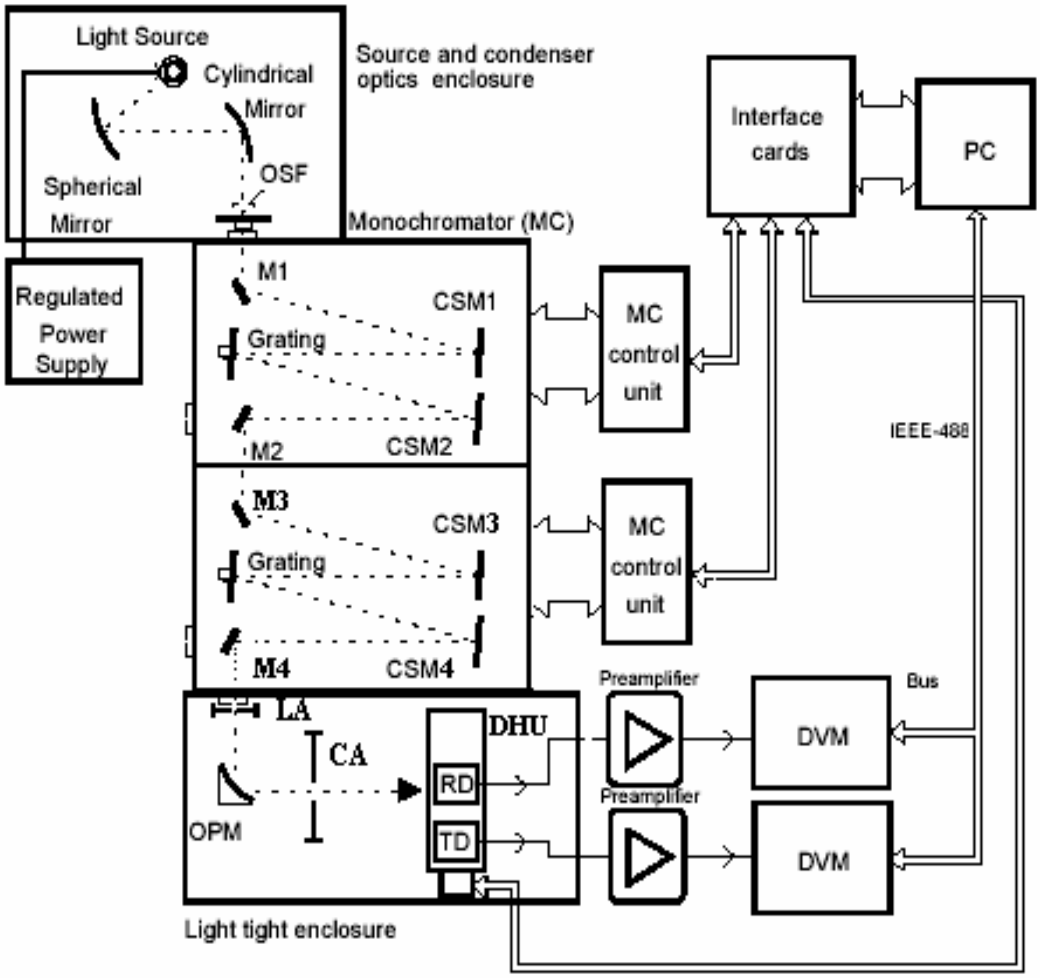

Figure 4.9: Schematic representation of the spectrometer configuration used in spectral responsivity measurements. OSF, order-sorting filter; CSM1, CSM2, CSM3, CSM4 collimating spherical mirrors; M1, M2, M3, M4 flat mirrors; CA, circular aperture; LA, limiting aperture; OPM, off-axis parabolic mirror; DHU, detector holder unit; RD and TD, reference and test detectors; DVM, digital voltmeters.

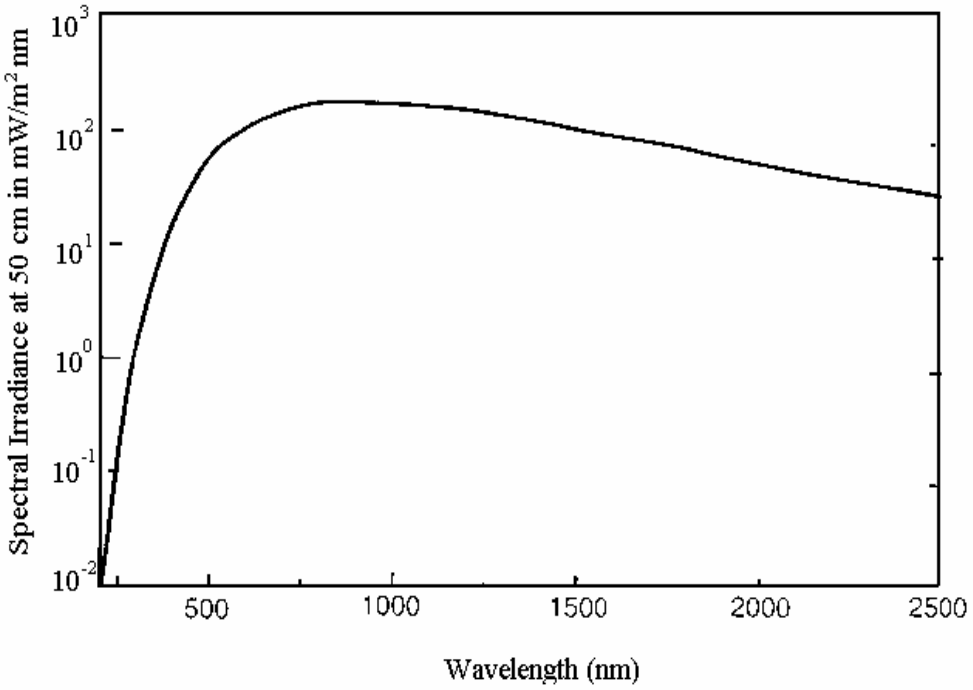

Figure 4.10: Spectral irradiance from a quartz halogen lamp 50 cm from the filament.

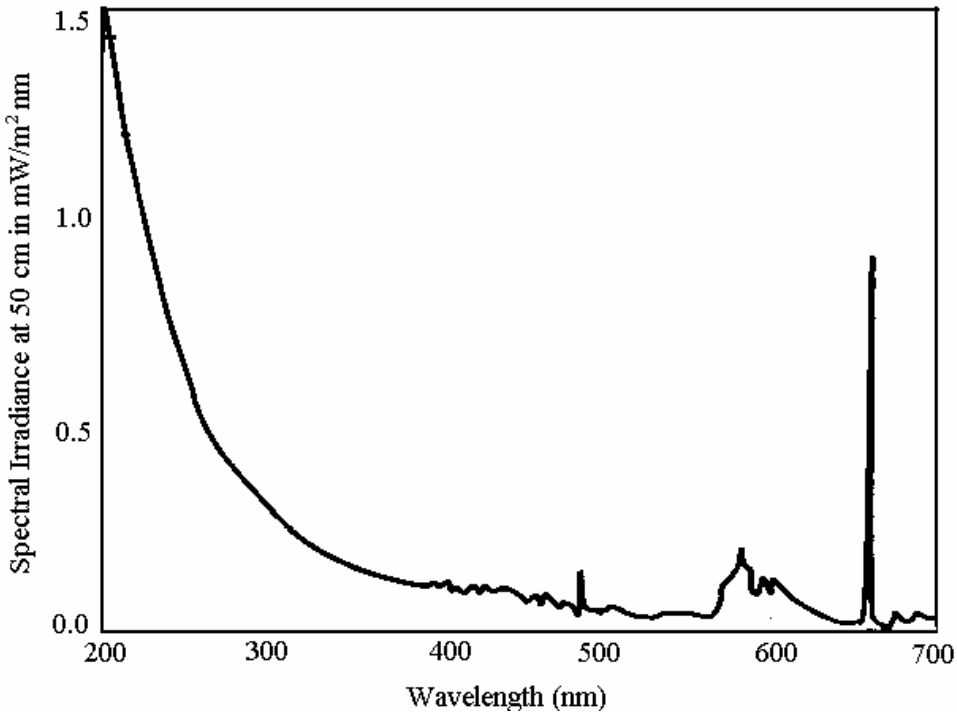

Figure 4.11: Spectral irradiance of a deuterium lamp 50 cm from the filament.

4.5 Relative Spectral Responsivity Measurements of Silicon (Si), Silicon Based Trap detector (TD), Germanium (Ge), Indium Galium Arsenide (InGaAs) and Photometer Heads in UV, VIS and NIR Regions

This part of the work deals with the investigations of the relative spectral responsivity within ultraviolet and the near-infrared spectral range using Si, Ge, InGaAs photodiodes, trap detectors and photometer heads. Si and Si based trap detectors are most commonly used detectors in the spectral range from 250 nm to 1100 nm both as working and transfer standard. Photometer heads have silicon based detector and V-lambda filter, used in realization of photometric units. Ge and InGaAs detectors are mainly used in the spectral range from 850 nm to 1800 nm. Calibrations of Ge and InGaAs detectors in the NIR spectral region are very much desired for two main reasons [91].

- In recent years, the application of optical fibers in the fields of telecommunications, optical metrology, material processing, diagnostics etc has greatly increased.
- The Nd: YAG laser at the wavelength 1064 nm is very common as one of the universal working tools in radiometry. Therefore, a careful spectral characterization of transfer detector standards for the NIR is necessary. It is the prerequisite for a low transfer uncertainty within the so-called radiometric chain [92], because these detectors can be used as a link between cryogenic radiometers as the national primary standards [93] on the one hand and the users or calibration laboratories on the other.

The relative responsivities were measured using the set up given in figure 4.9. The reference detector in UV and NIR regions is a spectrally flat ECPR, whose spectral characteristic was studied in the section 4.5, allows us to derive relative responsivity scale between 250 nm and 400 nm using Si photodiode and Si trap detectors detectors, between 380 nm and 780 nm photometer heads and between 800 nm and 1800 nm using Ge and InGaAs detectors.

The relative responsivities of these detectors were measured using substitution method. The substitution method uses a reference detector (rd) to transfer its responsivity to test detector (td) as given in the following equation

$$R_{td}(\lambda) = \frac{V_{td}}{V_{rd}} \frac{G_{rd}}{G_{td}} R_{rd}(\lambda) \tag{4.5}$$

where V_{td} and V_{rd} are the output voltages of test and reference detectors respectively, G_{rd} and G_{td} are gains for transimpedance amplifiers. Here reference detector is the pyrolectric detector. R_{td} (λ) is the responsivity of reference detector at the specified wavelength.

Figures 4.12 - 4.20 show the spectral responsivity of Si, Si based trap detectors, Ge and InGaAs detectors. Since all the detection mechanisms in Si, Si based trap detectors, Ge and InGaAs photo detectors are wavelength dependent, i.e there is a peak in responsitivity with a fall of at both long and short wavelengths. The long wavelength (low photon energy) cut off occurs because there is a certain minimum photo-energy required to generate electron hole pairs. The short cut off is a function of two effects [94]:

- The responsitivity in terms of power drops off because there are fewer short wavelength photons per watt.
- At the extreme short wavelength end, the energetic photons may no longer be absorbed in the sensitive region. In the deep ultraviolet, absorption of photons before they reach the sensitive region is a problem. Detectors windows, or surface coatings can also contribute to the spectral shape of the responsitivity curve.

Responsivity of Si photodiode increases with wavelength reaches its peaks value of 0.5225 A/W at 930 nm and then decreases abruptly. Beyond 1100 nm it becomes almost transparent. The deviation of responsivity from theoretical value is due to variety of reasons. First, there are some defects at the interface between Si and SiO_2 interface, which cause loss of carriers. Next, electron hole pairs that form outside the depletion region have different photon electron hole pair collection efficiencies and recombination rates than electron hole pairs formed in the depletion region. Also, reflections at the diode surface are wavelength dependent.

Trap detectors made from single element Si photodiodes have better optical properties (polarization independency, low reflectance looses, high quantum external efficiency, predicted spectral responsivity in the visible region ect.) compared to Si

photodiodes. Therefore they have almost linear responsivity from 350 nm to 900 nm and reaches maximum value of 0.7445 A/W at around 950 nm.

The spectral responsivities of both InGaAs and Ge photodiodes are shown in figures 4.19 and 4.20. The responsivity of InGaAs photodiode increases sharply from about 0.1067 A/W at 850 nm to 0.7193 A/W at 1000 nm. Then the responsivity increases slowly below 1000 nm to 1600 nm. The cutoff at 1600 nm corresponds to the band gap of the InGaAs and the cutoff below 1000 nm corresponds to band gap of the topmost InP layers [95].

The spectral responsivity of Ge also measured from 850 nm to 1800 nm. Corresponding to the direct band gap of Ge, there is a very sharp cut-off of the responsivity at about 1590 nm [91,96]. The soft shoulder between 1600 and 1800 nm corresponds to the indirect band transitions and the finite thickness of the Ge wafer [96]. Compared to (spectrally non-extended) InGaAs detectors, the Ge detectors cover a broader wavelength range. That is there is a reasonable responsivity up to about 2000 nm. However, the lower shunt resistances (varies from 780 Ω to 830 Ω) of Ge make it difficult to handle at low radiation signals and at not well-defined temperatures[91].

In figures 4.21 and 4.22 spectral responsivity of photometer heads and in figures 4.23 and 4.24 spectral responsivity of filter radiometers are displayed. Both photometer heads and filter fadiometers consist of trap detector and filters. Photometer heads have filter that transparent to the wavelengths in the visible region and used in the photometric measurements. On the other hand filter radiometers can have various filters each time in order to be used in the irradiance measurements.

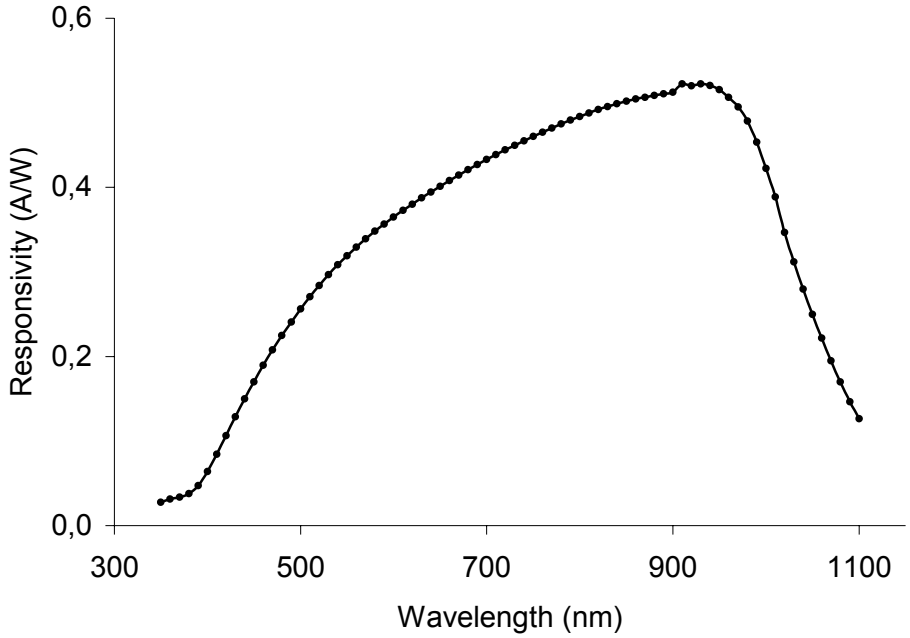

Figure 4.12: Spectral responsivity of silicon photodiode detector.

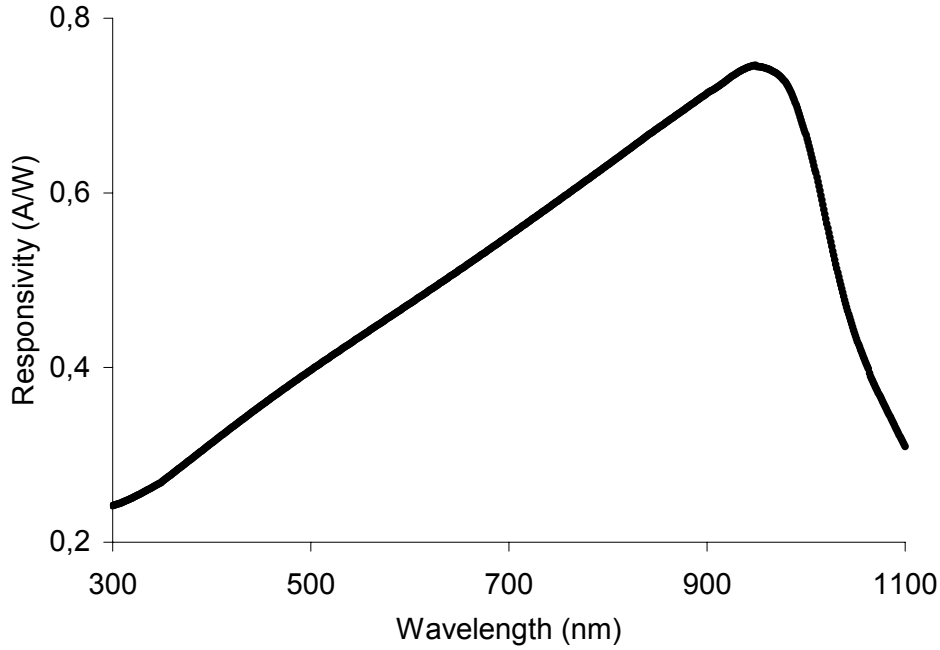

Figure 4.13: Spectral responsivity of trap detector (TD-1).

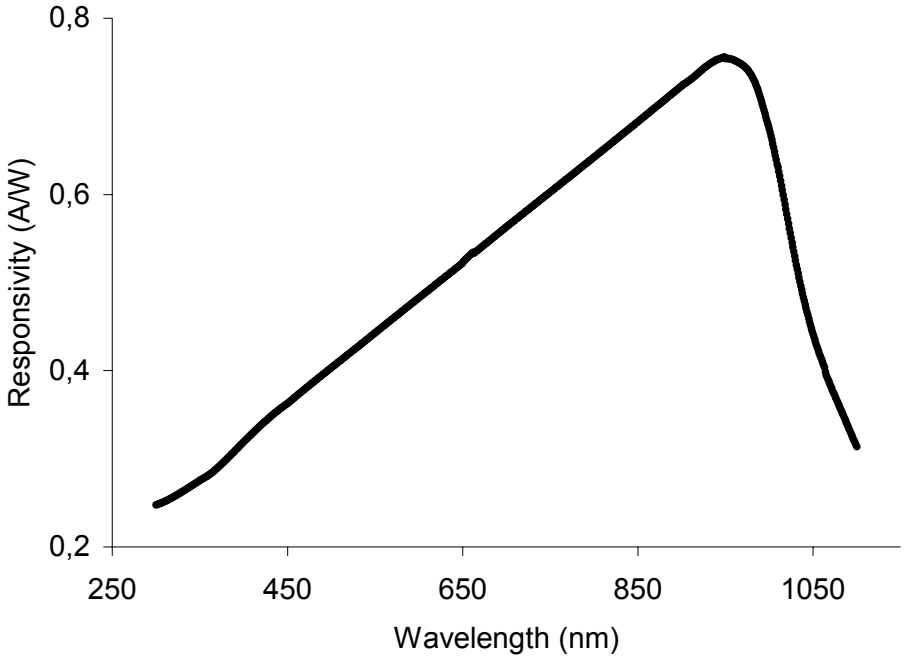

Figure 4.14: Spectral responsivity of trap detector (TD-2).

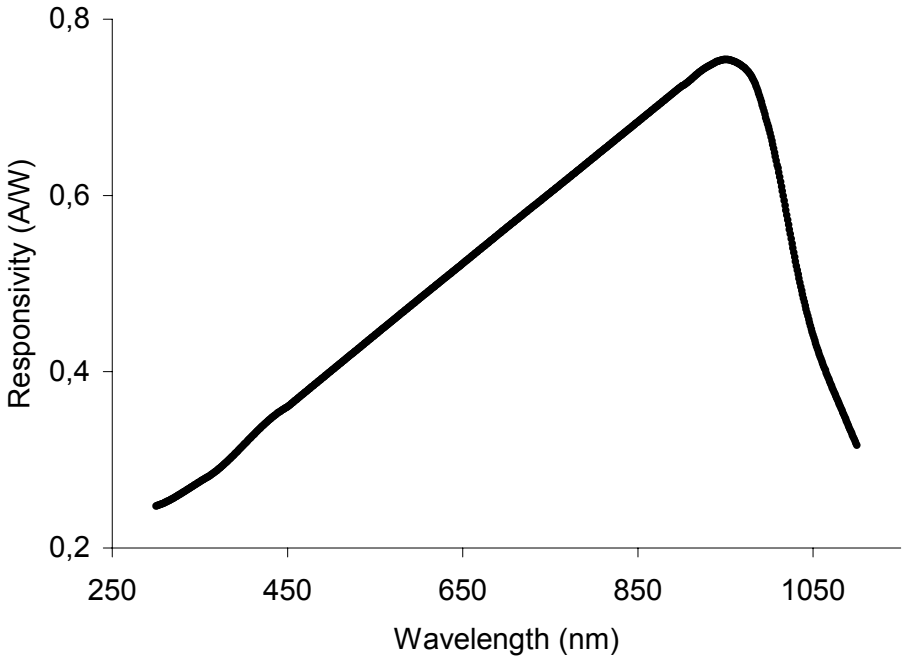

Figure 4.15: Spectral responsivity of trap detector (TD-3).

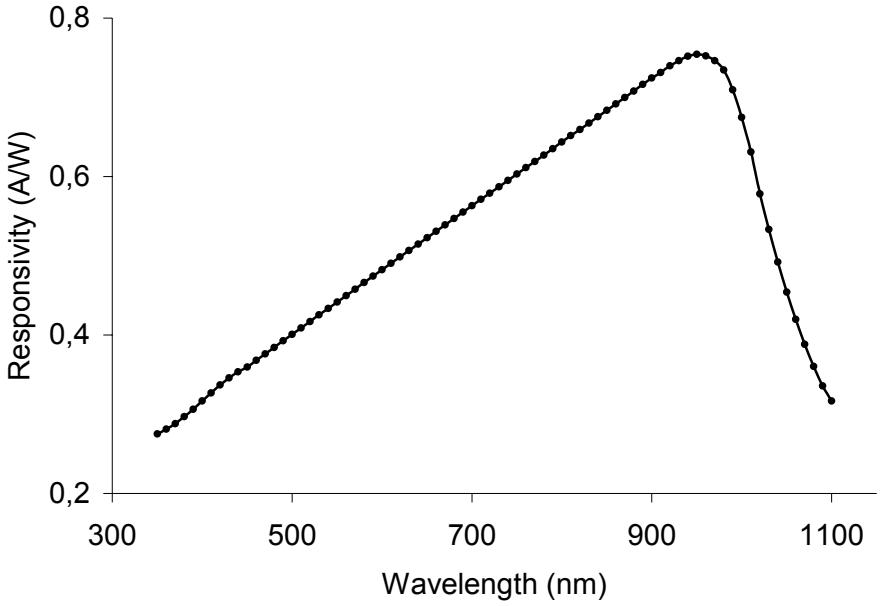

Figure 4.16: Spectral responsivity of trap detector (TD-4).

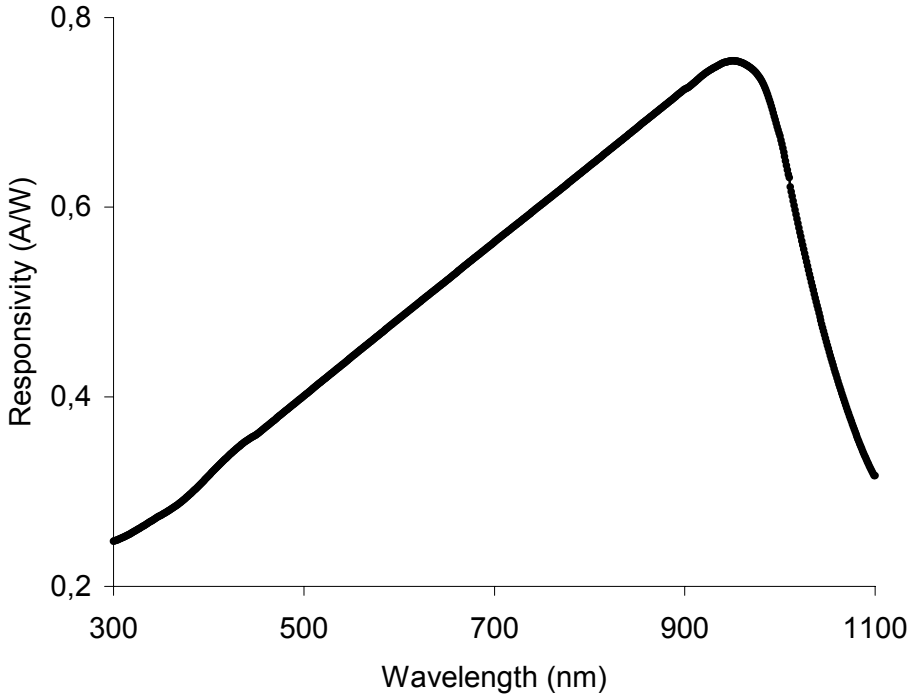

Figure 4.17: Spectral responsivity of trap detector (25.4).

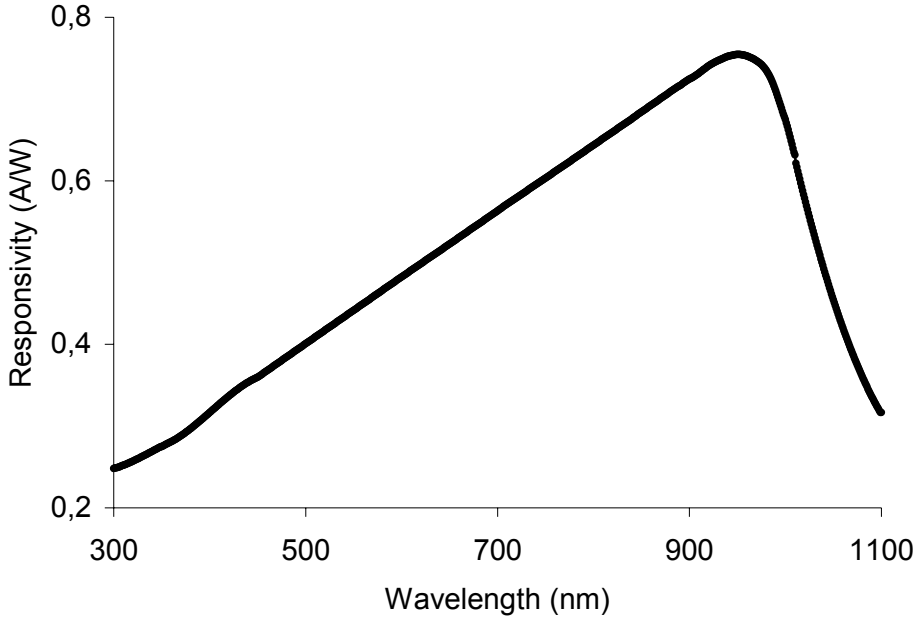

Figure 4.18: Spectral responsivity of trap detector (25.4-1).

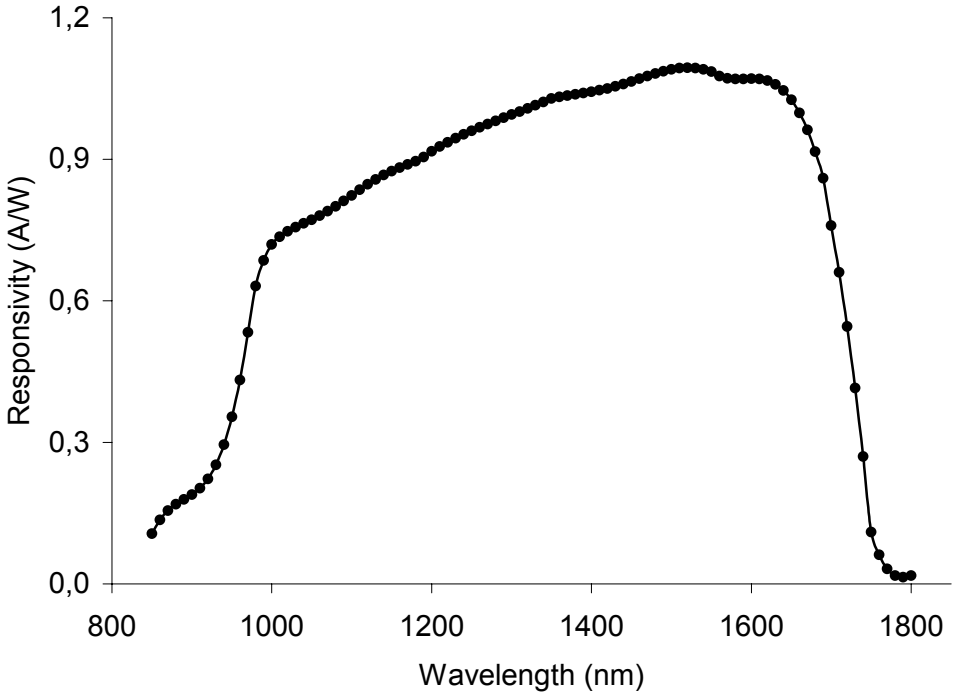

Figure 4.19: Spectral responsivity of InGaAs photodiode detector.

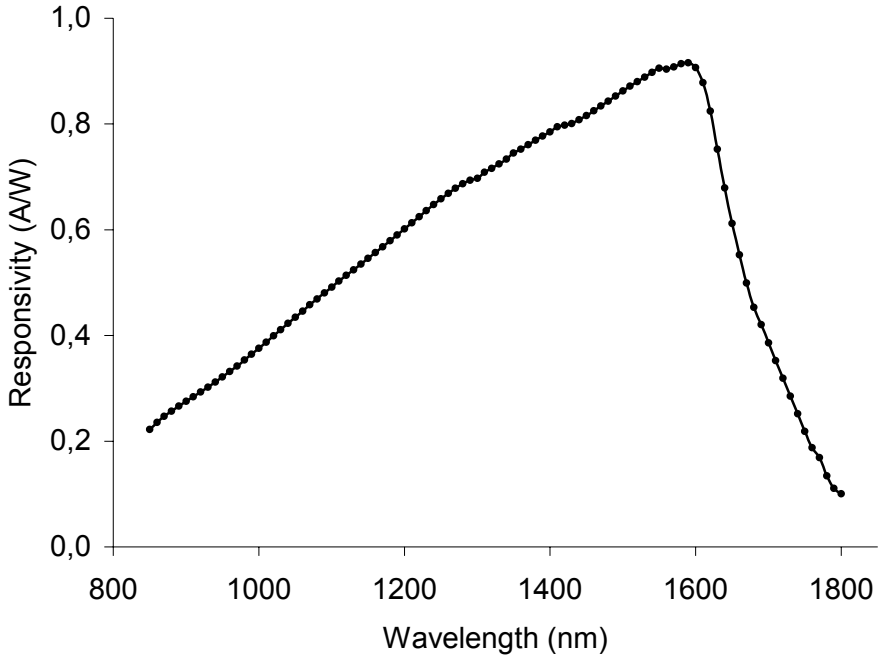

Figure 4.20: Spectral responsivity of Ge photodiode detector.

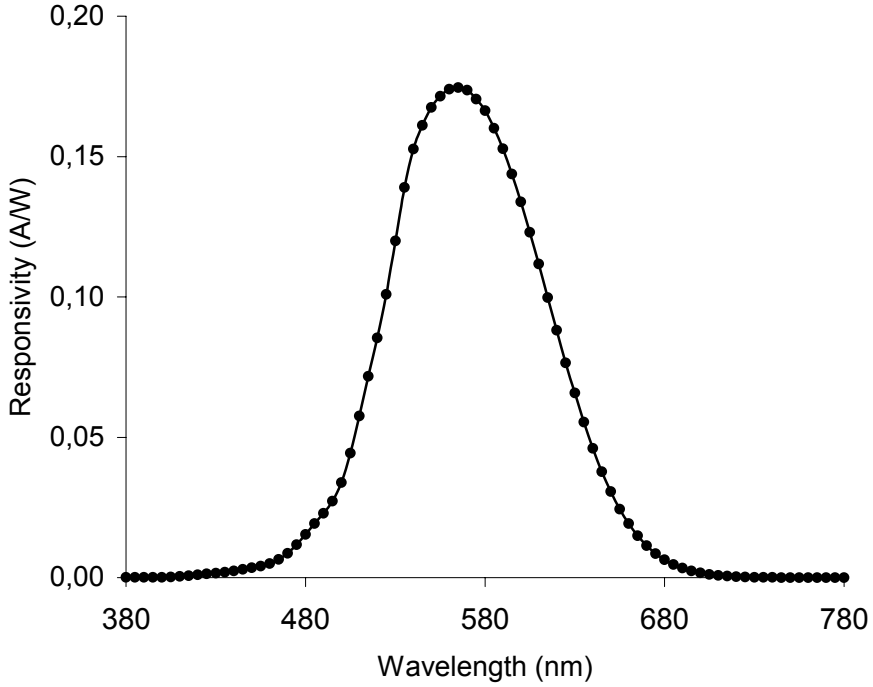

Figure 4.21: Spectral responsivity of photometer head (941114).

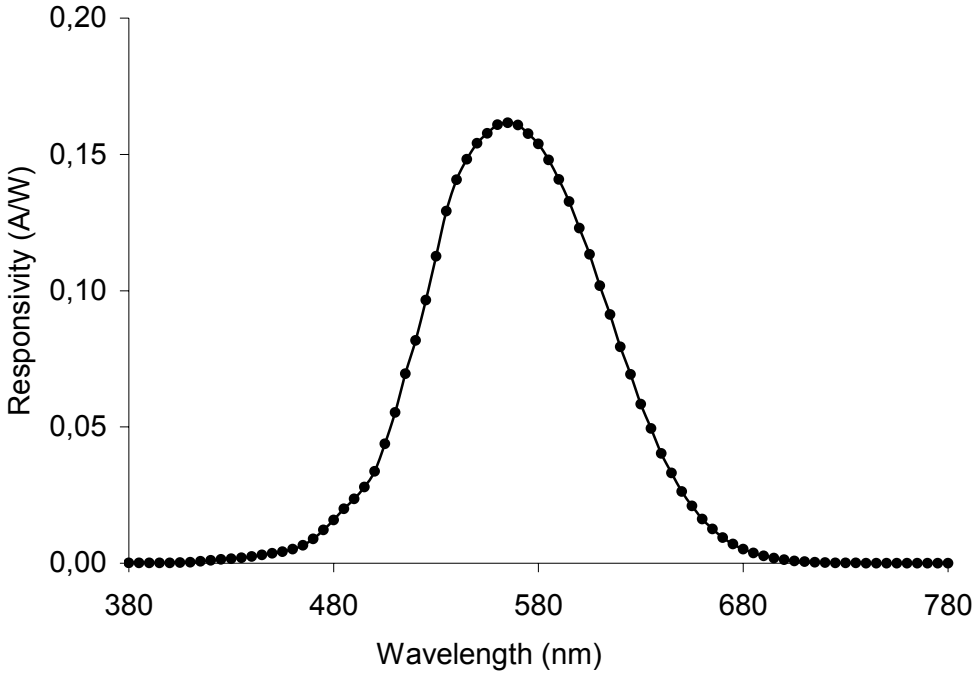

Figure 4.22: Spectral responsivity of photometer head.

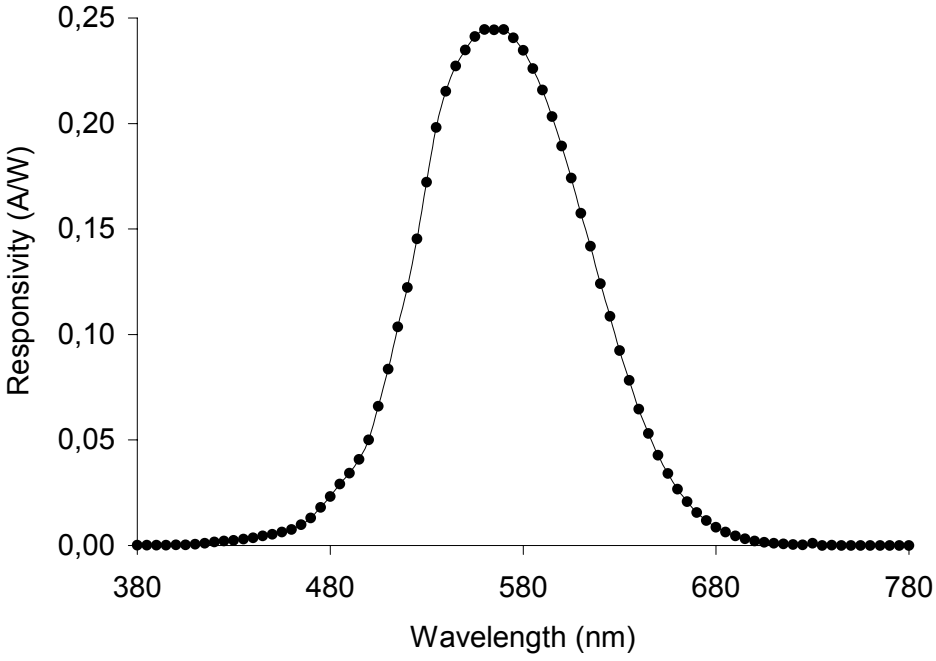

Figure 4.23: Spectral responsivity of filter radiometer (25.4).

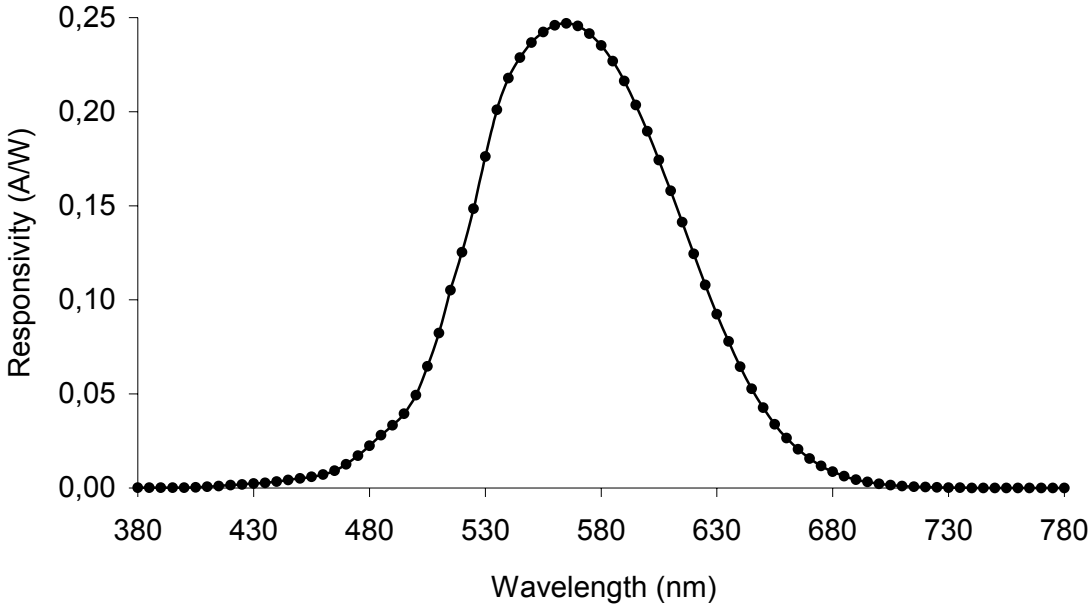

Figure 4.24: Spectral responsivity of filter radiometer (25.4-1).

CHAPTER 5

CONCLUSION

Absolute optical power scale has been realized by using helium cooled UME primary level electrical-substitution cryogenic radiometer. The scale was established at discrete laser wavelengths of vertically polarized tuneable Ar+, fixed He - Ne and Nd: YAG (with second harmonic) laser source. To generate a geometrically well-defined Gaussian laser beam a laser power stabilizer system was employed to the measurement system, which were kept power level stable to better than 0.001%. Performing the measurements at the highest level of accuracy require considerable care in preparations like power stabilization of laser beam, cleaning and transmittance measurements of window at the Brewster angle, minimization of scattered optical power and temperature-to-power sensitivity of radiometer cavity. The weakest component in this system is the window, because contamination's and its imperfect alignment to the Brewster angle affect the beam entering to the cavity too much.

Since the laser sources having different output power levels were used for the optical power measurements the sensitivity of the radiometer cavity to these power levels was checked by thermal link calibrations. The thermal link calibrations are important for obtaining minimum and maximum electrical power levels, which should be apply to the cavity by electrical heater. Because the sensitivity of cavity was found around 2.3 mK/μW, the power span for the electrical heating was kept as 5 μW. The absolute optical power was then measured and calculated at microwatt levels with relative standard uncertainty of 1.2×10^{-4} for 488 nm, 514.5 nm, 532 nm and 632.8 nm wavelengths and 1.5×10^{-4} for 457 nm and 1064 nm wavelengths.

After realization of absolute optical power scale the absolute spectral responsivity scale was established in UME between 350 nm and 850 nm wavelength

ranges. The scale is based on UME made reflection type trap detector consisting of three single element silicon photodiodes. The absolute responsivity was linked to the absolute optical power using laser stabilization optics and electrical substitution cryogenic radiometer system at discrete laser wavelengths. Then using physical models for the trap detectors, reflectance and internal quantum efficiency the absolute scale was realized with an expanded uncertainty of 0.05 %.

Moreover various measurements systems were established in order to make optical characterization of trap detectors like linearity, polarization sensivity, uniformity and spectral responsivity. For the nonlinearity measurements, flux addition technique was used and it was found that trap detectors in the 0.1 mW to 0.8 mW power ranges are linear within 10^{-5}. The polarization sensivity was obtained by measuring the responsivity as a function of rotation of trap detectors around the beam axis. Results shows that any misalignment of trap detectors leads to a maximum polarization sensivity of 10^{-4} in the responsivity. The uniformity measurements obtained by scanning of entrance aperture of trap detectors provides us the variation of responsivity across the detecting surface of trap detectors which is about $3x10^{-5}$ within the 6 mm diameter.

The relative spectral responsivity scale from 250 nm to 350 and from 850 nm to 2500 nm has been realized using ECPR traceable to the ESCR. ECPR was calibrated against ESCR at vertically polarized tunable Ar+ (488.1 nm, 514.6 nm) and Nd:YAG (532.0 nm) and fixed He-Ne (632.8 nm) lasers wavelengths with a standard uncertainty of 0.5 %. At four laser wavelengths an average calibration factor of 1.005 was found. The main parameters that mostly affect the calibration factor to be slightly different at each laser wavelengths are spatial non-uniformity and reflectance of pyrolectric detector coating. In order to obtain a correction factor to compensate the effects arise from illuminated area for each laser wavelengths, the optical response was mapped over the detector surface. For the 0.4 cm^2 region the spatial non-uniformity variation of responsivity was found to be less than 0.84 %.

Assuming the gold black transmittance of pyroelectric detector is negligible we have determined the relative spectral response of the detector from a spectral reflectance measurement. In the 250-2500 nm region the reflectance measurements indicated that the gold black coating is spectrally flat within 0.1 %.

REFERENCES

[1] K.Angstrom, Nova Acta R. Soc.Ups., ser.3 16, 1 (1893)

[2] F. Kurlbaum, Ann. Phys, 287, 591, (1894)

[3] CIE Pubblication No. 65, (1985)

[4] E. J. Gillham, Proc.R.Soc.London, Ser.A , 269, 249 (1962)

[5] L. P. Boivin and T. C. Smith, Appl. Opt., 18, 3067 (1978)

[6] R. C. Willson, Appl. Opt., 18,179 (1979)

[7] J. Geist, Appl. Opt., 18,760 (1979)

[8] E. F. Zaleski and J. Geist. Appl. Opt., 19,1214 (1980).

[9] J. Geist, E. F. Zalewski and A. R. Schaffer, Appl. Opt., 19, 3795 (1980)

[10] G. Kirchoff, "Ueber das Verhaltniβ zwischen dem Emissionvermögen und dem Absorptionsvermögen der Körper für Warne und Licht'', Ann. Phys. 19, 275-301 (1860).

[11] W. Wien and O.Lummer." Methode zu Prüfung des Strahlungsgesetzes absolut schwarzer Körper'', Ann. Phys. 56, 451 – 456, (1895).

[12] H. Preston Thomas, "The international temperature scale of 1990 (ITS-90),'' Metrologia 27,3-10 (1990).

[13] V. I. Sapritsky, " Black body radiometry'', Metrologia 32, 411-417 (1995/96).

[14] D. C. Ginnings and M. L. Reilly " Temperature its measurements and Control in Science and Industry, 4 (Instrument society of America, Pittsburg, Penn., 1972) p, 339.

[15] W. R. Blevin and W. J. Brown, Metrologia, 7, 15 (1971)

[16] W. R. Blevin, Metrologia, 6, 39 (1970).

[17] T. J . Quinn and J. E. Martin, Philos.Trans. R. Soc.London, ser. A, 316, 85 (1985)

[18] J. E. Martin, T. J . Quinn and B. Chu, Metrologia, 25, 107 (1988).

[19] J. E. Martin, N. P. Fox and P. J. Key, Metrologia, 21, 147 (1985).

[20] T. J. Quinn and J. E. Martin, " Precision measurement and fundamental constants II, Nat. Bur. Stand. (US),'' Sec. Publ.617, Washington DC: U.S. Government printing office, 291-297 (1984).

[21] J.E. Martin, N. P. Fox and P. J. Key, "A cryogenic radiometer for absolute radiometric measurements,'' metrologia 21, 147- 155 (1985).

[22] T. J. Quinn and J. E. Martin, " A radiometric determination Of Stefan-Boltman constant and the thermodynamic temperature between –40 ^{0}C and + 100 ^{0} C,'' Phil. Trans.R. Soc.Lond., A316, 85-189, (1985).

[23] T.Varpula, H.Seppa and J. M.Sarri. "Optical power calibrator based stabilized green He-Ne laser and a cryogenic absolute radiometer,'' IEEE Trans. Instrum. Meas.38, 558-564 (1989).

[24] P.V. Foukal, C. Hoyt, H. Kochling and P. Miller, "Crayogenic absolute radiometers as laboratory irradiance standards, remote sensing detectors, and phyroheliometers ,'' Appl. Opt. 29, 988-993 (1983).

[25] E.F. Zalewski and C.R. Duda, " Silicon photodiode device with 100% external quantum efficiency,'' Appl. Opt. 22, 2867-2873 (1983).

[26] N.P. Fox, “Trap detectors and their properties,’’ Metrologia 28, 197-202 (1991).

[27] J. M. Palmer, “Alternative configurations for trap detectors,’’ Metrologia, 30, 327-333 (1993).

[28] R. Köhler, R. Goebel and R. Pello. “Results of an international comparision of spectral responsivity of silicon photodetectors,’’ Metrologia 32, 463-468 (1995/96).

[29] O. Touayar, H. Reyn, J.Bastie and T. Varpula, “Indirect comparison of cryogenic radiometers from INM (France) and the VTT (Finland) with a QED-200 from VSL (Netherlands),’’ Metrologia 32, 561-564 (1995/96).

[30] A. Lassila, H. Hofer, E.Ikonen, L.Liedquist, K.D. Stock and T. Varpula, “ Intercomparison of cryogenic radiometers using silicon trap detectors,’’ Meas. Sci. Technol. 8, 123-127 (1997).

[31] E. F. Zalewski and C. C. Hoyt, “Comparison between cryogenic radiometry and predicted quantum efficiency of pn silicon photodiode light traps,’’ Metrologia, 28, 203-206 (1991).

[32] T. Varpula, L. Liedquist, H. Ludvigsen, H. Reyn and J. de Vreede, “Comparison of quantum efficient silicon photodetectors with a cryogenic absolute radiometer at a laser wavelength of 543.5 nm,’’ Metrologia, 28, 349-352 (1991).

[33] D. H. Nettleton, T.R. Prior and T.H. Ward, “ Improved spectral responsivity scales at the NPL, 400 nm to 20 μm,’’ Metrologia 30, 425-452 (1993).

[34] T. R. Gentile, J. M. Houston and C.L Cromer. “ Realization of scale of absolute spectral response using National Institute of Standards and Technology high accuracy cryogenic radiometer,’’ Apl. Opt.35 4392-4403 (1996).

[35] J.Geist, “Qunatum efficiency of p-n junction in silicon as an absolute radiometric standard,’’ Appl.Opt. 18, 760-762 (1979).

[36] L. Werner, J.Fisher, U. Johannsen and J.Hartman, " Accurate determination of spectral responsivity of silicon trap detectors between 238 nm and 1015 nm using laser based cryogenic radiometer,'' Metrologia, 37, 279-284 (2000).

[37] J. Geist, A. M. Robinson and C.R.James, " Numerical modeling of silicon photodiodes for high accuracy applications. Part III: Interpolating and extrapolating internal quantum efficiency calibrations, J. Res. Natl. Inst. Stand. Techol., 96, 481-492 (1991).

[38] A. Cuevas, R. A. Sinton, M. Ker, D. Macdonald, Helmut Mackel, "A contactless photoconductance technique to evaluate the quantum efficiency of solar cell emitters, Solar Energy Materials and Solar Cells 71, 295- 312 (2002).

[39] L. Kreinin, N. Bordin, and N. Eisenberg, " Self calibration technique as a tool for high accuracy determination of silicon solar cell internal quantum efficiency, Solar Energy Materials and Solar Cells, 53, 299-311 (1998).

[40] L. Kreinin, N. Bordin, and N. Eisenberg, " Use of the self calibration method for accurate determination of silicon solar cell internal quantum efficiency, Solar Energy Materials and Solar Cells, 63, 247-257 (2000).

[41] X. M. Dai and Y. H. Tang, " A simple general analytical solution for the quantum efficiency of front surface field solar cells, Solar Energy Materials and Solar Cells, 43, 363-376 (1996).

[42] Fiber optic Test and Measurement,Edited by Dennis Derickson,55-65,1998.

[43] N. P. Fox, " Uses of cryogenic radiometer in absolute radiometry'', Natioanal Physical Laboratory, Teddington , UK.

[44] R. E. Bedford and C. K. Ma, J. Opt. Soc. Am., 66, 724 (1976)

[45] J. C. De.Vos. Physica, 20, 669 (1954)

[46] T. J. Quinn, Temperature (Academic Press, London, 1983), p.307.

[47] R. A. Smith, F. E. Jones and R. P. Chasmar, The detection of measurement of infrared radiation (Clarendon, London, 1957), p.47.

[48] T. R. Gentile, J. M. Houston and C.L Cromer, Appl. Opt. 35, 1056-1068 (1996).

[49] J.S. Blakemore: Rev.Sci.Instrum., 33, 106 (1962)

[50] R.L. Rusby: Temperature: Its measurements and control in science and industry, 5 (American Istitute of Physics, New York, N.Y., 1982), p. 829

[51] B. W. A. Ricketson, Platinum Met. Rev., 33, 55 (1989)

[52] J.E. Martin, Cryogenic Radiometry, p.375,(1992)

[53] A. Ghanadzadeh and M.S Beevers, Journal of Molecular Liquids 107/1–3,77–98 (2003)

[54] M. Duarte and M.M.F. Vieira, Optics and Lasers in Engineering 28, 481-484, (1997)

[55] J. Torgerson, W.Nagourney, Optics Communications, 161, 264-266 (1999)

[56] A.Waksberg, Optics and Laser Technology, October 1975

[57] R.Köhler,R.Goebel and R.Pello, *Metrologia*, 33, 549-554, (1996).

[58] O.D.D. Soores, Trends in optical fibre, Metrology and standards, NATO ASI Series, p.78, (1995).

[59] R.Köhler,R.Goebel, R.Pello, O. Touayar and J. Bastile, First results of measurements with the BIPM cryogenic radiometer and comparison with the INM cryogenic radiometer, *Metrologia*, 32, 551-555 (1995/96)

[60] T.R.Gentile, J.M.Houston, J.E.Hardis, C.L.Cromer, and A.C.Parr, National istitute of standards and technology high-accuracy cryogenic radiometer, Appl.Opt. 35, 1056-1068 (1996)

[61] K. D. Stock and H. Hofer, Present state of the PTB primary standard for radiant power based on cryogenic radiometry, Metrologia, 30, 291-196 (1993)

[62] Guide to expression of uncertainty in measurements 1993.

[63] E. L. Dereniak, D. G. Crowe, Optical Radiation Detectors, New Yorl, 43-58 (1984)

[64] NIST special publication , Spectroradiometric detector measurements, 250-41, (1998)

[65] Petri Karha,Pasi Toivanen, Farshid Monoochehri, Erki Ikonen, Development of a detector based absolute spectral irradiance scale in the 380-900 nm spectral range, Applied Optics, 36, 8809-8918 (1997)

[66] T.Kübarsepp, A.Haapalinna, P.Karha, E.Ikonen, Non linearity measurements of photodiodes, Appl.Opt. 37, 2716-2722, (1998)

[67] J.Fischer and L.Fu, Photodiodes nonlinearity measurement with an intensity stabilized laser as a radiation source, Appl.Opt.32, 4187-4190, (1993)

[68] Atte.Haapalinna, T.Kübarsepp, P.Karha, E.Ikonen, Measurement of the absolute linearity of photodetectors with a diode laser, Meas. Sci. Technol. 10, 1075-1078, (1999)

[69] N.P. Fox, J.E. Martin, Inst. Phys. Conf. Ser., 92, 31-37 (1989)

[70] R. Köhler, R. Goebel, R. Pello, J. Bonhoure, Metrologia, 28 211-215 (1991)

[71] E.F.Zalewski, C.C.Hoyt., Comparison between cryogenic radiometry and predicted quantum efficiency of pn silicon photodiode light traps, Metrologia. 28, 203-206, (1191)

[72] Petri Karha,Anti Lassila, Hanne Ludvigsen, Farshid Monoochehri,Heidi Fagerlund, Erki Ikonen,Optical Engineering, 34, 2611-2618. (1995)

[73] J. D. Jackson, Classical Electrodynamics, John Willey and Sons.Inc, pp.278-282, (1975)

[74] Atte Haapalinna, Petri Karha, and Erkki Ikonen, Applied Optics, 37, 729-732,(1998).

[75] J.Geist, D. Chandler-Horowitz, R. Köhler, A.M. Robinson, and C.R James, Metrologia 28, 193-196 (1991)

[76] J. Geist, E. F. Zalewski, and A.R. Schaefer. Applied optics, 19, 3795-3799 (1980)

[77] C. Hicks, M. Kalatsky, R. A. Metzler, A. O. Goushcha, Applied Optics, 42, Issue22,4415-4422 (2003)

[78] H.J. Möller, Semiconductors for Solar Cells, John Willey and Sons.Inc ,New York,19-39, (1993)

[79] L.Kreinin, N. Bordin, N. Eisenberg, Solar Energy Materials and Solar Cells 53 299-311 (1998)

[80] N. Bordin, L.Kreinin, N. Eisenberg, Solar Energy Materials and Solar Cells 63 247-257 (2000)

[81] Ben G. Streetman,Solid State Electronic Devices,Fourth Ed., pp.87,117,439,1995

[82] RS-5900 electrically calibrated pyroelectric radiometer ınstruction manual 12802 Rev B January 1991

[83] W.M.Doyle, B.C.McIntosh and J. Geist,Implementation of a System of Optical Calibration Based on Pyroelectric Radiometry, Opt.Eng. 15, 541-548 (1983)

[84] E. L. Dereniak and F.G. Brown, Infrared Physics, 15 (1975) 36-43

[85] J.Lehman, G. Eppeldauer, J.A. Aust, and M.Racz, Domain-engineered Pyroelectric Radiometer, Appl.Opt. 38, 7047-7055 (1999)

[86] T.R.Gentile, J. M.Houston, G. Eppeldauer, A.L. Migdall, and C.L.Cromer, Calibration of a Pyroelectric Detector at 10.6μm with the National Institute of Standard Technology High Accuracy Cryogenic Radiometer,Appl.Opt. 36, 3614-3621 (1997)

[87] Thomas C. Larason, Sally S. Bruce, and Albert C. Parr, NIST Special Publication 250-41, 29-31 (1998)

[88] An introduction to bentham ınstruments limited 2 Boulton Road Reading Berkshire RG2 ONH

[89] Farshid Manoochehri, High Accuracy Spectrometer for Application in Photometry and Radiometry, Helsinki University of Technology Department of Electrical and Communications Engineering Metrology Reserch Institute,, pp 3-4 (1998)

[90] W.R. Meclurey, Introduction to Radiometry and Photometry, Boston, London p.77 (1994)

[91] K D Stock, R Heine and H Hofer Spectral characterization of Ge trap detectors and photodiodes used as transfer standards Metrologia 40 S163–S166 (2003)

[92] Metzdorf J Metrologia 37 573–8 (2000)

[93] Stock K D, Hofer H, Pawlak M and Metzdorf J Metrologia 35 279–82 (1998)

[94] P.W.Kruse, Infrared Phys. Technol, 36 (1995) 869-882

[95] Ping-Shine Shaw, Thomas C. Larason, Rajeev Gupta, Steven W. Brown, and Keith R.Lykke, Improved Near Infrared Spectral Responsivity Scale, J. Res. Natl. Stand. Technol. 105 697-700 (2000)

[96] Stock K D Appl. Opt. 27 12–14 (1988)

VITA

ÖZCAN BAZKIR was born in Bingöl on January 05, 1973. He graduated from Physics department of METU in 1997. He received the M.Sc. degree in 1999 and Ph.D degree in 2004 from the same department. He worked in Middle East Technical University as a research assistant from 1997 to 2001. He has been working in Optics Laboratory at National Metrology Institution of Turkey (UME) since 2001. His main areas of interest are solid state, semiconductors, silicon based materials, lasers, radiometry and photometry.

List of Publications:

1. "High-accuracy optical power measurements by using electrical-substitution cryogenic radiometer" **Özcan Bazkır**, Sevilay Uğur, Farhad Samadov, Akif Esendemir, *Optical Engineering* (at press).
2. "Characterization of Silicon Photodiode Based Trap Detectors and Establishment of Spectral Responsivity Scale" **Özcan Bazkır,** Farhad Samadov, *Optics and Lasers in Engineering.*
3. "Realization of relative responsivity scale with the elctrically calibrated pyroelectric radiometer", **Özcan Bazkır**, Oğuz Çelikel, Farhad Samedov, *Submitted to Optics & Laser Technology.*
4. "Electrical substitution cryogenic radiometer based spectral responsivity scale between 250-2500 nm wavelengths**", Özcan Bazkır,** Farhad Samadov, *Submitted to Optica Applicata.*
5. "Realization of Photometric Base Unit of Candela Traceable to Cryogenic Radiometer at UME", F. Samedov, M. Durak, **Ö. Bazkır,** *Submitted to The European Physical Journal Applied Physics.*